Non-Gaussian Fluctuations in Active Suspensions

Irwin Morton Zaid

Lady Margaret Hall

University of Oxford

A thesis submitted for the degree of

Doctor of Philosophy

Michaelmas 2012

Abstract

An active particle converts energy to motion. An active suspension is a population of active particles, typically microscale, that are immersed in a viscous and/or elastic medium.

This thesis is about the statistics of active suspensions. Unlike a suspension at thermodynamic equilibrium, we show that an active suspension inherently has non-Gaussian fluctuations due to an interplay between self-driven constituents and microscopic physics. Consequently, the diffusion of a tracer in an active suspension is not Gaussian.

Our results explain some experiments with active suspensions that contain either swimming microorganisms or molecular motors. We provide different models for the fluctuations in dilute active suspensions, ranging from phenomenological to exact. The fundamental ingredient of such non-Gaussian fluctuations is an ultraslow convergence to the central limit theorem caused by truncated power-laws. Without any truncation, there is an intimate relation to the generalized central limit theorem.

We suggest similar effects occur in many other systems. These may be associated with probability distributions that appear to be exponential.

To Marie Morton, I hope you would be proud of this.

Acknowledgements

I couldn't have done this by myself and there are many people who deserve my thanks.

This thesis just would not exist without Julia Yeomans. Thanks for taking me as a student and listening to a plethora of wild ideas from the day we met. You had endless patience with me. I enjoyed all that we did together.

Because of Richard Berry, I didn't spend four years only thinking about non-Gaussian fluctuations. Thanks for bringing me into your laboratory without a second of hesitation. You gave me the freedom to build and explore, as well as support when I needed it. I learned a lot by watching what you do.

For better or worse, my conception of what research should be was shaped by Ralf Metzler. Thanks for introducing me to so many things, ranging from statistics to Schwäbisch, especially when it wasn't clear it might pay off. You always had my best interests in mind. It is your fault that I cannot escape the binding spell of the generalized central limit theorem.

When I started to write this thesis, I had to decide whether it was going to be about non-Gaussian fluctuations or digital holography. I owe James Flewellen for what didn't make it in. Thanks for throwing yourself in with me, holding it all together in the dark days of 2012, and keeping everything fun. I can't wait to see what comes next.

All of my friends each deserve their own paragraph, I'm sorry that I can't give it to them. In the context of this thesis, I do want to mention Jack Cohen, Lisa Mövius, Tom Ouldridge, Mitya Pushkin, Vic Putz, Petr Šulc, and Ioannis Zachardiou. Thanks for being around.

There is so much I have gained from all of my collaborators, but I must single out Daisuke Mizuno here. His experiments forced me to revisit the

fluctuations of active suspensions. Thanks for being generous with your ideas, data, and time.

While being a graduate student, I've been lucky enough to interact with many famous scientists. Among those, there is someone that really stands out. Michael Nielsen, pioneer of quantum computing and advocate of open science, not only came at my invitation to speak, but also hung around to chat with me personally for quite a long time afterwards. Thanks for demonstrating to me, and the world, what science should be.

Way back before Oxford, I was a lost undergraduate student at Carleton University. Jason Morrison and Bruce Campbell took the time to guide, inspire, and teach me. Thanks to both of you for starting me on this path.

If I'm able to accomplish anything now, it is because of what I attempted before. Dave Amundsen gave me a chance to mess around with solitary waves. Bill Macready and the rest of D-Wave Systems showed me what ambition means. Jit Bose and Pat Morin let me explore geometric graphs. Thanks for those opportunities.

Finally, we've reached the most important person to this thesis and to me. Thank you, Lauren Hutchinson, for always being there. You have been wonderful through everything, while asking for so little in return. We've passed through a snowy capital, a "toytown", and, finally, some dreaming spires. I always cherish that you came with me on this adventure.

Publications

Chapter 3 has been published, see below. Chapters 4 and 5 are each being prepared as a publication.

- A. V. Chechkin, I. M. Zaid, M. A. Lomholt, I. M. Sokolov, and R. Metzler, *Bulk-mediated diffusion on a planar surface: full solution*, Phys. Rev. E **86** (2012), 041101.
- I. M. Zaid, J. Dunkel, and J. M. Yeomans, *Lévy fluctuations and mixing in dilute suspensions of algae and bacteria*, J. Roy. Soc. Interface **8** (2011), 1314-1331.
- A. V. Chechkin, I. M. Zaid, M. A. Lomholt, I. M. Sokolov, and R. Metzler, *Effective surface motion on a reactive cylinder of particles that perform intermittent bulk diffusion*, J. Chem. Phys. **134** (2011), 204116.
- J. Dunkel, V. B. Putz, I. M. Zaid, and J. M. Yeomans, *Swimmer-tracer scattering at low Reynolds number*, Soft Matter **6** (2010), 4268-4276.
- J. Dunkel and I. M. Zaid, *Noisy swimming at low Reynolds numbers*, Phys. Rev. E **80** (2009), 021903.
- I. M. Zaid, M. A. Lomholt, and R. Metzler, *How subdiffusion changes the kinetics of binding to a surface*, Biophys. J. **97** (2009), 710-721.
- A. V. Chechkin, I. M. Zaid, M. A. Lomholt, I. M. Sokolov, and R. Metzler, *Bulk-mediated surface diffusion along a cylinder: propagators and crossovers*, Phys. Rev. E **79** (2009), 040105.
- M. A. Lomholt, I. M. Zaid, and R. Metzler, *Subdiffusion and weak ergodicity breaking in the presence of a reactive boundary*, Phys. Rev. Lett. **98** (2007), 200603.

Contents

List of Figures

Chapter 1

Introduction

1.1 Life is complicated

Fluctuations are the beating heart of the microscopic world. The jiggling of a colloid suspended in a viscous fluid, the intrinsic variability of gene expression, and the run-and-tumble pattern of a swimming *E. coli* all have randomness as a fundamental ingredient. Not only are these relevant for biology, but they also have led to many new ideas in statistical physics throughout the last century.

Still, phenomena at the microscale are more than stochastic, as chaotic and/or nonlinear effects appear quite often. In the face of so much complexity, is it reasonable to search for simple models? Or is there no other choice than to simulate an entire system in terms of its interacting constituents? Assuming, of course, that simulation is even within our limits of computation. For some problems, coarse-grained theories have been very successful, by subsuming unnecessary degrees of freedom into effective variables that are really of interest. The challenge to a physicist is to determine which details are worth considering.

This sort of approach has recently been used to model life, from the cytoskeleton of a cell to a flock of birds or a herd of beasts, which we generally refer to as active matter [1, 2, 3, 4]. What defines active matter is that each system consists of self-driven particles capable of converting energy to motion. The interaction of these particles with each other, and the medium they live in, leads to collective behavior

and emergent mechanics. Despite the obvious differences between systems, it is hoped that a mathematical framework can predict their shared characteristics.

Many descriptions of active matter take quantities like concentration, orientation, and flow as continuum fields. Formally, these are valid for both dilute and dense systems, though most studies lie somewhere in between.[1] In order to model biology realistically, fluctuations inherent to active matter must be included. This thesis is mostly about the first steps toward understanding these fluctuations, specifically at the microscale.

We used the word 'fluctuations' a little too glibly – think about randomness embedded in some active matter, not statistics produced in a thermal bath. In fact, at thermodynamic equilibrium, Gaussian fluctuations always occur [5]. Suppose u is a variable in some closed system. Given $S(u)$ as the entropy, the probability distribution for u is $P(u) \propto e^{S(u)}$ in the microcanonical ensemble. We expand $S(u)$ about its maximum at $\langle u \rangle$,

$$S(u) \simeq S(\langle u \rangle) + \frac{\partial}{\partial u} S(u)\bigg|_{u=\langle u \rangle} (u - \langle u \rangle) + \frac{\partial^2}{\partial u^2} S(u)\bigg|_{u=\langle u \rangle} \frac{(u - \langle u \rangle)^2}{2}, \tag{1.1}$$

which is specifically valid near thermodynamic equilibrium as u approaches $\langle u \rangle$. Renormalizing, then matching the constants of Eq. (1.1) against the moments of u, leads to

$$P(u) = \frac{e^{(u-\langle u \rangle)^2/(2\langle u^2 \rangle)}}{(2\pi \langle u^2 \rangle)^{1/2}}. \tag{1.2}$$

By its very definition, a suspension of active particles is not at thermodynamic equilibrium. What should be expected?

1.2 Kinds of activity

Our focus is on active suspensions in the dilute limit, particularly those with swimming microorganisms or molecular motors. This section provides some background

[1] A continuum description can include a probability distribution for its constituents, making it valid even for very dilute systems.

for what is to come.

1.2.1 Animalcules

Most microorganisms navigate their environment. Many species of bacteria, for instance, propel themselves with tiny motors that each rotate a helical flagellum [6]. To reach their optimum conditions for growth, they alter their swimming patterns in response to environmental cues. Some species tumble periodically as they swim, others reverse, some stop, and others screw through the medium using their spiral-shaped bodies.

Life in the microscopic world was first observed around the turn of the 17th century. Using a primitive microscope made from a small glass bead, Antonie van Leeuwenhoek claimed there were more animalcules, meaning "little animals", in a single drop of water than people in the entire Dutch kingdom [7].

While microorganisms always fascinated biologists, it was the pioneering work of Geoffrey Taylor in 1951 that brought them into physics and mathematics [15]. He simply asked how a tiny object could propel itself without imparting momentum to the fluid, as fish do. By considering a waving sheet, he showed that force-free swimming is possible even if the fluid is viscous. Although a waving sheet is not quite a flagellum, models in this spirit have proved helpful for understanding the fluid mechanics of swimming microorganisms. Of course, there also exist models closer to biology, where a flagellum is approximated as a slender curve of point forces [16, 17].

For such tiny scales, the laws of physics are fundamentally different from those we experience in our macroscopic world. Edward Purcell pointed this out in his famous 1976 lecture "Life at low Reynolds number" and, more specifically, used a scallop to highlight the importance of kinematic reversibility to microorganisms [11]. Without inertia, the flow of a fluid is determined instantaneously. If a swimming stroke is the same under time reversal, then the net force applied to the fluid vanishes as any

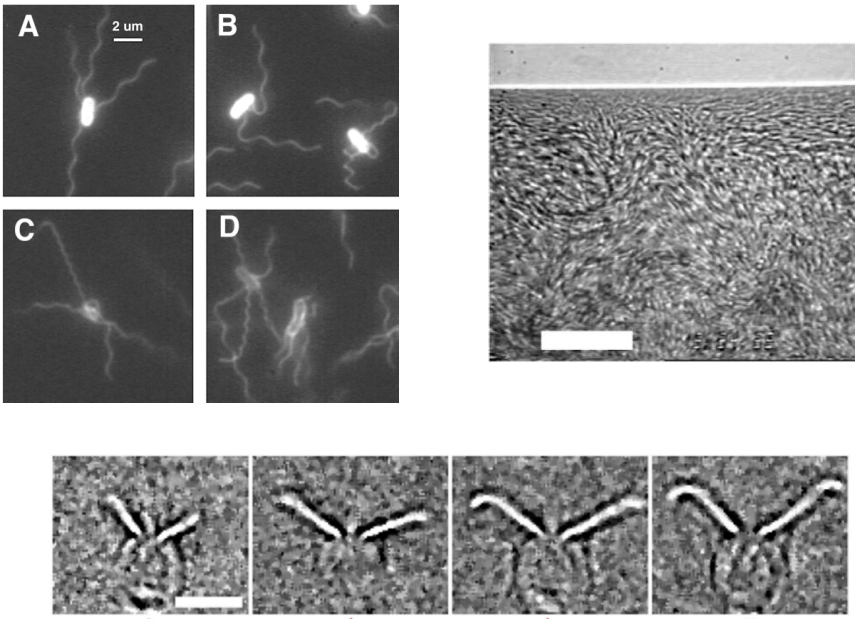

Fig. 1.1: Examples of biological swimmers. (Top left) *E. coli* swims by rotating many helical flagella, from Ref. [8]. (Top right) Collective behavior of *B. subtilis* in a sessile drop, from Ref. [9]. (Bottom) *C. reinhardtii* swims by beating a pair of apical flagella, from Ref. [10].

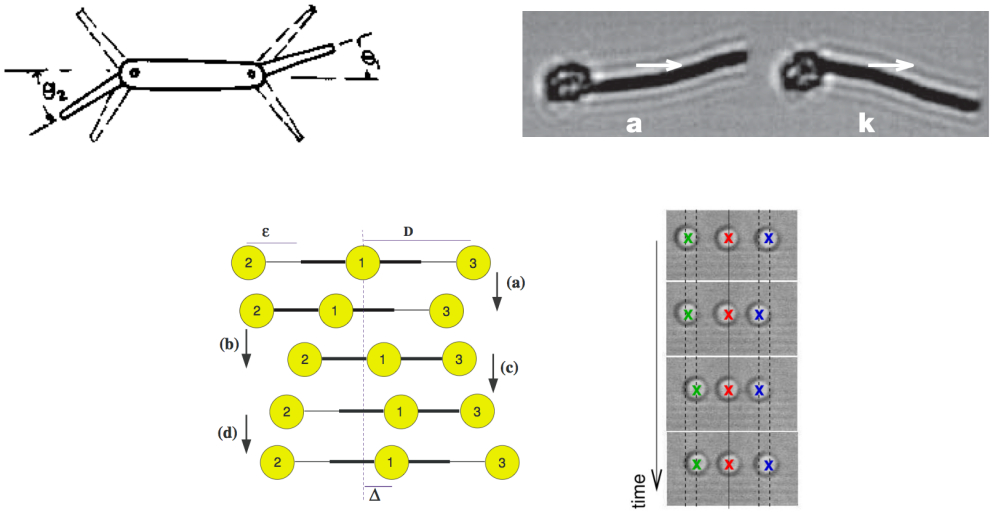

Fig. 1.2: Examples of artificial swimmers. (Top left) The Purcell swimmer made of three rods, from Ref. [11]. (Top right) A chain of magnetic colloids linked by DNA carrying a red blood cell, from Ref. [12]. (Bottom left) The Najafi-Golestanian swimmer made of three spheres, from Ref. [13]. (Bottom right) A set of colloids moved with optical tweezers pumping fluid, from Ref. [14].

propulsion is canceled by its reversed counterpart. So a scallop does not swim in a viscous fluid because its shell can only open and close. In order to swim, two or more degrees of freedom are needed, like an example from Purcell's lecture that consists of three slender rods articulated by two hinges. An analysis of the Purcell swimmer is possible, but rather involved [18]. Something much easier to work with is the Najafi-Golestanian swimmer, just three spheres linked by two rods [13]. Both swimmers have been realized experimentally [19, 14], among various others. These include colloids linked by DNA [12], a robot with an elastic oar [20], symmetry-breaking microstructures operating at a water-air interface [21], chiral propellers [22], and flexible wires [23]. We display some biological and artificial swimmers, respectively, in Figs. 1.1 and 1.2.

Anything that swims must create a flow in the surrounding fluid. This flow affects how a swimmer interacts with a surface [24, 25] or another swimmer [26, 27]. As a swimmer nears a solid boundary, it may be drawn into circular trajectories [24], depending on its shape and size [25]. When two swimmers approach each other, they can attract or repel [26], as well as form bound states [27]. On a single microorganism, or between a pair of them in close proximity, it is thought flagella may synchronize beats solely via the fluid [15, 28, 29]. Cilia, anchored filaments that switch between conformations, often appear as arrays able to generate large-scale flow by organizing, perhaps hydrodynamically, into dynamic patterns like metachronal waves [30].

Just as flagella and cilia act coordinately, suspensions of swimming microorganisms also exhibit collective behavior [9, 31, 32]. At a high concentration of swimmers, say a million cells per millilitre, complex structures rapidly appear and disappear. These structures, which far exceed the size of an individual, can be plumes [33], networks [34], swarms [35], or vortices [36]. Most theoretical approaches for collectivity either reduce a microscopic model to coarse-grained equations [37, 38] or introduce phenomenological equations from symmetry arguments [39, 40]. Since microorgan-

isms naturally occur in dense communities, ranging from biofilms to blooms, the collective behavior of swimmers has wider implications for biology and physiology.

1.2.2 Minimotors

In a cell, self-assembly and self-organization occur through the dissipation of adenosine triphosphate (ATP) or guanosine triphosphate (GTP). Molecular motors convert this chemical energy to mechanical work, exerting forces on a network of polar elastic filaments, namely the cytoskeleton. Almost always out of equilibrium, the cytoskeleton dynamically changes in response to various stimuli, such as mechanical forces or chemical gradients. It is critical for most properties and processes of a cell [41].

By itself, a molecular motor is an assembly of parts that move coordinately through a series of conformational changes. It can be understood in terms of mechanical concepts like force, elasticity, damping, and work [42]. For the cytoskeleton, we are thinking of linear motors, say dynein, kinesin, or myosin, that bind to, then sometimes move along, its filaments. This differs from ion pumps and rotary motors, which are permanently anchored to a membrane. A linear motor generates a force of about 5 pN [43].

It is simply too complex to study *in vivo* how molecular motors interact with the cytoskeleton. As an alternative, a network of filaments, say tubulin or actin, can be reconstituted *in vitro*, which allows specific effects to be isolated and explored. The motivation is to understand the mechanics of a cell from the bottom up [44, 45]. A schematic of a molecular motor (myosin II), as well as how it affects a network (actin), is shown in Fig. 1.3.

Without activity from molecular motors, a network of filaments behaves like a polymer gel [48]. The gel can have either temporary or more permanent crosslinks, depending on how the time for association between the crosslinking proteins and filaments compares against the time over which measurements are made. At short

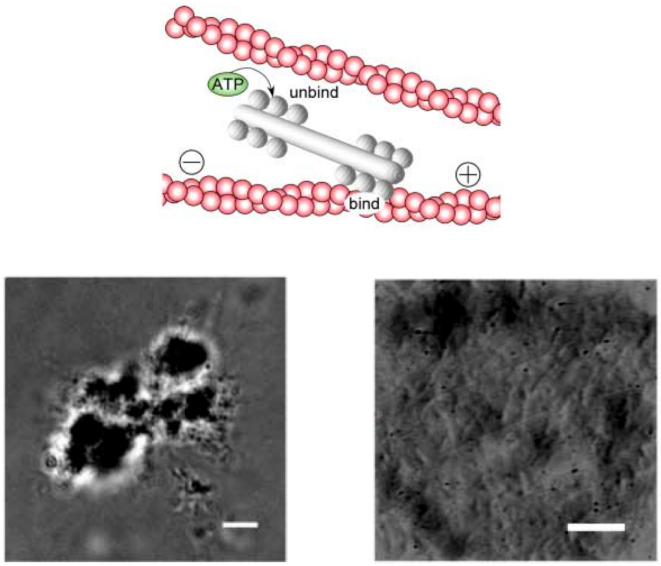

Fig. 1.3: A myosin minifilament binds to a pair of actin filaments (top), which yields actin-myosin complexes (bottom left) that are not present in an actin network without myosins (bottom right). All figures are from Ref. [46].

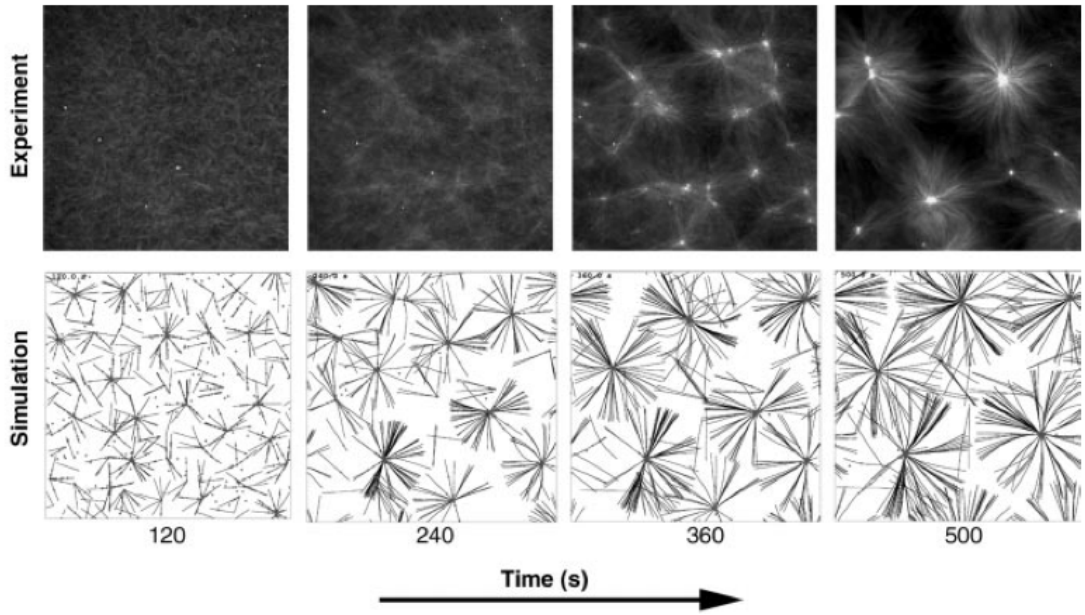

Fig. 1.4: Asters formed by kinesins and microtubules, as observed *in vitro* (top) or as reproduced *in silico* (bottom). All figures are from Ref. [47].

times, the mechanical response to a perturbation is characterized by a shear modulus. Eventually, there is also flow, corresponding to a viscosity. These macroscopic parameters can be related to the microscopic structure of a network by simple models that describe flexible or stiff polymers.

When the molecular motors are active, the network is driven out of equilibrium and theories for polymers in static conformations do not apply. Instead, what is needed is a dynamic model that reflects the local fluxes of the system. Just as for swimmers, this comes from coarse-grained equations [49, 50] or phenomenological equations [51, 52].

At present, it is established that molecular motors and a network of filaments are a simple *in vitro* route to pattern formation. For example, transient structures, namely asters and vortices, have been observed in a suspension containing only kinesins and microtubules [53, 47]. By varying the concentration of a component, the suspension formed a rich set of patterns. We display some of the patterns in Fig. 1.4. Many of the patterns could be reproduced *in silico* using self-propelled particles, to represent kinesins, and semi-flexible rods, to represent microtubules, that interact locally. Building on these studies, other experiments see a plethora of phenomena, including polar clusters [54], density inhomogeneities [55], and steady states [56]. If such variety comes out of basic ingredients, then a cell may easily have lots of diverse structures.

1.3 So, what's the plan?

There are different ways to think about what we are going to do. One is that, even though active matter has been studied at scales ranging from individual particles to continuum fields, there is very little understanding of its intrinsic fluctuations. We uncover simple experiments on suspensions containing active particles, where the measured probability distributions have shapes that are not understood. According to

the second page of this thesis, these probability distributions are definitely not Gaussian distributions. By extending statistical methods developed for non-equilibrium systems, we find some probability distributions that help to explain the experiments.

Or perhaps this thesis is not really about active suspensions at all! It seems as if non-Gaussian fluctuations are found throughout nature. Wherever that happens, the classical tools used so often in statistical physics – like the central limit theorem, the Langevin equation, and the Fokker-Planck equation – fail quickly. We must develop new approaches to non-Gaussianity, beyond cumulant expansions and uncorrelated continuous random walks. What we are going to do may be a few of the many steps to get us there.

From any perspective, we need a proper basis to get started. It is for this reason that Chapter 2 exists. We review the fundamental equations of fluid and solid mechanics, especially certain limits relevant to most active suspensions. Using the appropriate Green's function, we discuss simple models for an active particle. More generally, we illustrate some unique characteristics of all active particles. After going through the necessary physics, we move towards probability and stochastic processes. We explain the Gaussian distribution from the central limit theorem and the Lévy stable distribution from the generalized central limit theorem, followed by Langevin and Fokker-Planck equations that are particularly helpful.

In Chapter 3, we study a suspension that consists of swimmers and tracers. At a dilute concentration, swimming microorganisms behave mostly independent from each other. This allows us to model a suspension of them as an "ideal gas" of ballistic particles. We combine analytic techniques and numerical simulations to show that the trajectory of a tracer diffusing amongst a population of swimmers is a Lévy-like flight. The reason for such non-Gaussian statistics is an ultraslow convergence, with respect to the central limit theorem, from the power-law decay in the velocity field of a swimmer.

After Chapter 3 whet your appetite for non-Gaussianity, Chapter 4 provides even more. We temporarily forget all about active suspensions to focus on the statistical physics of power-law fields. Assuming statistical isotropy, we derive an exact probability distribution, as well as a much simpler approximation to it, for the sum of many power-law fields distributed uniformly in space. This allows us to prove the existence of near-exponential tails, which are universal in the sense there is no dependence, except for constants, on the specific power-law.

Chapter 5 makes good on a promise made by the title of this thesis, which is non-Gaussian fluctuations occur in suspensions of active particles, not just those with swimmers. We use the mathematical machinery of Chapter 4 to predict a steady state for tracers placed in a reconstituted network of elastic filaments alongside molecular motors. Unlike a steady state at thermodynamic equilibrium, this probability distribution is non-Gaussian even though it is a steady state. This makes it possible to measure kinetic parameters of molecular motors from displacements of tracers.

We finally conclude in Chapter 6 with a summary of this thesis and some ideas for the future.

Chapter 2

Prerequisites in Physics and Probability

2.1 Continuum equations

At the microscale, life appears in environments that are quite different from those we experience. If we want to model active particles, or to prove things about them, then we need to know which equations in physics are relevant.

We are going to work with media that flow and/or deform. These are described by continuum equations, namely the Navier-Stokes and Navier-Cauchy equations. Generally, both are nonlinear partial differential equations that must usually be solved numerically. Under specific conditions, we reduce each to a linear partial differential equation that can more often be studied analytically. The linear counterparts are, respectively, the Stokes and Navier equations.

From whichever equation is appropriate to the environment, we derive simple expressions that help us to model an active particle. These form a basis for understanding the field induced by an active particle.

2.1.1 Viscous flows

The Navier-Stokes equations govern the motion of a fluid,

$$\rho\left(\frac{\partial}{\partial t}\mathbf{u}(\mathbf{r},t)+\mathbf{u}(\mathbf{r},t)\cdot\nabla\mathbf{u}(\mathbf{r},t)\right)=\nabla\cdot\boldsymbol{\sigma}(\mathbf{r},t)+\mathbf{f}(\mathbf{r},t), \tag{2.1}$$

where $\mathbf{u}(\mathbf{r},t)$ is the velocity, ρ is the density, $\boldsymbol{\sigma}(\mathbf{r},t)$ is the stress tensor, and $\mathbf{f}(\mathbf{r},t)$ is the applied force per unit volume. We consider only incompressible fluids, for which ρ is constant and $\nabla\cdot\mathbf{u}(\mathbf{r},t)=0$. Eq. (2.1) follows straightforwardly from Newton's second law applied to a volume of fluid. Each term in the bracket on the left-hand side represents an acceleration, either unsteady as the time derivative of $\mathbf{u}(\mathbf{r},t)$ or convective as the dot product of $\mathbf{u}(\mathbf{r},t)$ and its gradient. On the right-hand side are both the internal and external forces. To actually model a fluid, we must express $\boldsymbol{\sigma}(\mathbf{r},t)$ in terms of measurable quantities. We often assume a Newtonian fluid with pressure $p(\mathbf{r},t)$ and viscosity η, meaning

$$\boldsymbol{\sigma}(\mathbf{r},t)=-p(\mathbf{r},t)\mathbf{I}+\eta[\nabla\mathbf{u}(\mathbf{r},t)+(\nabla\mathbf{u}(\mathbf{r},t))^{\dagger}]. \tag{2.2}$$

So Eq. (2.1) becomes

$$\rho\left(\frac{\partial}{\partial t}\mathbf{u}(\mathbf{r},t)+\mathbf{u}(\mathbf{r},t)\cdot\nabla\mathbf{u}(\mathbf{r},t)\right)=-\nabla p(\mathbf{r},t)+\eta\nabla^2\mathbf{u}(\mathbf{r},t)+\mathbf{f}(\mathbf{r},t). \tag{2.3}$$

A solution of Eq. (2.3), together with $\nabla\cdot\mathbf{u}(\mathbf{r},t)=0$, requires both $\mathbf{u}(\mathbf{r},t)$ and $p(\mathbf{r},t)$.

Without much effort, we are able to characterize the flow obtained from the Navier-Stokes equations in terms of a dimensionless quantity. Since each term in Eq. (2.3) has dimensions of force over volume, we multiply both sides by $l/(\rho v^2)$ and rewrite all variables using their dimensionless counterparts (denoted with $'$). The length l and velocity v are typical values imposed through the boundary conditions. We find

$$\frac{\partial}{\partial t'}\mathbf{u}'(\mathbf{r}',t')+\mathbf{u}'(\mathbf{r}',t')\cdot\nabla'\mathbf{u}'(\mathbf{r}',t')=-\nabla' p'(\mathbf{r}',t')+\mathrm{Re}^{-1}\nabla'^2\mathbf{u}'(\mathbf{r}',t')+\mathbf{f}'(\mathbf{r}',t'), \tag{2.4}$$

where $\mathrm{Re}=\rho l v/\eta$ is called the Reynolds number. This dimensionless quantity can be interpreted as the ratio of inertial to viscous forces.

If Re is small, then friction dominates. A swimming bacterium, say *E. coli*, is 1 μm in length and achieves velocities of 10 μm s^{-1} in water, leading to $\mathrm{Re}\sim 10^{-5}$. By contrast, a 30 m blue whale cruises through the ocean at 50 km h^{-1}, resulting

in Re $\sim 10^8$. For low Reynolds numbers, we take the limit Re $\to 0$, which reduces Eq. (2.3) to the Stokes equations,

$$-\nabla p(\mathbf{r}) + \eta \nabla^2 \mathbf{u}(\mathbf{r}) + \mathbf{f}(\mathbf{r}) = 0. \tag{2.5}$$

Technically, we also assume that any frequency is small, causing the 'angular' Reynolds number to be negligible. Subject to appropriate boundary conditions, Eq. (2.5) captures many microscale flows very well.

2.1.2 Elastic structures

Under a load, a body may become deformed and stressed. Generally, an elastic solid behaves according to the Navier-Cauchy equations,

$$\rho \frac{\partial^2}{\partial t^2} \mathbf{u}(\mathbf{r}, t) = \nabla \cdot \boldsymbol{\sigma}(\mathbf{r}, t) + \mathbf{f}(\mathbf{r}, t), \tag{2.6}$$

where $\mathbf{u}(\mathbf{r}, t)$ is the displacement, ρ is the density, $\boldsymbol{\sigma}(\mathbf{r}, t)$ is the stress tensor, and $\mathbf{f}(\mathbf{r}, t)$ is the applied force per unit volume. Just as for the Navier-Stokes equations, Eq. (2.6) is a restatement of Newton's second law. Given an isotropic solid that has only small displacements, $\boldsymbol{\sigma}(\mathbf{r}, t)$ is usually

$$\boldsymbol{\sigma}(\mathbf{r}, t) = \lambda(\nabla \cdot \mathbf{u}(\mathbf{r}, t))\mathbf{I} + \mu[\nabla \mathbf{u}(\mathbf{r}, t) + (\nabla \mathbf{u}(\mathbf{r}, t))^\dagger]. \tag{2.7}$$

The Lamé parameters μ and λ describe the solid, though sometimes the Poisson ratio $\nu = \lambda/[2(\mu + \lambda)]$ replaces λ. It is possible that λ is negative. Note $-1 \leq \nu \leq 1/2$ and $\nu = 1/2$ means incompressibility.

With $\boldsymbol{\sigma}(\mathbf{r}, t)$ from Eq. (2.7), Eq. (2.6) simplifies to

$$\rho \frac{\partial^2}{\partial t^2} \mathbf{u}(\mathbf{r}, t) = \mu \nabla^2 \mathbf{u}(\mathbf{r}, t) + (\mu + \lambda) \nabla(\nabla \cdot \mathbf{u}(\mathbf{r}, t)) + \mathbf{f}(\mathbf{r}, t). \tag{2.8}$$

A derivation like that of Eq. (2.5) yields the Navier equations,

$$\mu \nabla^2 \mathbf{u}(\mathbf{r}) + (\mu + \lambda) \nabla(\nabla \cdot \mathbf{u}(\mathbf{r})) + \mathbf{f}(\mathbf{r}) = 0. \tag{2.9}$$

There are two quantities analogous to the Reynolds number hidden in Eq. (2.8), $\rho v^2/\mu$ and $\rho v^2/(\mu+\lambda)$. When a typical value of the velocity v is small compared to $(\mu/\rho)^{1/2}$ and $(|\mu+\lambda|/\rho)^{1/2}$, Eq. (2.9) approximates Eq. (2.8) rather well.

2.2 From monopoles to multipoles

Many active particles are hard to model. For example, *E. coli* has a rod-shaped body with about 5 helical flagella. Besides the difficulty, solving Eq. (2.5) with such boundary conditions is not always necessary.

Our philosophy is to use simple models for active particles built out of point forces.[1] While these do capture some of the mathematical properties, at least asymptotically, they do not fully correspond to biological features. Still, throughout this thesis, a field $\mathbf{u}(\mathbf{r})$ caused by an active particle is approximated as the leading-order term in its multipole expansion.[2]

2.2.1 Point force

We seek the solution of Eq. (2.9) for a point force. Using this, we find the analogous solution of Eq. (2.5) subject to $\nabla \cdot \mathbf{u}(\mathbf{r}) = 0$.

Take $\mathbf{f}(\mathbf{r}) = \mathbf{F}\delta(\mathbf{r})$. We have, from Eq. (2.9),

$$\mu\nabla^2\mathbf{u}(\mathbf{r}) + (\mu+\lambda)\nabla(\nabla\cdot\mathbf{u}(\mathbf{r})) + \mathbf{F}\delta(\mathbf{r}) = 0. \tag{2.10}$$

Due to linearity, we expect a solution of the form $\mathbf{u}(\mathbf{r}) = \mathsf{G}(\mathbf{r})\cdot\mathbf{F}$. The equation for the Green's function $\mathsf{G}(\mathbf{r})$ is

$$\mu\nabla^2\mathsf{G}(\mathbf{r}) + (\mu+\lambda)\nabla(\nabla\cdot\mathsf{G}(\mathbf{r})) + \mathsf{I}\delta(\mathbf{r}) = 0. \tag{2.11}$$

[1] A point force and a monopole are the same thing. A Green's function is the response to a point force.

[2] A multipole expansion is a series in terms of a parameter that decreases as the distance to a fixed position increases.

Its Fourier transform is

$$-\mu k^2 \mathbf{G}(\mathbf{k}) - (\mu+\lambda)\mathbf{k}(\mathbf{k}\cdot\mathbf{G}(\mathbf{k})) + \mathbf{I} = 0, \tag{2.12}$$

or, equivalently,

$$[\mu k^2 \mathbf{I} + (\mu+\lambda)\mathbf{kk}]\cdot\mathbf{G}(\mathbf{k}) = \mathbf{I}. \tag{2.13}$$

After rewriting $\mu k^2\mathbf{I} + (\mu+\lambda)\mathbf{kk}$ explicitly in terms of three-dimensional coordinates, we solve for $\mathbf{G}(\mathbf{k})$. This produces

$$\mathbf{G}(\mathbf{k}) = \frac{1}{\mu k^2}\left[\mathbf{I} - \frac{(\mu+\lambda)\mathbf{kk}}{(2\mu+\lambda)k^2}\right] = \frac{1}{\mu k^2}\left[\mathbf{I} - \frac{\mathbf{kk}}{2(1-\nu)k^2}\right]. \tag{2.14}$$

With

$$\frac{1}{(2\pi)^3}\int \frac{e^{-i\mathbf{k}\cdot\mathbf{r}}}{k^2}\, d^3k = \frac{1}{4\pi r} \tag{2.15}$$

and

$$\frac{1}{(2\pi)^3}\int \frac{e^{-i\mathbf{k}\cdot\mathbf{r}}\mathbf{kk}}{k^4}\, d^3k = \frac{1}{8\pi r}\left(\mathbf{I} - \frac{\mathbf{rr}}{r^2}\right), \tag{2.16}$$

we invert the Fourier transform,

$$\mathbf{G}(\mathbf{r}) = \frac{1}{16\pi\mu(1-\nu)r}\left[(3-4\nu)\mathbf{I} + \frac{\mathbf{rr}}{r^2}\right]. \tag{2.17}$$

If $\mu = \eta$ and $\nu = 1/2$, then we recover $\mathbf{G}(\mathbf{r})$ for Eq. (2.5) such that $\nabla\cdot\mathbf{G}(\mathbf{r}) = 0$,

$$\mathbf{G}(\mathbf{r}) = \frac{1}{8\pi\eta r}\left(\mathbf{I} + \frac{\mathbf{rr}}{r^2}\right), \tag{2.18}$$

also known as the Oseen tensor [57].

2.2.2 Stress plus higher-order terms

Both Eqs. (2.5) and (2.9) can be written as integrals representing $\mathbf{u}(\mathbf{r})$, rather than partial differential equations solvable for $\mathbf{u}(\mathbf{r})$. Intuitively, this is consistent with the idea that a disturbance caused by some rigid body is a superposition of point forces distributed appropriately. Mathematically, it is a consequence of linearity. Let B be

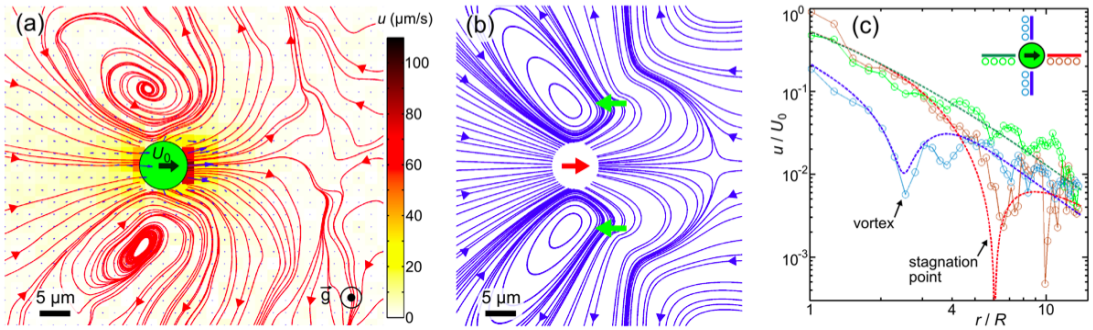

Fig. 2.1: Azimuthal- and time-averaged flow field of a swimming *C. reinhardtii*, from Ref. [58]. The measured flow field (left) was fitted to a simple model consisting of three point forces (middle). This model is a good description for how the magnitude of the flow decays (right).

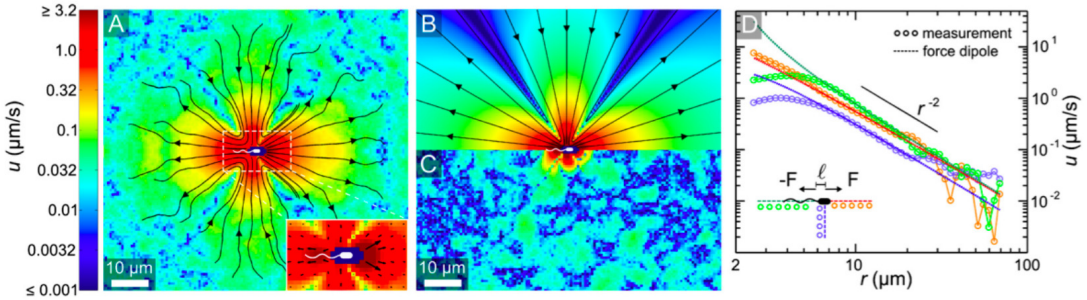

Fig. 2.2: Azimuthal- and time-averaged flow field of a swimming *E. coli*, from Ref. [59]. The measured flow field (left) is mostly dipolar, as indicated with the residual obtained by subtracting the fitted model (middle). At a few micrometres away, the magnitude of the flow decays as r^{-2} (right).

the surface of a rigid body. From either Ref. [60] for a viscous fluid or Ref. [61] for an elastic solid,

$$\mathbf{u}(\mathbf{r}) = \int_B (\boldsymbol{\sigma}(\mathbf{r}') \cdot \hat{\mathbf{n}}) \cdot \mathbf{G}(\mathbf{r} - \mathbf{r}')\, d^2 r', \tag{2.19}$$

where $\hat{\mathbf{n}}$ is a normal pointing outside B. Assuming B lies at the origin, we expand $\mathbf{G}(\mathbf{r} - \mathbf{r}')$ as a Taylor series in $\mathbf{r}'$ about $\mathbf{r}$,

$$\mathbf{G}(\mathbf{r} - \mathbf{r}') = \sum_{n=0}^{\infty} \frac{(-1)^n}{n!} (\mathbf{r}' \cdot \nabla)^n \mathbf{G}(\mathbf{r}). \tag{2.20}$$

Then Eq. (2.19) is

$$\begin{aligned} \mathbf{u}(\mathbf{r}) &= \sum_{n=0}^{\infty} \frac{(-1)^n}{n!} \int_B (\boldsymbol{\sigma}(\mathbf{r}') \cdot \hat{\mathbf{n}}) \cdot [(\mathbf{r}' \cdot \nabla)^n \mathbf{G}(\mathbf{r})]\, d^3 r' \\ &= -\mathbf{F} \cdot \mathbf{G}(\mathbf{r}) + \mathbf{S} : \nabla \mathbf{G}(\mathbf{r}) + \cdots, \end{aligned} \tag{2.21}$$

where $\mathbf{F}$ is the force applied to B,

$$\mathbf{F} = \int_B (\boldsymbol{\sigma}(\mathbf{r}') \cdot \hat{\mathbf{n}})\, d^3 r', \tag{2.22}$$

and $\mathbf{S}$ is the stress arising from B,

$$\mathbf{S} = \int_B (\boldsymbol{\sigma}(\mathbf{r}') \cdot \hat{\mathbf{n}}) \mathbf{r}'\, d^3 r'. \tag{2.23}$$

Without any applied forces, an active particle has $\mathbf{F} = 0$ because it self-propels. This means

$$\mathbf{u}(\mathbf{r}) \simeq \mathbf{S} : \nabla \mathbf{G}(\mathbf{r}). \tag{2.24}$$

In either medium, $\mathbf{u}(\mathbf{r})$ behaves asymptotically like $\nabla \mathbf{G}(\mathbf{r})$, namely $u(r) \sim r^{-2}$ unless $\mathbf{S} = 0$.

How realistic is Eq. (2.24)? Does the field induced by an active particle actually decay as r^{-2}? These questions were recently answered, at least for some typical swimmers [58, 59]. Figs. 2.1 and 2.2 show flow fields measured respectively for the alga *C. reinhardtii* and the bacterium *E. coli* as they swim. It seems the asymptotics from Eq. (2.24) can appear just a few body lengths from a swimmer.

2.3 Gauss or Lévy: a tale of normalcy and stability

We are going to repeatedly intersect with probability and stochastic processes. Separately from active matter, we need to be familiar with some common tools like the central limit theorem and the Fokker-Planck equation, as well as some more exotic concepts like a Lévy flight and the fractional Fokker-Planck equation.

2.3.1 Limit theorems and distributions

The Gaussian, or normal, distribution,

$$P(x) = \frac{e^{-(x-\mu)^2/(2\sigma^2)}}{\sqrt{2\pi}\sigma}, \tag{2.25}$$

is likely to be the most common probability distribution in nature. As is well known, $P(x)$ is fully determined by its mean $\mu = \langle x \rangle$ and variance $\sigma^2 = \langle x^2 \rangle$. Gaussian distributions have many other convenient properties, so an unknown probability distribution is often assumed to be a Gaussian distribution, especially in physics. It seems naive, but sometimes the assumption is justified because of the central limit theorem [62]. This states the probability distribution for a sum of N random variables is a Gaussian distribution in the limit $N \to \infty$, assuming the variance of each random variable is finite. Nevertheless, the central limit theorem only holds asymptotically, it may not always be appropriate. Gabriel Lippman expressed this succinctly in a letter to Henri Poincaré [63]:

> "Everybody believes in the exponential law of errors: the experimenters, because they think it can be proved by mathematics; and the mathematicians, because they believe it has been established by observation."

Like any other tool, the central limit theorem must be used carefully. It is usually stated for independent and identically distributed random variables, which we assume throughout this thesis.

Another limit theorem does exist for a sum of N random variables under a specific condition. Consider, more generally, some family of random variables with the property that any linear combination of them belongs to the same family. We say that such a family is stable. Gaussian random variables are stable, a proof of the central limit theorem invokes this fact indirectly. Cauchy random variables, which follow a Cauchy distribution,

$$P(x) = \frac{c}{\pi[(x-\mu)^2 + c^2]}, \tag{2.26}$$

are also stable. Both probability distributions are special cases of the (symmetric) Lévy stable distribution, defined by its Fourier transform

$$P(k) = e^{ik\mu - (c|k|)^\alpha}, \tag{2.27}$$

where the characteristic exponent α is restricted to $0 \leq \alpha \leq 2$.[3] The parameter c is the scale of $P(k)$, something that is similar to a variance. As $N \to \infty$, a Lévy stable distribution is the probability distribution for a sum of N random variables if the variance of each random variable is infinite. This is the generalized central limit theorem [62, 64]. Again, we assume independent and identically distributed random variables.

2.3.2 Langevin and Fokker-Planck equations

The microscopic world is always subject to fluctuations. A small object often has apparent randomness in its motion, something we model by adding a random force to Newton's second law.

When there are no other forces, the position $x(t)$ of a diffusing particle follows the Langevin equation

$$\frac{m}{\gamma}\frac{d^2}{dt^2}x(t) = -\frac{d}{dt}x(t) + \zeta(t), \tag{2.28}$$

[3] We recover a Gaussian distribution for $\alpha = 2$ and a Cauchy distribution for $\alpha = 1$.

where the particle has mass m and drag coefficient γ. The random force $\zeta(t)$ is distributed according to a Gaussian distribution. It has no mean, $\langle\zeta(t)\rangle = 0$, and no correlations, $\langle\zeta(t)\zeta(t')\rangle = 2D\delta(t-t')$. At a temperature T, we set the diffusion coefficient D from the Stokes-Einstein relation $D = k_bT/\gamma$. Eq. (2.28) is underdamped, when t is typically longer than a few nanoseconds we prefer its overdamped counterpart

$$\frac{d}{dt}x(t) = \zeta(t). \tag{2.29}$$

This is equivalent to the Fokker-Planck equation solvable for the probability distribution $P(x,t)$,

$$\frac{\partial}{\partial t}P(x,t) = D\frac{\partial^2}{\partial x^2}P(x,t), \tag{2.30}$$

also known as the diffusion equation of Brownian motion.

Eq. (2.28) is really just Newton's second law, like we mentioned before. We think of $\zeta(t)$ as representing the interaction between a particle and the countless molecules that surround it. Since molecular collisions happen much faster than the motion of our particle, it is perfectly fine to let $\zeta(t)$ be uncorrelated. But, this is not the general case. Suppose instead $\zeta(t)$ is correlated such that $\langle\zeta(t)\zeta(t')\rangle = C(t-t')$. How does Eq. (2.30) change for this colored noise?

We describe colored Gaussian noise $\zeta(t)$ using a characteristic functional [65], say

$$\mathcal{F}[k(\cdot);t] = \langle e^{i\int_0^t k(t')\zeta(t')\,dt'}\rangle = e^{-\frac{1}{2}\int_0^t\int_0^t k(t')C(t'-t'')k(t'')\,dt'dt''}, \tag{2.31}$$

where we kept $\langle\zeta(t)\rangle = 0$. Given $\mathcal{F}[k(\cdot);t]$, the Fokker-Planck equation is [66]

$$\frac{\partial}{\partial t}P(x,t) = \frac{1}{2}\int_0^t C(t-t')\frac{\partial^2}{\partial x^2}P(x,t')\,dt'. \tag{2.32}$$

It seems remarkable that $P(x,t)$ is so easily determined from $C(t-t')$. After some thought, it becomes clear this just reflects $\zeta(t)$ is Gaussian noise. For a Gaussian distribution, the second moment is all that matters. Speaking about $\zeta(t)$, this role is played by $C(t-t')$.

What happens if $\zeta(t)$ is no longer Gaussian noise? Then, whether or not $\zeta(t)$ is correlated, we still prescribe $\mathcal{F}[k(\cdot);t]$. A classic example is a Lévy flight [67, 68], for which $\zeta(t)$ is drawn from a Lévy stable distribution, such as Eq. (2.27), at any instant in time. By the generalized central limit theorem, $\zeta(t)$ could arise from the sum of many random variables, each of whose probability distribution behaves asymptotically like a power-law. The characteristic functional is, again with $\langle\zeta(t)\rangle = 0$,

$$\mathcal{F}[k(\cdot);t] = e^{-D_\alpha \int_0^t |k(t')|^\alpha \, dt'}. \tag{2.33}$$

In Fourier space, this means [69, 70]

$$\frac{\partial}{\partial t}P(k,t) = -D_\alpha |k|^\alpha P(k,t). \tag{2.34}$$

We usually cannot invert $P(k,t)$ analytically, but $|k|^\alpha$ can be interpreted as the Fourier transform of a fractional derivative. It is equivalent to write Eq. (2.34) as the fractional Fokker-Planck equation [71, 72]

$$\frac{\partial}{\partial t}P(x,t) = -D_\alpha \left(-\frac{\partial^2}{\partial x^2} \right)^{\alpha/2} P(x,t). \tag{2.35}$$

The solution to Eq. (2.35) inherits properties from the underlying Lévy stable noise. More specifically, $\langle x^2(t)\rangle = \infty$. Although Eq. (2.35) is elegant, the diverging moments of $P(x,t)$ do not suggest it is a robust physical model.

Eqs. (2.32) and (2.35) are the state of the art for non-Gaussian stochastic processes that are relevant to us. But, they will not be used at all. This is the problem. A model of fluctuations in active suspensions needs to generalize some aspects of these equations. We do not fully achieve this, though we will make connections with equations from this Section as certain limits.

Chapter 3

Lévy-like Flights and Mixing due to Swimming Microorganisms

3.1 Beyond Brownian motion

Microorganisms may rely on effective mixing strategies to achieve efficient nutrient flux. Some recent experiments revealed that the diffusion of 2 μm tracers is enhanced if they are placed in a dilute suspension of *C. reinhardtii* [73]. This alga is nearly spherical, about 5 μm in radius, and swims at roughly 100 μm s^{-1}. The measured trajectories of swimmers and tracers are shown in Fig. 3.1. The probability distributions of a tracer displacement, as a function of alga concentration, are shown in Fig. 3.2. On the basis of the central limit theorem, we might expect the probability distribution of a tracer displacement to be a Gaussian distribution like that of Brownian motion, except with a larger diffusion coefficient to account for the swimmers. But, the probability distributions have tails that are clearly unlike a Gaussian distribution. What is their origin and structure?

In Chapter 2, we gave Brownian motion as a natural example of the central limit theorem at work. Discovered by Jan Ingenhousz in 1784 [74], colloids that jiggle suddenly became part of physics when Jean Perrin in 1909 [75] used them to prove the atomistic hypothesis. This advance in our understanding of matter happened long before atoms and molecules were directly observable, it was only possible because

William Sutherland [76] and Albert Einstein [77] linked the properties of a fluid to the mean square displacement of a colloid. Caused by many random collisions with molecules in a fluid, the Brownian motion of a colloid is quintessentially Gaussian. We are going to explain why the motion of a tracer in a dilute suspension of swimmers is not. Understanding such an apparent violation of the central limit theorem is a challenging problem, whose solution may provide clues into how microorganisms mix a fluid [11].

Modern microscopy probes the random motion of tiny particles to an ever increasing accuracy [78, 79]. This opens the door to precise experiments that measure the trajectory of a tracer as it is advected by swimmers. Furthermore, a novel class of micromechanical devices are powered with non-equilibrium fluctuations generated by bacteria [80, 81]. To explain and exploit the conditions of active suspensions, it is important to relate the statistics of a tracer and the characteristics of swimmers.

In Ref. [73], the time-dependent probability distributions for a tracer displacement exhibit tails that decay much more slowly than a Gaussian distribution, even though the concentration of swimmers is low. At a high concentration of swimmers, enhanced transport is perfectly reasonable as collective behavior emerges from swimmer interactions, leading to the formation of large vortices and jets [82, 83, 84, 85]. For dilute suspensions, where swimmer-swimmer interactions can be safely neglected, a quantitative description of the underlying statistics has been lacking. We demonstrate the probability distribution for a tracer velocity is well described by a tempered Lévy stable distribution and the long time behavior of the probability distribution for a tracer displacement is similar to that of a Lévy flight. The fundamental ingredient of such non-Gaussian fluctuations is an ultraslow convergence to Gaussian distribution predicted by the central limit theorem.

If a microswimmer is self-propelled, we know from Eq. (2.24) in Chapter 2 that the velocity field scales with distance as r^{-n} for some exponent $n \geq 2$. This power-

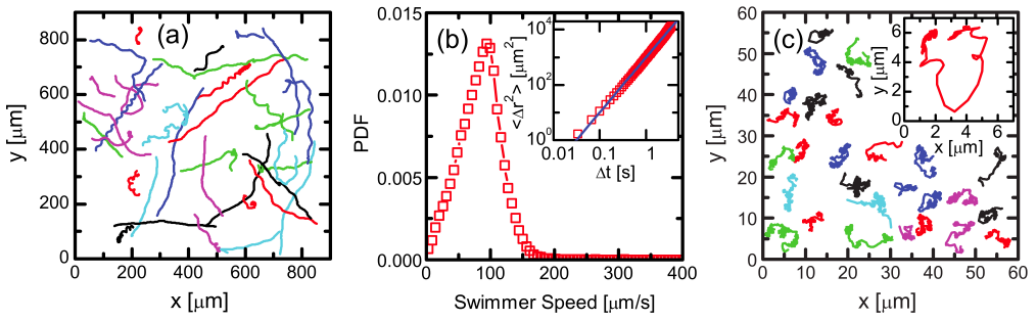

Fig. 3.1: Experimental data from Ref. [73]. (Left) Trajectories of swimmers, over a time interval of 1 s, showing mostly ballistic motion. (Middle) Probability distribution of swimmer speeds, which is sharply speaked about 75 μm s. (Right) Trajectories of tracers, showing large displacements and loop-like structures.

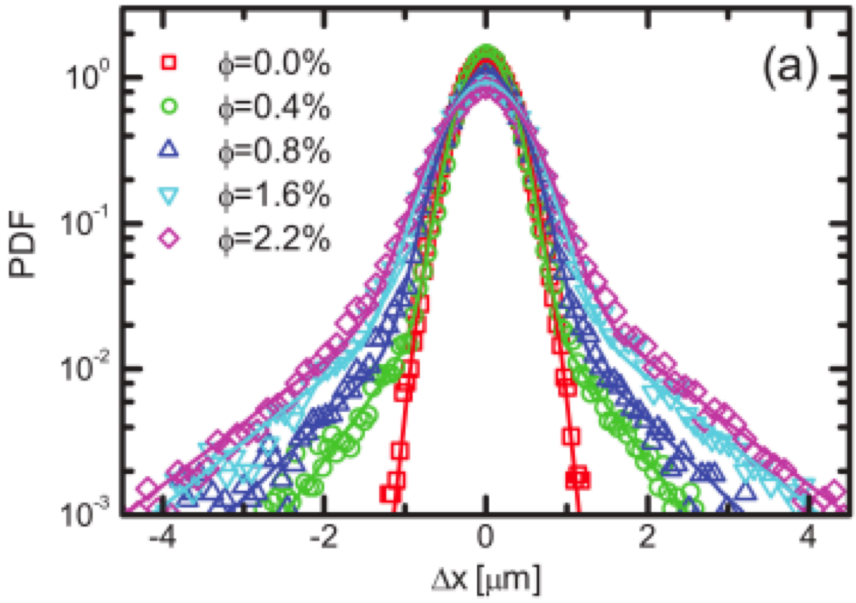

Fig. 3.2: Experimental data from Ref. [73]. The probability distribution of a tracer displacement at different volume fractions, labeled ϕ here but Φ in this Chapter, after 0.12 s has elapsed.

law decay is responsible for the non-Gaussian diffusion of tracers. Interestingly, very different behavior may occur in suspensions of sedimenting swimmers: should gravity play a role in the dynamics, the velocity fields decay like r^{-1} and a tracer will diffuse normally.[1] Finally, our results suggest that, on sufficiently long times scales, tracer diffusion in dilute active suspensions can be viewed as a natural example of a stochastic process described by a tempered fractional diffusion equation.

3.2 Models and assumptions

Given an advecting flow $\mathbf{u}(\mathbf{r}, t)$, we model the position $\mathbf{r}(t)$ of a tracer by the overdamped Langevin equation

$$\frac{d}{dt}\mathbf{r}(t) = \mathbf{u}(\mathbf{r}(t), t) + \boldsymbol{\zeta}(t). \tag{3.1}$$

The random term $\boldsymbol{\zeta}(t)$ is the usual Gaussian noise, for which $\langle \boldsymbol{\zeta}(t) \rangle = 0$ and $\langle \boldsymbol{\zeta}(t)\boldsymbol{\zeta}(t') \rangle = 2D\delta(t - t')\mathbf{I}$. It describes molecular collisions between the tracer and the surrounding fluid. The diffusion coefficient D in a fluid of viscosity η is determined from the Stokes-Einstein relation $D = k_b T/(6\pi\eta a)$, where a is the tracer radius.

If the Reynolds number is very small, then the net flow due to N active swimmers, each located at a position $\mathbf{r}_i(t)$ and moving at a velocity $\mathbf{v}_i$, is the sum of all flow fields $\mathbf{u}_i(\mathbf{r}, t)$,

$$\mathbf{u}(\mathbf{r}, t) = \sum_{i=1}^{N} \mathbf{u}_i(\mathbf{r}, t). \tag{3.2}$$

Since we are interested in conditions similar to those of Ref. [73], we focus on a suspension of active particles in the limit of a small volume fraction Φ, that is $\Phi \ll 1$.[2] For this case, binary encounters between swimmers are negligible perturbations. Moreover, we ignore the random reorientation of swimmers caused by rotational diffusion

[1] This was confirmed experimentally after this Chapter had been submitted for publication [86].

[2] More generally, this criterion may depend on the swimmer velocity, meaning it is likely to be more stringent than $\Phi \ll 1$.

(due to thermal fluctuations) and search behavior (like chemotaxis or phototaxis). Statistically speaking, it is irrelevant to some quantities whether a tracer experiences two successive scatterings from one tumbling swimmer or from two non-tumbling swimmers. We therefore assume that all of the swimmers move ballistically,

$$\mathbf{r}_i(t) = \mathbf{r}_i(0) + \mathbf{v}_i t. \tag{3.3}$$

The initial conditions for each swimmer, $\mathbf{r}_i(0)$ and $\mathbf{v}_i$, are independent and identically distributed random variables. We take the probability distribution of each initial position $\mathbf{r}_i(0)$ as a uniform distribution in space. All of the swimmers have the same speed v.

To complete our model, we must specify the flow field $\mathbf{u}_i(\mathbf{r}, t)$ generated by each swimmer. There are various strategies for achieving directed propulsion at the microscale [87]. Microorganisms, like algae and bacteria, can swim by moving slender filaments in a manner not the same under time reversal. Self-motile colloids, a class of miniature artificial swimmers, are powered with interfacial forces induced from the environment [88]. Although both of these are active particles, microscopic details of their geometry and self-propulsion can lead to quite different velocity fields. This, in turn, affects how a tracer migrates in their flow. In Stokes flow, without external forces, the most important feature of the velocity field caused from a self-propelled colloid or microorganism is that it decays asymptotically as r^{-2} or faster. Since we are interested in the general features of mixing by active suspensions, and there is no universal description of the flow around an active particle, it is helpful to consider simplified velocity fields that capture generic features of real microflows. We restrict ourselves to the case of neutrally buoyant swimmers, for which there is no r^{-1} term in the flow field.

We focus on two models, see Fig. 3.3, that can be interpreted as contributions to a general multipole expansion of a velocity field. Specifically, we compare a co-oriented

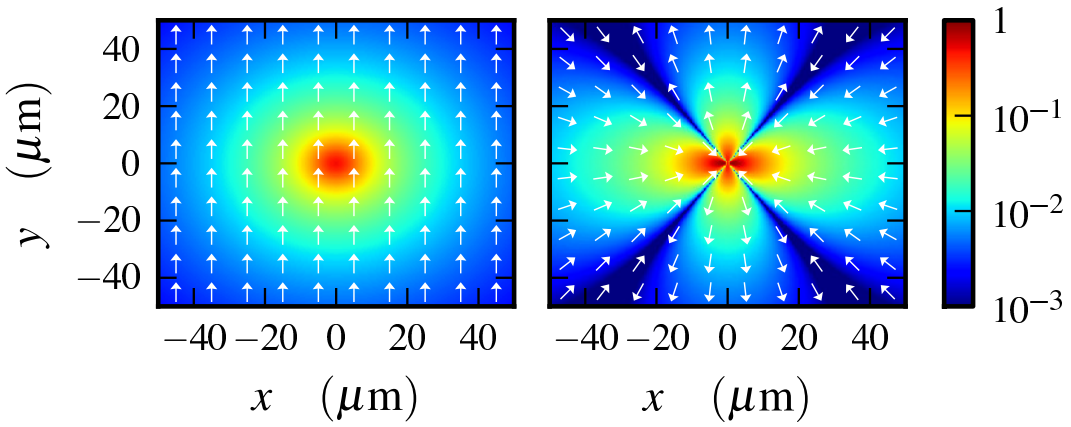

Fig. 3.3: Flow fields of the model swimmers considered in our analytical and numerical calculations. In both plots, the swimmer is oriented upwards and the flow is normalized by the swimming speed. The arrows indicate velocity direction and the colors represent magnitude. Co-oriented model with r^{-2} decay (left) and stroke-averaged flow generated by a dipolar "pusher" (right). Parameters are listed in Fig. 3.4.

'toy' model [89] with a trivial angular dependence,

$$\mathbf{u}_i(\mathbf{r}(t),t) = \frac{\kappa^n q v \hat{\mathbf{n}}_i}{d_i(t)^n + \epsilon^n}, \tag{3.4}$$

against a more realistic dipolar model [90],

$$\mathbf{u}_i(\mathbf{r}(t),t) = \frac{\kappa^2 q v [1 - 3(\hat{\mathbf{d}}_i(t)\cdot\hat{\mathbf{n}}_i)^2]\hat{\mathbf{d}}_i(t)}{d_i(t)^2 + \epsilon^2}. \tag{3.5}$$

In Eqs. (3.4) and (3.5), the vector $\mathbf{d}_i(t) = \mathbf{r}_i(t) - \mathbf{r}(t)$ connects the swimmer and tracer position at a time t, $\hat{\mathbf{d}}_i(t) = \mathbf{d}_i(t)/d_i(t)$ is the associated unit vector, and $\hat{\mathbf{n}}_i = \mathbf{v}_i/v$ defines the swimmer's orientation. The parameter κ characterizes the swimmer length scale, q is a dimensionless constant that relates the amplitude of the velocity field to the swimmer speed, and ϵ regularizes the singularity of the velocity field at small distances. The co-oriented model of Eq. (3.4), due to its minimal angular dependence, is useful for pinpointing how the tracer statistics depend on the distance scaling of the velocity field. For $n = 1$, the scaling is equivalent to that of a sedimenting colloid or forced swimmer, whereas for $n \geq 2$ the scaling resembles that of various natural swimmers not subject to an external force. The case $n = 2$ allows

us to ascertain the effects of the angular details in the velocity field on tracer diffusion, by checking against the more realistic dipolar model of Eq. (3.5). The latter is often considered as a simple stroke-averaged description for microswimmers [38, 40]. As shown in Ref. [89], stroke-averaged models are able to capture the most important aspects of the tracer dynamics on time scales longer than the swimming stroke of a microorganism.

Our interest is in statistical properties of tracers that are accessible to experiments, such as the velocity probability distribution, correlation functions, and the position probability distribution. These are obtained by averaging suitably defined functions with respect to a probability distribution for the initial conditions of all swimmers,

$$f(r_1,\ldots,r_N,v_1,\ldots,v_N) = \frac{3\Theta(R-r_1)}{4\pi R^3}\cdots\frac{3\Theta(R-r_N)}{4\pi R^3} \times \frac{\delta(v_1-v)}{4\pi v_1^2}\cdots\frac{\delta(v_N-v)}{4\pi v_N^2}, \tag{3.6}$$

where $\Theta(x)$ is the Heaviside theta function and R is the radius of some large spherical container. Assuming that each swimmer is a sphere of radius κ, we estimate the volume fraction as $\Phi = N(\kappa/R)^3$. Generally, we work in the thermodynamic limit, for which $N \to \infty$ and $R \to \infty$ at a fixed Φ.

We first consider the velocity probability distribution at a fixed point in time and the velocity autocorrelation function at a fixed point in space. These quantities are independent of thermal noise, which we have to include later for the mean square displacement and position probability distribution of a tracer. Considering a suspension of N swimmers inside a spherical volume of radius R, the velocity probability distribution and the velocity autocorrelation function are formally defined by

$$W(\mathbf{u}) = \langle \delta(\mathbf{u} - \mathbf{u}(0,0)) \rangle \tag{3.7}$$

and

$$C(t) = \langle \mathbf{u}(0,t) \cdot \mathbf{u}(0,0) \rangle, \tag{3.8}$$

where the angular brackets indicate an average with respect to $f(r_1, \ldots, r_N, v_1, \ldots, v_N)$ of Eq. (3.6). We investigate $W(\mathbf{u})$ and $C(t)$ for both the co-oriented and dipolar model, that is Eqs. (3.4) and (3.5) respectively.

In what follows, we mostly use the characteristic function $W(\mathbf{k})$ of the velocity probability distribution, which is defined as

$$W(\mathbf{k}) = \int e^{i\mathbf{k}\cdot\mathbf{u}} W(\mathbf{u})\, d^3u. \tag{3.9}$$

Then, taking the inverse Fourier transform, we recover

$$W(\mathbf{u}) = \frac{1}{(2\pi)^3} \int e^{-i\mathbf{k}\cdot\mathbf{u}} W(\mathbf{k})\, d^3k. \tag{3.10}$$

Given $W(\mathbf{k})$, any moment of $W(\mathbf{u})$ follows by differentiating appropriately. For example, the second and fourth velocity moments are

$$\langle u^2 \rangle = -\nabla^2 W(\mathbf{k})|_{\mathbf{k}=0}, \tag{3.11a}$$

$$\langle u^4 \rangle = (\nabla^2)^2 W(\mathbf{k})|_{\mathbf{k}=0}. \tag{3.11b}$$

As our suspension of swimmers is statistically isotropic, we expect $W(\mathbf{u}) = W(u)$ and $W(\mathbf{k}) = W(k)$. So, the differential operators in Eqs. (3.11) become

$$\nabla^2 = \frac{\partial^2}{\partial k^2} + \frac{2}{k}\frac{\partial}{\partial k}, \tag{3.12a}$$

$$(\nabla^2)^2 = \left(\frac{\partial^2}{\partial k^2} + \frac{2}{k}\frac{\partial}{\partial k}\right)^2 = \frac{\partial^4}{\partial k^4} + \frac{2}{k}\frac{\partial^3}{\partial k^3} - \frac{1}{k^2}\frac{\partial^2}{\partial k^2} + \frac{1}{k^3}\frac{\partial}{\partial k}, \tag{3.12b}$$

due to radial symmetry.

We will show that the velocity probability distribution of a tracer in the presence of active swimmers can be approximated by a tempered Lévy stable distribution, whose characteristic function is

$$W(k) = e^{-[(\chi k^2 + \lambda^2)^{\alpha/2} - \lambda^\alpha]}. \tag{3.13}$$

This probability distribution has the second and fourth moments

$$\langle u^2 \rangle = 3\alpha\chi\lambda^{\alpha-2}, \tag{3.14a}$$

$$\langle u^4 \rangle = 15\alpha\chi^2\lambda^{\alpha-4}[2 + \alpha(\lambda^\alpha - 1)]. \tag{3.14b}$$

The tempered Lévy stable distribution of Eq. (3.13) reduces to either the Gaussian distribution from the central limit theorem as λ becomes large (many swimmers) or the Lévy stable distribution from the generalized central limit theorem [64] as $\lambda \to 0$ (unregularized swimmers).

Using the Euler method of integration, we simulate an "ideal gas" of swimmers that move according to Eq. (3.3) inside a sphere of radius R. This sphere is always relative to the tracer, whose position evolves according to Eq. (3.1). If a swimmer leaves the sphere, then we immediately delete it. In order to keep our suspension statistically homogeneous and isotropic, we continually insert new swimmers at the boundary of the sphere. The number of insertions j per time step is drawn from a Poisson distribution $\Gamma^j e^{-\Gamma}/j!$, where Γ is the mean number of insertions during Δt. We obtain equilibrium by setting Γ equal to the mean number of deletions during Δt, which may be estimated from the kinetic theory of gases [91] as $\Gamma = [3NV/(4R)]\Delta t$. For each insertion, it is necessary to bias the orientation of an active particle so that the conditional probability distribution of $\hat{\mathbf{n}}_i$ given $\hat{\mathbf{r}}_i$ is proportional to $\hat{\mathbf{n}}_i \cdot \hat{\mathbf{r}}_i$. We achieve that by uniformly choosing a position $\hat{\mathbf{r}}_i$ at a distance R relative to the tracer, then choosing an orientation from a probability distribution $g(\hat{\mathbf{n}}_i \mid \hat{\mathbf{r}}_i) \propto \hat{\mathbf{r}}_i \cdot \hat{\mathbf{n}}_i$ that is normalized over the solid angle of a hemisphere with inward surface normal $\hat{\mathbf{r}}_i$. Generally, our procedure achieves numerical accuracy if R is large. It also ensures that a suspension of ballistic particles remains homogeneous and isotropic with mean population N. The validity of this approached is justified by comparing against exact results for the time-dependent velocity autocorrelation function.

Resolving the tail of a probability distribution can be a computationally expensive task, even for stochastic processes that are relatively simple. In our numerical simulations, further difficulties arise from having to create and maintain an active suspension unique to each tracer. This process would not be possible in a reasonable amount of time on a traditional computer. We therefore implemented parallelized

simulations on a graphics processing unit (GPU) using NVIDIA's Compute Unified Device Architecture (CUDA). Compared to a single-core CPU, GPU code yields substantial speed-ups (up to a factor of a few hundreds). However, our longest simulation still took two weeks on a GPU.

3.3 The velocity probability distribution and its ultraslow convergence

Why are there anomalous statistics in a suspension of swimmers? To answer this question, we consider the probability distribution $w(u)$ of the instantaneous velocity imparted to a tracer when there is only a single swimmer present,

$$w(u) = \langle \delta(u - u_1(0,0)) \rangle, \tag{3.15}$$

where $\mathbf{u}_1(\mathbf{r}, t)$ is taken from either Eq. (3.4) or (3.5). The tail of $w(u)$ reflects large velocities that come out of a close encounter with the swimmer. It is helpful to think about the limit $\epsilon \to 0$, for which $\mathbf{u}_1(\mathbf{r}, t)$ diverges at small distances and $w(u)$ lacks a cutoff at large velocities. By a change of variables in Eq. (3.15), we derive $w(u) \sim u^{-3-3/n}$.[3] This means the variance of $w(u)$ is finite for $n = 1$, but infinite for $n \geq 2$. According to Eq. (3.2), the velocity field from N swimmers is the sum of N independent and identically distributed random variables. So the central limit theorem predicts $W(u)$ converges to a Gaussian distribution for $n = 1$. While $\epsilon = 0$, the central limit theorem does not apply for $n \geq 2$ because $w(u)$ has an infinite variance.

If $\epsilon > 0$, then $\mathbf{u}_1(\mathbf{r}, t)$ is strongly increasing in the vicinity of the swimmer [58, 92], but remains finite due to lubrication effects and a nonzero size. Since the variance of $w(u)$ no longer diverges, the conditions of the central limit theorem are satisfied

[3] You can see the details of this calculation in Chapter 4.

for all $n \geq 1$. Nevertheless, for $n \geq 2$, the variance of $w(u)$ is very large and the convergence to a Gaussian distribution is very slow.

These statements are illustrated in Figs. 3.4 and 3.5, containing $W(u)$ obtained from numerical simulations and analytic approximations at different volume fractions of swimmers. As evident in Fig. 3.4 A, for $n = 1$, $W(u)$ converges rapidly to a Gaussian distribution. However, for velocity fields decaying as r^{-n} with $n \geq 2$, the convergence is surprisingly slow and there are strongly non-Gaussian features if Φ is small. The arrows highlight this regime, which shows a power-law dependence in $W(u)$ on the magnitude of u, a signature of a Lévy stable distribution.

Such an ultraslow convergence to a Gaussian distribution can be described quantitatively using the tempered Lévy stable distribution defined with Eq. (3.13). The parameters χ and λ are estimable in terms of $\langle u^2 \rangle$ and $\langle u^4 \rangle$, which can be calculated explicitly, from solving Eqs. (3.14). By studying the asymptotic behavior as $\epsilon \to 0$, we find that, for velocity fields decaying as r^{-n}, $\alpha = 2$ if $n = 1$ and $\alpha = 3/n$ if $n \geq 2$. In this limit, Eq. (3.13) reduces to a Lévy stable distribution for $n \geq 2$. As discussed in Chapter 2, a Lévy stable distribution arises from the generalized central limit theorem, relevant only to random variables having an infinite variance [64]. This is unrealistic here, as ϵ should be nonzero.

The solid curves in Fig. 3.4 correspond to Eq. (3.13) with the appropriate χ and λ. For $u(\mathbf{r}, t) \sim r^{-2}$, the central limit theorem only becomes accurate at large volume fractions, say $\Phi > 25\%$. In the dilute regime, say $\Phi \ll 1$, the bulk of the probability comes from a Lévy stable distribution before it crosses over to a faster decay. A truncated Lévy stable distribution behaves similarly [93].

3.3.1 Co-oriented model

For the co-oriented model, we now show how to approximate the velocity probability distribution by a tempered Lévy stable distribution. Later we do the same for the

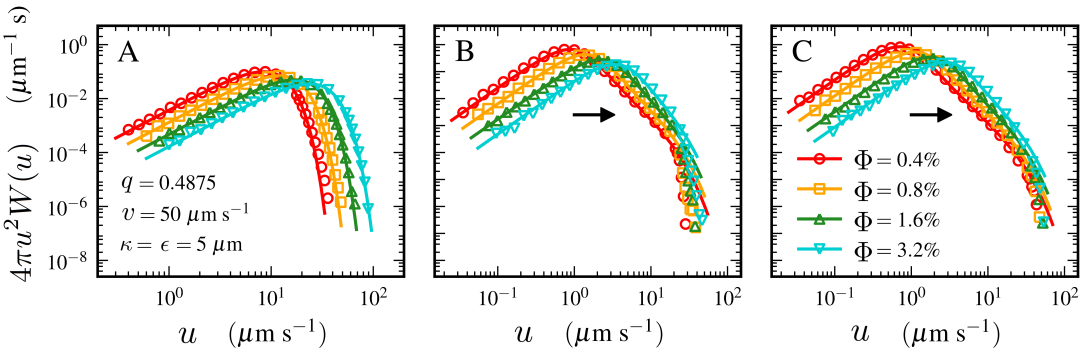

Fig. 3.4: Velocity probability distribution of a tracer in the flow generated by different volume fractions of swimmers. The solid curves are based on Eq. (3.13), using the exact second and fourth moments derived from either Eq. (3.4) or (3.5). (A) For the co-oriented model with $n = 1$, the velocity probability distributions measured in simulations (symbols) converge rapidly to the Gaussian distribution predicted by the central limit theorem (solid curves), even at small volume fractions. (B) For the co-oriented model with $n = 2$, the convergence to a Gaussian distribution is very slow and the velocity probability distributions exhibit strongly non-Gaussian features at volume fractions similar to those in Ref. [73]. (C) The velocity probability distributions for the dipolar model look very similar to that of our co-oriented model (B), which means the angular dependence does not play an important role. Simulation parameters are given in A and C, the sample size is $2^{22} = 4194304$ throughout. In Fig. 3.5, the one-dimensional data of A and B is displayed as a semi-logarithmic plot.

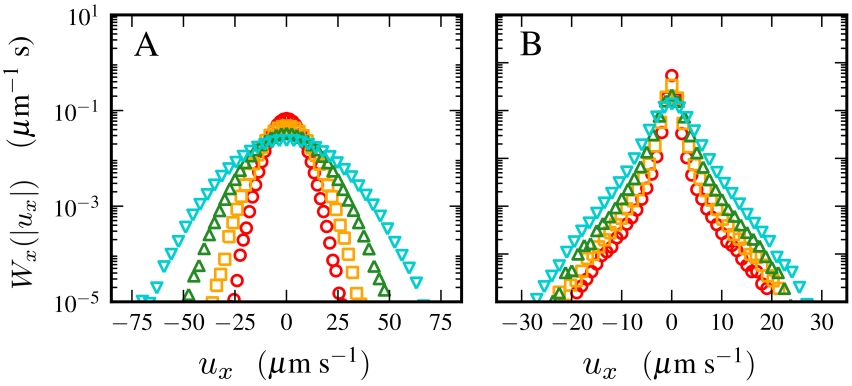

Fig. 3.5: Marginal velocity probability distribution of a tracer in the flow generated by different volume fractions of swimmers, for the co-oriented model with (A) $n = 1$ and (B) $n = 2$. Here $W_x(|u_x|)$ is obtained from $W(u)$ be integrating over u_y and u_z. These one-dimensional probability distributions reflect the Gaussian or Lévy stable nature of their corresponding three-dimensional probability distributions. Symbols and parameters are those of Fig. 3.4.

dipolar model.

Using the Fourier transform of the Dirac delta function, we rewrite Eq. (3.7) as

$$W(u) = \frac{1}{(2\pi)^3}\int e^{-i\mathbf{k}\cdot\mathbf{u}} \times \left[\int \exp\left(-i\mathbf{k}\cdot\sum_{i=1}^{N}\mathbf{u}_i(0,0)\right) d^3r_1\cdots d^3r_N d^3v_1\cdots d^3v_N\right] d^3k. \tag{3.16}$$

Since the positions $\mathbf{r}_1,\ldots,\mathbf{r}_N$ and velocities $\mathbf{v}_1,\ldots,\mathbf{v}_N$ are independent and identically distributed random variables, we just need a single integral over, say, $\mathbf{r}$ and $\mathbf{v}$. With $\mathbf{r} = r\hat{\mathbf{r}}$ and $\mathbf{v} = v\hat{\mathbf{n}}$,

$$W(u) = \frac{1}{(2\pi)^3}\int e^{-i\mathbf{k}\cdot\mathbf{u}} \times \left[\frac{3}{4\pi R^3}\int \exp\left(\frac{iq\kappa^n v\hat{\mathbf{n}}\cdot\mathbf{k}}{r^n+\epsilon^n}\right) r^2\, dr d^3v\right]^N d^3k. \tag{3.17}$$

Let $\epsilon' = \epsilon/R$, $\kappa' = \kappa/R$, and $r' = r/R$. Performing the angular integration of Eq. (3.17) gives

$$W(u) = \frac{1}{(2\pi)^3}\int e^{-i\mathbf{k}\cdot\mathbf{u}} W(k)\, d^3k, \tag{3.18}$$

where $W(k)$ is the characteristic function of $W(u)$,

$$W(k) = \left[3\int_0^1 \frac{\sin(A(r')k)}{A(r')k} r'^2\, dr'\right]^N. \tag{3.19}$$

The function $A(r')$ is

$$A(r') = \frac{\kappa'^n qv}{r'^n+\epsilon'^n}. \tag{3.20}$$

It is sometimes helpful to rewrite $W(k)$ in an equivalent form,

$$W(k) = \left[3\int_0^1\int_0^1 \cos(A(r')k\xi) r'^2\, d\xi dr'\right]^N = w(k)^N, \tag{3.21}$$

recalling that $w(k)$ is the characteristic function for the case of a single swimmer.

Note, assuming m is a nonnegative integer,

$$\frac{\partial^{2m}}{\partial k^{2m}} w(k)\bigg|_{k=0} = \frac{3(-1)^m}{2m+1}\int_0^1 A(r')^{2m} r'^2\, dr', \tag{3.22a}$$

$$\frac{\partial^{2m-1}}{\partial k^{2m-1}} w(k)\bigg|_{k=0} = 0, \tag{3.22b}$$

and

$$\lim_{k\to 0}\frac{1}{k}\frac{\partial^{2m-1}}{\partial k^{2m-1}}w(k)=\frac{3(-1)^m}{2m+1}\int_0^1 A(r')^{2m}r'^2\,dr'=\left.\frac{\partial^{2m}}{\partial k^{2m}}w(k)\right|_{k=0}. \tag{3.23}$$

From these expressions, we have

$$\left.\frac{\partial}{\partial k}W(k)\right|_{k=0}=0, \tag{3.24a}$$

$$\left.\frac{\partial^2}{\partial k^2}W(k)\right|_{k=0}=N\left.\frac{\partial^2}{\partial k^2}w(k)\right|_{k=0}, \tag{3.24b}$$

$$\left.\frac{\partial^3}{\partial k^3}W(k)\right|_{k=0}=0, \tag{3.24c}$$

$$\left.\frac{\partial^4}{\partial k^4}W(k)\right|_{k=0}=3N(N-1)\left.\left(\frac{\partial^2}{\partial k^2}w(k)\right)^2\right|_{k=0}+N\left.\frac{\partial^4}{\partial k^4}w(k)\right|_{k=0}. \tag{3.24d}$$

Then

$$\nabla^2W(k)|_{k=0}=3N\left.\frac{\partial^2}{\partial k^2}w(k)\right|_{k=0}, \tag{3.25a}$$

$$(\nabla^2)^2W(k)|_{k=0}=15N(N-1)\left.\left(\frac{\partial^2}{\partial k^2}w(k)\right)^2\right|_{k=0}+5N\left.\frac{\partial^4}{\partial k^4}w(k)\right|_{k=0}, \tag{3.25b}$$

both of which hold for any radially symmetric probability distribution in three dimensions.

Eqs. (3.25) lead to exact formulas for the velocity moments,

$$\langle u^2\rangle=3N\int_0^1 A(r')^2r'^2\,dr', \tag{3.26a}$$

$$\langle u^4\rangle=\frac{5(N-1)}{3N}\langle u^2\rangle^2+3N\int_0^1 A(r')^4r'^2\,dr'. \tag{3.26b}$$

After integrating, we have

$$\int_0^1 A(r')^2 r'^2\, dr' = \frac{(qv)^2}{n}\left(\frac{\kappa}{\epsilon}\right)^{2n} \times \left[\frac{\epsilon'^n}{1+\epsilon'^n} + \frac{n-3}{3}\,{}_2F_1\left(1, \frac{3}{n}; 1+\frac{3}{n}; -\frac{1}{\epsilon'^n}\right)\right], \tag{3.27a}$$

$$\int_0^1 A(r')^4 r'^2\, dr' = \frac{(qv)^4}{6n^3}\left(\frac{\kappa}{\epsilon}\right)^{4n} \times \left\{\frac{3(n-1)}{(1+\epsilon'^n)^3}\left[(2n-3)\epsilon'^n + (5n-6)\epsilon'^{2n} + \frac{9-18n+11n^2}{3(n-1)}\epsilon'^{3n}\right] + (n-1)(n-3)(2n-3)\,{}_2F_1\left(1, \frac{3}{n}; 1+\frac{3}{n}; -\frac{1}{\epsilon'^n}\right)\right\}. \tag{3.27b}$$

In the most interesting case, which is $n = 2$,

$$\int_0^1 A(r')^2 r'^2\, dr' = \frac{\kappa'^4}{2}\left(\frac{\operatorname{arccot}\epsilon'}{\epsilon'} - \frac{1}{1+\epsilon'^2}\right), \tag{3.28a}$$

$$\int_0^1 A(r')^4 r'^2\, dr' = \frac{1}{16}\left(\frac{\kappa'}{\epsilon}\right)^4\left[\frac{\operatorname{arccot}\epsilon'}{\epsilon'} + \frac{1-\epsilon'^2}{(1+\epsilon'^2)^2} + \frac{8\epsilon'^2}{3(1+\epsilon'^2)^3}\right]. \tag{3.28b}$$

The first integral, and therefore $\langle u^2\rangle$, diverges as $1/\epsilon$ if $\epsilon \to 0$ More precisely, this limit gives

$$\langle u^2\rangle \simeq \frac{3\pi\kappa(qv)^2\Phi}{4\epsilon}, \tag{3.29a}$$

$$\langle u^4\rangle \simeq \frac{3\pi\kappa^5(qv)^4\Phi}{32\epsilon^5}, \tag{3.29b}$$

at leading order in ϵ/R.

We seek to approximate $W(k)$ from Eq. (3.21) by the tempered Lévy stable distribution of Eq. (3.13). At small k, this behaves like a Gaussian distribution,

$$W(k) \simeq e^{-\alpha\chi\lambda^{\alpha-2}k^2/2}. \tag{3.30}$$

To motivate, we rewrite Eq. (3.16) as $W(k) = e^{-N\log w(k)}$, then consider the limit $\epsilon \to 0$. The double integral in Eq. (3.21) can be calculated exactly. By expanding for a large volume $R \gg \epsilon$, we recover a Gaussian distribution if $n = 1$,

$$W(k) \simeq \exp\left[-\frac{N(\kappa' qvk)^2}{2}\right]. \tag{3.31}$$

In contrast, the limit distribution is a Lévy stable distribution if $n \geq 2$,

$$W(k) \simeq \exp[-\omega_n N \kappa'^3 (qv)^{3/n}], \tag{3.32}$$

where ω_n is a numerical constant. Note $\omega_2 = \sqrt{8\pi}/5$ and $\omega_3 = \pi/4$. Taking $\lambda \to 0$ in Eq. (3.13), we obtain

$$W(k) = e^{-\chi^{\alpha/2} k^\alpha}. \tag{3.33}$$

Comparing Eq. (3.31) to (3.30) and Eq. (3.32) to (3.33), we see $\alpha = 2$ if $n = 1$ and $\alpha = 3/n$ if $n \geq 2$.

Before estimating the values of χ and λ, it is worth mentioning that $\log W(k)$ scales with R differently for $n = 1$ and $n \geq 2$. If $n = 1$, then $\log W(k)$ is proportional to the area fraction $N(\kappa/R)^2$, see Eq. (3.31). If $n \geq 2$, then $\log W(k)$ is proportional to the volume fraction $N(\kappa/R)^3$, see Eq. (3.32). This implies, for $n = 1$, the thermodynamic limit corresponds to $N \to \infty$ and $R \to \infty$ while $N(\kappa/R)^2$ is kept fixed, but, for $n \geq 2$, it corresponds to $N \to \infty$ and $R \to \infty$ while $N(\kappa/R)^3$ is kept fixed.

We are ready to illustrate how to find χ and λ, which is done specifically for $n = 1$, $n = 2$, and $n = 3$. If $n = 1$, then it is mostly straightforward. If $n = 2$ or $n = 3$, then the second and fourth velocity moments of the tempered Lévy stable distribution, Eqs. (3.14), are matched against the same exact moments, Eqs. (3.26).

$n = 1$: Take $\alpha = 2$. Eq. (3.13) reduces to a Gaussian distribution in the thermodynamic limit,

$$\lim_{N\to\infty, R\to\infty} W(k) = e^{-\chi k^2}. \tag{3.34}$$

By comparing against Eq. (3.30),

$$\chi = \frac{N(\kappa' qv)^2}{2}(1 + \epsilon' + 2\epsilon' \log \epsilon'), \tag{3.35}$$

where we included further corrections in ϵ'.

$n = 2$: Take $\alpha = 3/2$. Eqs. (3.14) become

$$\langle u^2 \rangle = \frac{9\chi}{2\lambda^{1/2}}, \tag{3.36a}$$

$$\langle u^4 \rangle = \frac{45\chi[2 + 3(\lambda^{3/2} - 1)]}{2\lambda^{5/2}}. \tag{3.36b}$$

Solving these equations for χ and λ yields

$$\chi = \frac{2}{9}\left(\frac{5}{3}\right)^{1/3} \frac{\langle u^2 \rangle^{5/3}}{(3\langle u^4 \rangle - 5\langle u^2 \rangle^2)^{1/3}}, \tag{3.37a}$$

$$\lambda = \left(\frac{5}{3}\right)^{2/3} \frac{\langle u^2 \rangle^{4/3}}{(3\langle u^4 \rangle - 5\langle u^2 \rangle^2)^{2/3}}. \tag{3.37b}$$

Inserting $\langle u^2 \rangle$ and $\langle u^4 \rangle$ from Eqs. (3.26) gives the values used in Fig. 3.4 A. By expanding,

$$\chi \simeq \frac{1}{3}\left(\frac{5\pi^4}{12}\right)^{1/3} (qv)^2 \Phi^{4/3}, \tag{3.38a}$$

$$\lambda \simeq \left(\frac{10\pi}{3}\right)^{2/3} \left(\frac{\epsilon}{\kappa}\right)^2 \Phi^{2/3}, \tag{3.38b}$$

for $R \gg \epsilon$ and $R \gg \kappa$.

$n = 3$: Take $\alpha = 1$. Eqs. (3.14) become

$$\langle u^2 \rangle = \frac{3\chi}{\lambda}, \tag{3.39a}$$

$$\langle u^4 \rangle = \frac{15\chi^2(1 + \lambda)}{\lambda^3}. \tag{3.39b}$$

Solving these equations for χ and λ yields

$$\chi = \frac{5\langle u^2 \rangle^3}{9\langle u^4 \rangle - 15\langle u^2 \rangle^2}, \tag{3.40a}$$

$$\lambda = \frac{5\langle u^2 \rangle^2}{3\langle u^4 \rangle - 5\langle u^2 \rangle^2}. \tag{3.40b}$$

Inserting $\langle u^2 \rangle$ and $\langle u^4 \rangle$ from Eqs. (3.26), then expanding

$$\chi \simeq \frac{5(qv)^2\Phi^2}{3}, \tag{3.41a}$$

$$\lambda \simeq 5\left(\frac{\epsilon}{\kappa}\right)^3 \Phi, \tag{3.41b}$$

for $R \gg \epsilon$ and $R \gg \kappa$.

As $\epsilon \to 0$, the parameter λ vanishes in both Eqs. (3.38) and (3.41). This causes $\langle u^2 \rangle$ to diverge. It indicates there is an ultraslow convergence to a Gaussian distribution for $n \geq 2$. Figs. 3.4 and 3.5 show exactly this.

3.3.2 Dipolar model

We now perform similar calculations for the dipolar model.

Again, with $\mathbf{r} = r\hat{\mathbf{r}}$ and $\mathbf{v} = v\hat{\mathbf{n}}$,

$$W(u) = \frac{1}{(2\pi)^3} \int e^{-i\mathbf{k}\cdot\mathbf{u}} \times \left[\frac{3}{(4\pi)^2 R^3} \int \exp\left(\frac{i\kappa^2 qv[3(\hat{\mathbf{r}}\cdot\hat{\mathbf{n}})^2 - 1]\hat{\mathbf{r}}\cdot\mathbf{k}}{r^2+\epsilon^2} \right) r^2 \, dr d^3v \right]^N d^3k. \tag{3.42}$$

Set $\epsilon' = \epsilon/R$, $\kappa' = \kappa/R$, $r' = r/R$ and $\gamma = \hat{\mathbf{r}}\cdot\hat{\mathbf{n}}$. Then

$$W(u) = \frac{1}{(2\pi)^3} \int e^{-i\mathbf{k}\cdot\mathbf{u}} W(k) \, d^3k, \tag{3.43}$$

for which

$$W(k) = \left[\frac{3}{2} \int_0^1 \int_{-1}^1 \int_0^1 \cos(B(r',\gamma)k\xi) r'^2 \, d\gamma d\xi dr' \right]^N = w(k)^N. \tag{3.44}$$

Above we chose $\mathbf{k} = k\hat{\mathbf{z}}$. The function $B(r',\gamma)$ is

$$B(r',\gamma) = \frac{\kappa^2 \epsilon'^2 (3\gamma^2 - 1)}{r'^2 + \epsilon'^2}. \tag{3.45}$$

The moments of the velocity probability distribution can be extracted from Eq. (3.44)

Applying Eqs. (3.25) to Eq. (3.44) produces the exact second and fourth velocity moments,

$$\langle u^2 \rangle = \frac{6(\kappa' qv)^2 N}{5} \left(\frac{\operatorname{arccot} \epsilon'}{\epsilon'} - \frac{1}{1+\epsilon'^2} \right), \tag{3.46a}$$

$$\langle u^4 \rangle = \frac{5(N-1)}{3N} \langle u^2 \rangle^2 + \frac{3(\kappa' qv)^4 N}{35} \left[\frac{3 \operatorname{arccot} \epsilon'}{\epsilon'^5} + \frac{3 + 8\epsilon'^2 - 3\epsilon'^4}{\epsilon'^4 (1+\epsilon'^2)^3} \right]. \tag{3.46b}$$

When $\epsilon \to 0$,

$$\langle u^2 \rangle \simeq \frac{3\pi\kappa(qv)^2\Phi}{5\epsilon}, \tag{3.47a}$$

$$\langle u^4 \rangle \simeq \left(\frac{\kappa}{\epsilon}\right)^5 \frac{9\pi\kappa(qv)^4\Phi}{70}. \tag{3.47b}$$

These expressions are similar to those obtained for the co-oriented model with $n = 2$, see Eqs. (3.26). Eqs. (3.47) can be used to determine χ and λ, through Eqs. (3.37), for the tempered Lévy stable distribution given by Eq. (3.13).

3.4 The velocity autocorrelation function and its angular dependence

The similarity of Figs. 3.4 B and C suggests the angular structure of the velocity field is not that important to the instantaneous velocity probability distribution. But, as illustrated by Fig. 3.6, the velocity autocorrelation function $C(t)$ depends sensitively on the details of the velocity field. For both the co-oriented model, Eq. (3.4) with $n = 1$ or $n = 2$, and the dipolar model, Eq. (3.5), $C(t)$ can be determined analytically. In the thermodynamic limit, we find

$$C(t) \simeq \frac{3\pi^2(qv)^2\tau_\kappa\Phi}{4t} \tag{3.48}$$

for the co-oriented model and

$$C(t) \simeq \frac{3\pi\kappa(qv)^2\Phi}{5\epsilon} \begin{cases} 1 - 3(t/\tau_\epsilon)^2/7 & \text{if } t \leq \tau_\epsilon, \\ (\tau_\epsilon/t)^3[1 - 3(\tau_\epsilon/t)^2/7] & \text{if } t > \tau_\epsilon, \end{cases} \tag{3.49}$$

for the dipolar model. Here $\tau_\epsilon = 4\epsilon/(\pi v)$ and $\tau_\kappa = \kappa/v$. At long times, the approximations made to obtain Eqs. (3.48) and (3.49) become exact.

Eq. (3.49) predicts an asymptotic decay of t^{-3}, which is much faster than the asymptotic decay of t^{-1} in Eq. (3.48). This comes from the different angular structure of the respective velocity fields. In Fig. 3.6, the excellent agreement between the simulation data and the analytic expressions also confirms our numerical methods.

3.4.1 Co-oriented model

Starting from Eq. (3.8), the velocity autocorrelation function is

$$C(t) = N\left\langle \frac{(\kappa^n qv)^2}{(|\mathbf{r}+\mathbf{v}t|^n+\epsilon^n)(r^n+\epsilon^n)} \right\rangle = Nc(t), \tag{3.50}$$

where $c(t)$ is the velocity autocorrelation function in the presence of a single swimmer,

$$c(t) = \frac{3}{R^3}\left(\frac{\kappa^n qv}{4\pi}\right)^2 \int \frac{d^3r d^2\hat{n}}{(|r\hat{\mathbf{r}}+vt\hat{\mathbf{n}}|^n+\epsilon^n)(r^n+\epsilon^n)}. \tag{3.51}$$

Let $\epsilon' = \epsilon/R$, $\kappa' = \kappa/R$, $r' = r/R$, $s' = vt/R$, and $\gamma = \hat{\mathbf{r}}\cdot\hat{\mathbf{n}}$. By writing

$$|r\hat{\mathbf{r}}+vt\hat{\mathbf{n}}| = R(r'^2+2\gamma r's'+s'^2)^{1/2}, \tag{3.52}$$

we have

$$c(t) = 3\left(\frac{\kappa'^n qv}{4\pi}\right)^2 \int \frac{r'^2}{[(r'^2+2\gamma r's'+s'^2)^{n/2}+\epsilon'^n](r'^n+\epsilon'^n)}\, dr' d^2\hat{r} d^2\hat{n}. \tag{3.53}$$

Note, for any function $f(\gamma)$,

$$\int f(\gamma)\, d^2\hat{r} d^2\hat{n} = 8\pi^2 \int_{-1}^{1} f(\gamma)\, d\gamma. \tag{3.54}$$

Then

$$c(t) = \frac{3(\kappa'^n qv)^2}{2}\int_0^1 \frac{I(r',s')r'^2}{r'^n+\epsilon'^n}\, dr', \tag{3.55}$$

for which $I(r',s')$ encapsulates the integral

$$I(r',s') = \int_{-1}^{1} \frac{d\gamma}{(r'^2+2\gamma r's'+s'^2)^{n/2}+\epsilon'^n}. \tag{3.56}$$

We proceed further by specializing Eq. (3.55) for different n.

$n = 1$: Eq. (3.56) evaluates to

$$I(r',s') = \frac{r'+s'-|r'-s'|}{r's'} + \frac{\epsilon'}{r's'}\log\left(\frac{|r'-s'|+\epsilon'}{r'+s'+\epsilon'}\right). \tag{3.57}$$

Although the integral over r' in Eq. (3.55) can be calculated numerically, it can also be determined analytically in terms of the polylogarithm $\mathrm{Li}_\nu(z)$. This is defined as either a series,

$$\mathrm{Li}_\nu(z) = \sum_{m=1}^{\infty}\frac{z^m}{m^\nu} \qquad (|z|<1), \tag{3.58}$$

or an integral,

$$\mathrm{Li}_\nu(z) = \frac{z}{\Gamma(\nu)} \int_0^\infty \frac{\xi^{\nu-1}}{e^\xi - z}\, d\xi. \tag{3.59}$$

We find, denoting the real part of z by $\mathrm{Re}\, z$,

$$\begin{aligned} c(t) = -\frac{3(\kappa' q v)^2}{2s'} \mathrm{Re} \Bigg\{ & s'^2 + 2(\epsilon' - 1)s' \\ & + 2\epsilon'(1+\epsilon') \arctan\left(\frac{s'}{1+\epsilon'}\right) + \epsilon'^2 \log\left(\frac{\epsilon'}{s'+\epsilon'}\right)\left[4 + \log\left(\frac{s'}{s'+2\epsilon'}\right)\right] \\ & + \epsilon' s' \log\left(\frac{(1+\epsilon')^4 - (1+\epsilon')^2 s'^2}{(s'+\epsilon')^4}\right) + \epsilon'^2 \Bigg[\mathrm{Li}_2\left(\frac{s'+\epsilon'}{s'}\right) - \mathrm{Li}_2\left(\frac{1+\epsilon'}{s'}\right) \\ & - \mathrm{Li}_2\left(-\frac{\epsilon'}{s'}\right) + \mathrm{Li}_2\left(-\frac{1+\epsilon'}{s'}\right) + \mathrm{Li}_2\left(\frac{\epsilon'}{s'+2\epsilon'}\right) - \mathrm{Li}_2\left(\frac{s'+\epsilon'}{s'+2\epsilon'}\right)\Bigg] \Bigg\} \qquad (s' \le 1). \end{aligned} \tag{3.60}$$

In the thermodynamic limit, $C(t)$ is a constant,

$$\lim_{N\to\infty, R\to\infty} C(t) = 3(qv)^2 \Phi. \tag{3.61}$$

While interesting, this case is mostly irrelevant to active suspensions.

$n = 2$: Eq. (3.56) evaluates to

$$I(r', s') = \frac{1}{2r's'} \log\left(1 + \frac{4r's'}{(r'-s')^2 + \epsilon'^2}\right), \tag{3.62}$$

which further implies

$$\begin{aligned} c(t) = -\frac{3(\kappa'^2 q v)^2}{4s'} \mathrm{Re} \Bigg[& \frac{\log s'}{2} \log\left(1 + \frac{4s'}{(s'-1)^2 + \epsilon'^2}\right) \\ & + \log\left(\frac{s - 1 + i\epsilon'}{1 + s' + i\epsilon'}\right) \log\left(\frac{1+\epsilon'^2}{s' + 2i\epsilon'}\right) \\ & + \mathrm{Li}_2\left(\frac{s' - 1 - i\epsilon'}{s'}\right) - \mathrm{Li}_2\left(\frac{1 + s' - i\epsilon'}{s'}\right) \\ & + \mathrm{Li}_2\left(\frac{s' - 1 - i\epsilon'}{s' - 2i\epsilon'}\right) - \mathrm{Li}_2\left(\frac{s' + 1 - i\epsilon'}{s' - 2i\epsilon'}\right)\Bigg] \qquad (s' \le 1). \end{aligned} \tag{3.63}$$

Taking the thermodynamic limit[4], then expanding for a long time t, shows that $C(t)$

[4]Due to the potential singularness within integrals like Eq. (3.56), one must be careful about interchanging the limits and performing the integration. We avoid any problems by evaluating the integrals before taking the limits.

is a power-law,

$$\lim_{N\to\infty,R\to\infty} C(t) \simeq \frac{3\pi^2(qv)^2\tau_\kappa\Phi}{4t}. \tag{3.64}$$

More precisely, t is considered long when $t \gg \tau_\kappa$ for $\tau_\kappa = \kappa/v$.

3.4.2 Dipolar model

Again, from Eq. (3.8),

$$C(t) = N\left\langle \frac{(\kappa^2 qv)^2[3(\hat{\mathbf{r}}\cdot\hat{\mathbf{n}})^2-1]}{(|\mathbf{r}+vt\hat{\mathbf{n}}|+\epsilon^2)(r^2+\epsilon^2)}\left[3\left(\frac{r\hat{\mathbf{r}}\cdot\hat{\mathbf{n}}+vt}{|\mathbf{r}+vt\hat{\mathbf{n}}|}\right)^2-1\right]\right\rangle = Nc(t), \tag{3.65}$$

where

$$c(t) = (\kappa^2 qv)^2 \int \frac{3(\hat{\mathbf{r}}\cdot\hat{\mathbf{n}})^2-1}{(|\mathbf{r}+vt\hat{\mathbf{n}}|+\epsilon^2)(r^2+\epsilon^2)}\left[3\left(\frac{r\hat{\mathbf{r}}\cdot\hat{\mathbf{n}}+vt}{|\mathbf{r}+vt\hat{\mathbf{n}}|}\right)^2-1\right] d^3r d^2\hat{n}. \tag{3.66}$$

If $t = 0$, then we recover the second velocity moment $\langle u^2\rangle$, given in Eqs. (3.46), through $C(0) = \langle u^2\rangle$.

Keeping the notation used for the co-oriented model,

$$c(t) = \frac{3}{R^3}\left(\frac{\kappa^2 qv}{4\pi}\right)^2 \int \frac{(3\gamma^2-1)(r+\gamma vt)}{(r^2+\epsilon^2)[r^2+2\gamma rvt+(vt)^2]^{1/2}[r^2+2\gamma rvt+(vt)^2+\epsilon^2]} \times\left[\frac{3(\gamma r+vt)^2}{r^2+2\gamma rvt+(vt)^2}-1\right] d^3r d^2\hat{n}. \tag{3.67}$$

This is rewritten as

$$c(t) = \frac{3(\kappa'^2 qv)^2}{2}(I(t)-J(t)), \tag{3.68}$$

for which $I(t)$ and $J(t)$ enscapulate the double integrals

$$I(t) = 3\int_0^1\int_{-1}^1 \frac{(3\gamma^2-1)(r'+\gamma s')(\gamma r'+s')^2 r'^2}{(r'^2+\epsilon'^2)(r'^2+2\gamma r's'+s'^2)^{3/2}(r'^2+2\gamma r's'+s'^2+\epsilon'^2)}\, d\gamma dr' \tag{3.69}$$

and

$$J(t) = \int_0^1\int_{-1}^1 \frac{(3\gamma^2-1)(r'+\gamma s')r'^2}{(r'^2+\epsilon'^2)(r'^2+2\gamma r's'+s'^2)^{1/2}(r'^2+2\gamma r's'+s'^2+\epsilon'^2)}\, d\gamma dr'. \tag{3.70}$$

We perform the integrals over γ in Eqs. (3.69) and (3.70),

$$I(t) = \int_0^1 i(r',s')\, dr' \tag{3.71}$$

and

$$J(t) = \int_0^1 j(r', s')\, dr', \tag{3.72}$$

using the helpful definitions

$$\begin{aligned} i(r', s') = {} & \frac{3(3r'^4 + 2r'^2 s'^2 + 3s'^4)[(r' - s')|r' - s'|(r' + s')^3 - (r' + s')^2(r' - s')^3]}{32\epsilon'^2 r'^2 s'^5 (r'^2 + \epsilon'^2)} \\ & - \frac{3\epsilon'^2(s'^2 - 9r'^2 - 5\epsilon'^2)(r' + s' + |r' - s'|)}{80r's'^4(r'^2 + \epsilon'^2)} \\ & + \frac{3\epsilon'^2[18r'^4 - 32s'^4 + 5\epsilon'^2(8r'^2 + 3\epsilon'^2) + 2s'^2(19r'^2 + 5\epsilon'^2)](r' + s' + |r' - s'|)}{160r'^2 s'^5 (r'^2 + \epsilon'^2)} \\ & + \frac{(174r'^4 - 185r'^2 s'^2 - 201s'^4)[(r' + s')^2 - (r' - s')|r' - s'|]}{280r's'^5(r'^2 + \epsilon'^2)} \\ & + \frac{(174r'^4 - 185r'^2 s'^2 - 201s'^4)[(r' + s')^2 - (r' - s')|r' - s'|]}{280r's'^5(r'^2 + \epsilon'^2)} \\ & + \frac{3(r'^2 - s'^2 + \epsilon'^2)^2[3s'^6 - s'^4(r'^2 - 9\epsilon'^2) + 8\epsilon'^4 r'^2 + (r'^2 + \epsilon'^2)^2(s'^2 - 3r'^2 + 3\epsilon'^2)]}{32} \\ & \times \left[\arctan\left(\frac{r' + s'}{\epsilon'}\right) - \arctan\left(\frac{|r' - s'|}{\epsilon'}\right)\right] \end{aligned} \tag{3.73}$$

and

$$\begin{aligned} j(r', s') = {} & (r' + s' + |r' - s'|)\left[\frac{(r'^2 - 9s'^2 - 5\epsilon'^2)}{20r's'^2(r'^2 + \epsilon'^2)}\right. \\ & \left. + \frac{33s'^4 - 17r'^4 + 10\epsilon'^2 r'^2 + 15\epsilon'^2 + 8s'^2(r'^2 + 5\epsilon'^2)}{40r'^2 s'^3(r'^2 + \epsilon'^2)}\right] \\ & - \frac{(s'^2 - r'^2 + \epsilon'^2)[3s'^4 + 3(r'^2 + \epsilon'^2)^2 + 2s'^2(r'^2 + 3\epsilon'^2)]}{8\epsilon' r'^2 s'^3 (r'^2 + \epsilon'^2)} \\ & \times \left[\arctan\left(\frac{r' + s'}{\epsilon'}\right) - \arctan\left(\frac{|r' - s'|}{\epsilon'}\right)\right]. \end{aligned} \tag{3.74}$$

The remaining integrals of Eqs. (3.71) and (3.72) can be computed numerically or, in certain limits, analytically.

At a long time t, we obtain a tractable approximation by replacing ϵ' with 0 in the denominator of the integrands for $I(t)$ and $J(t)$. From this simplification,

$$C(t) \simeq \frac{24\kappa'(qv)^2\Phi}{70} \int_0^1 \left[\frac{7r'^2 - 9s'^2}{r'^4}\Theta(r' - s') + \frac{2r'(6r'^2 - 7s'^2)}{s'^5}\Theta(s' - r')\right] dr'. \tag{3.75}$$

The remaining integral over r' can be evaluated to determine the behavior of $C(t)$ at long times. Unfortunately, the corresponding expression diverges at short times

because we took $\epsilon' \to 0$. We avoid this divergence by introducing another cutoff l' as the lower limit of integration,

$$C(t) \simeq \frac{24\kappa'(qv)^2\Phi}{70}\int_{l'}^{1}\left[\frac{7r'^2-9s'^2}{r'^4}\Theta(r'-s')+\frac{2r'(6r'^2-7s'^2)}{s'^5}\Theta(s'-r')\right]dr', \quad (3.76)$$

which gives

$$C(t) \simeq \frac{12\kappa'(qv)^2\Phi}{5}\begin{cases} -1+1/l'+3s'^2/7-3s'^2/(7l'^3) & \text{if } l' \geq s', \\ -1-3l'^4/(7s'^5)+l'^2/s'^3+3s'^2/7 & \text{if } l' < s' < 1. \end{cases} \quad (3.77)$$

The value of l' is set by demanding $C(0) = \langle u^2 \rangle$, for which $\langle u^2 \rangle$ is taken from Eq. (3.46). We have

$$l' \simeq \frac{4\epsilon'}{\pi}. \quad (3.78)$$

At long times, Eq. (3.78) becomes exact, though it is also a useful approximation at intermediate times. Interestingly, the second piece of $C(t)$ from Eq. (3.77) implies that, for finite R, there is a certain time τ_{-1} after which $C(t)$ becomes negative. This can be estimated as the root of $C(t)$,

$$\tau_{-1} \simeq \frac{1}{v}\left[\left(\frac{4\epsilon}{\pi}\right)^2 R\right]^{1/3} \qquad (R \gg \epsilon). \quad (3.79)$$

Physically, this is caused by the structure of a dipolar velocity field. If a swimmer goes past a fixed point in the fluid, then the flow reverses direction (meaning the sign flips) after a certain time. But, as indicated by Eq. (3.79), this negative correlation is no longer accessible when $R \to \infty$ because $\tau_{-1} \propto R^{1/3}$. Taking the thermodynamic limit of Eq. (3.77) yields

$$C(t) \simeq \frac{3\pi\kappa(qv)^2\Phi}{5\epsilon}\begin{cases} 1-3(t/\tau_\epsilon)^2/7 & \text{if } t \leq \tau_\epsilon, \\ (\tau_\epsilon/t)^3[1-3(\tau_\epsilon/t)^2/7] & \text{if } t > \tau_\epsilon, \end{cases} \quad (3.80)$$

where $\tau_\epsilon = 4\epsilon/(\pi v)$. So the velocity autocorrelation function in a suspension of dipolar swimmers decays asymptotically like t^{-3}, which differs from the asymptotic decay of t^{-1} for the co-oriented model with $n = 2$, recall Eq. (3.64).

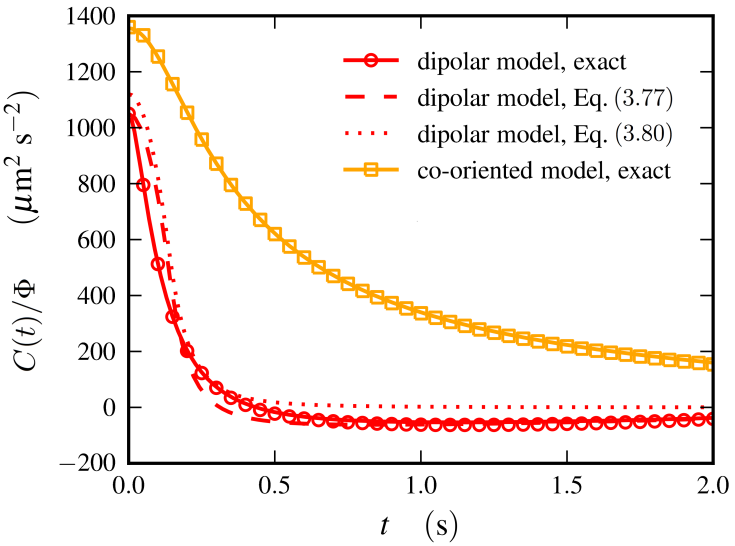

Fig. 3.6: Owing to the different field topologies, the velocity autocorrelation function $C(t)$ for the dipolar model of Eq. (3.5) decays faster than that for the co-oriented model of Eq. (3.4) with $n = 2$. Solid curves indicate the exact analytic solution and symbols correspond to simulation data. Dotted and dashed curves illustrate respectively the long time approximation and its behavior in the thermodynamic limit. Parameters are those of Fig. 3.4.

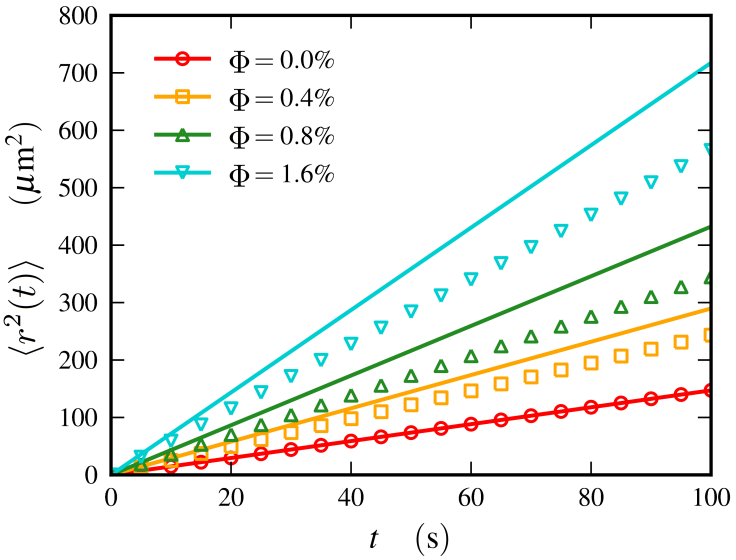

Fig. 3.7: Mean square displacement of a tracer at different volume fractions of swimmers. Solid lines are analytic upper bounds, $\langle r^2(t)\rangle = \langle \rho^2(t)\rangle + 6Dt$, and symbols display the ensemble-averaged measurements from simulations. Parameters are those of Fig. 3.4.

3.5 Mean square displacement

Having discussed the tracer velocities, we can analyze the tracer displacements. We focus on the more relevant case of dipolar swimmers and include Brownian motion. Something that can be directly measured in experiments is the mean square displacement of a tracer, $\langle r^2(t)\rangle$. We split $\langle r^2(t)\rangle$ into two parts, one from thermal effects, equal to $6Dt$, and one from swimmer flows, $\langle \rho^2(t)\rangle$. The velocity autocorrelation function $C(t)$ can be used to obtain an upper bound for contribution due to swimmers,

$$\begin{aligned}\langle \rho^2(t)\rangle &= \int_0^t \int_0^t \langle \mathbf{u}(\mathbf{r}(t'),t')\cdot\mathbf{u}(\mathbf{r}(t''),t'')\rangle\, dt'dt'' \\ &\leq \int_0^t \int_0^t \langle \mathbf{u}(0,t')\cdot\mathbf{u}(0,t'')\rangle\, dt'dt''. \end{aligned} \tag{3.81}$$

The above reflects the assumption that the spatial correlations are homogeneous and decay with distance, that is

$$\langle \mathbf{u}(\mathbf{r}',t')\cdot\mathbf{u}(\mathbf{r}'',t'')\rangle \leq \langle \mathbf{u}(\mathbf{r}',t')\cdot\mathbf{u}(\mathbf{r}',t'')\rangle = \langle \mathbf{u}(0,t')\cdot\mathbf{u}(0,t'')\rangle. \tag{3.82}$$

Inserting Eq. (3.49) into Eq. (3.81) yields

$$\begin{aligned}\langle \rho^2(t)\rangle &\leq \int_0^t \int_0^t C(|t'-t''|)\, dt'dt'' \\ &\simeq 6\kappa q^2 v\Phi t \begin{cases} (t/\tau_\epsilon)[2/5-(t/\tau_\epsilon)^2/35] & \text{if } t<\tau_\epsilon, \\ 1+(\tau_\epsilon/t)[-1+2(\tau_\epsilon/t)/5-(\tau_\epsilon/t)^3/35] & \text{if } t\geq\tau_\epsilon. \end{cases}\end{aligned} \tag{3.83}$$

This implies a tracer diffusing in the presence of dipolar swimmers has a ballistic mean square displacement at short times, $t \ll \tau_\epsilon$, and a normal mean square displacement at long times, $t \gg \tau_\epsilon$. We compare Eq. (3.83) to simulation data in Fig. 3.7. The linear growth $\langle r^2(t)\rangle \propto t$ agrees with the experimental results of Ref. [73].

3.6 Evolution of the position probability distribution

The motion of a tracer in a fluctuating field $\mathbf{u}(\mathbf{r}, t)$ is captured by the position probability distribution,

$$P(\mathbf{r}, t) = \langle \delta(\mathbf{r} - \mathbf{r}(t)) \rangle. \tag{3.84}$$

For a Gaussian field, which is uniquely defined from the two-point correlation function $\langle \mathbf{u}(\mathbf{r}, t)\mathbf{u}(\mathbf{r}', t') \rangle$, it is possible to model $P(\mathbf{r}, t)$ analytically [66]. We saw as much in Chapter 2. But, we demonstrated that fluctuations in an active suspension are neither Gaussian nor uncorrelated. They are much closer to a Lévy stable process.

Generally, the hierarchy of correlations in Lévy stable random fields is poorly understood [94]. It is therefore unclear how to adapt successful models of random advection by a Gaussian field [95] or, more broadly, extend the understanding of colored Gaussian noise [66] to colored Lévy stable processes. These challenges make it very difficult to construct an effective model that bridges the dynamics in $P(\mathbf{r}, t)$ on all of the time scales. Partial theoretical insight can be gained, however, by considering the asymptotic behavior for short and long times. Here we expect $P(\mathbf{r}, t)$ to depend only on r and t.

At short times, $t \ll \tau_\epsilon$, $P(r, t)$, combines ballistic transport from constant swimmer advection and diffusive spreading from thermal Brownian effects. With parameters similar to those of Ref. [73], normal diffusion is much stronger than advection and, at these times, $P(r, t)$ is captured by the normal diffusion equation. If Brownian motion is neglected, then we rescale as $P(r, t) = W(r/t)/t^3$, where $W(r/t)$ is the tempered Lévy stable distribution taken directly from Eq. (3.13). The rescaling comes from averaging over constant, but random, advection by swimmers. This probability distribution compares well against the simulation data, given $D = 0$, at short times. See the insets of Fig. 3.8.

For long times, $t \gg \tau_\epsilon$, after the correlations of the velocity field have vanished

(typically several seconds), we may interpret a tracer diffusing in an active suspension as a realization of an uncorrelated tempered Lévy stable process. Effectively, this corresponds to replacing $\mathbf{u}(\mathbf{r},t)$ from Eq. (3.1) with an uncorrelated, but non-Guassian, random function $\boldsymbol{v}(t)$. In order to describe the swimmer-induced noise $\boldsymbol{v}(t)$, we must supply a characteristic functional $\mathcal{F}[\mathbf{k}(\cdot);t]$. The tempered Lévy stable distribution used for the velocity probability distribution, Eq. (3.13), suggests

$$\mathcal{F}[\mathbf{k}(\cdot);t] = \exp\left[- D_\alpha \int_0^t (k(t')^2 + \Lambda^2)^{\alpha/2}\, dt' + D_\alpha \Lambda^\alpha t \right] \tag{3.85}$$

as an approximation at long times. Here D_α is an anomalous diffusion coefficient of dimensions $\mathrm{m}^\alpha\ s^{-1}$ and Λ is a reguarization coefficient of dimensions m^{-1}. For $\alpha = 2$, $\boldsymbol{v}(t)$ reduces to uncorrelated Gaussian noise. As $\Lambda \to 0$, $\mathcal{F}[\mathbf{k}(\cdot);t]$ becomes exactly the characteristic functional for Lévy stable noise, Eq. (2.33) of Chapter 2. This is the same as taking $\epsilon \to 0$.

The Fokker-Planck equation that corresponds to $\mathcal{F}[\mathbf{k}(\cdot);t]$ is [96]

$$\frac{\partial}{\partial t} P(r,t) = D_\alpha[\Lambda^\alpha - (\Lambda^2 - \nabla^2)^{\alpha/2}]P(r,t) + D\nabla^2 P(r,t), \tag{3.86}$$

where we also included a term for normal diffusion. In Fourier space, the solution of Eq. (3.86) reads

$$P(k,t) = e^{D_\alpha[\Lambda^\alpha - (k^2+\Lambda^2)^{\alpha/2}]t - Dk^2 t}. \tag{3.87}$$

Using a Levenberg-Marquardt algorithm that numerically inverts the Fourier transform, we fit the coefficients D_α and Λ to the data from our simulations. Eq. (3.86) compares well against the long time data in Figs. 3.8 and 3.9. It is worth emphasizing that, although the motion of tracers at long times is non-Gaussian and described by a fractional diffusion equation, the asymptotic mean square displacement is normal, $\langle r^2(t)\rangle \propto t$.

At intermediate times, when the velocity autocorrelation function is already decaying, but still not negligible due to the t^{-3} scaling, the transient behavior of the

position probability distribution can be interpreted as a superposition of two distinct effects: ballistic tracer displacements, remaining from the dynamics at short times, and fractional diffusive behavior, owing to the onset of scattering by multiple swimmers. A qualitative comparision suggests the measurements of tracer diffusion in Ref. [73], which focused on the range $t \simeq 1$ s, are exploring this intermediate regime.

3.7 Discussion

How microorganisms stir and mix a fluid is important for deciphering the evolution from unicellular to multicellular life [97, 98]. As the transport of nutrients is often diffusion-limited, a suspension of swimmers may induce an anomalous (not Brownian) uptake.

We developed a theoretical model of tracer diffusion in dilute swimmer suspensions. Analytically and numerically, using simulations on GPUs, we showed that different statistics can be expected depending on the asymptotic decay of the velocity field. For velocity fields that scale as r^{-1} due to the presence of an external force, the fluctuations are Gaussian even at small volume fractions. This agrees with the central limit theorem. But, velocity fields that decay as r^{-2} or faster will exhibit signatures of a Lévy stable process. Very recent measurements appear to confirm this prediction [86]. When the statistics are non-Gaussian, our results suggest the convergence properties are similar to those of truncated Lévy flights [93]. Though we prepared data for swimmers that are "pullers" ($q < 0$), these statements are also true for "pushers" ($q > 0$) as long as the suspension remains statistically homogeneous and isotropic.

Thinking about experimental measurements, it is important to note that a tracer velocity is well-defined only if thermal effects are negligible, which corresponds to $D = 0$. Otherwise, displacements over a time interval Δt contain a factor that scales as $(\Delta t)^{1/2}$. This must be taken into account to reconstruct velocity distributions from

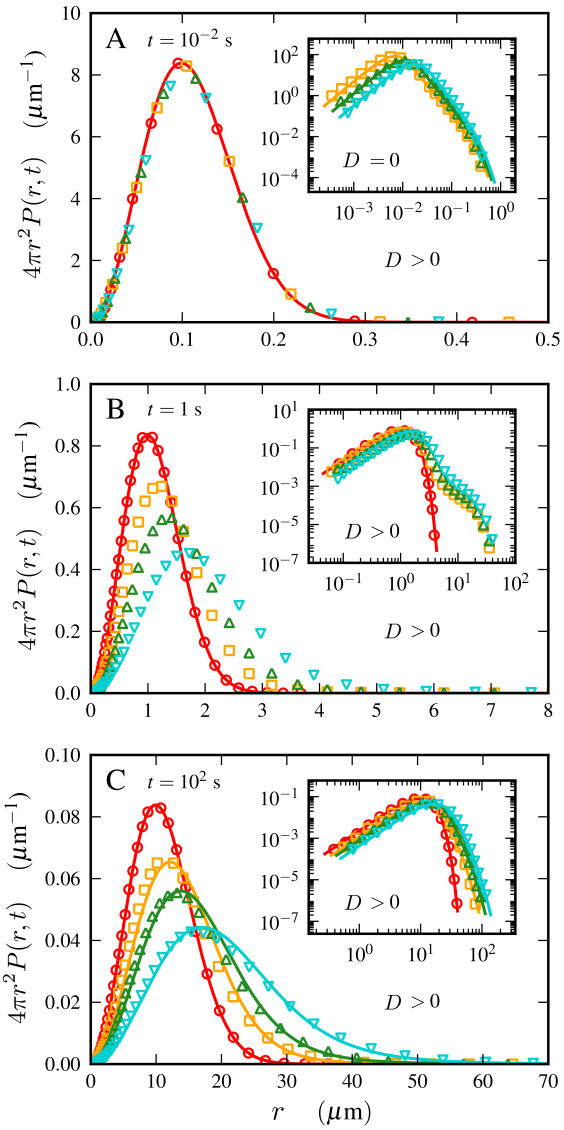

Fig. 3.8: Radial position probability distribution of a tracer in a dilute suspension of dipolar swimmers at various times. Solid curves represent analytic forms of $P(r,t)$ and symbols illustrate histograms determined from simulations. Insets B and C show the same quantities on a log-log scale. Volume fractions and symbols are those of Fig. 3.7. Parameters are those of Fig. 3.4 with $D = 0.245$ μm^2 s^{-1}. (A) Short time regime. At these times, Brownian motion effectively dominates constant advection for our choice of parameters. In the limit of no thermal noise (inset), the position probability distribution is the tempered Lévy stable velocity probability distribution, $W(u)$, after a rescaling with t. (B) Transient behavior. This period corresponds to an intermediate decay of the velocity autocorrelation function. (C) Asymptotic long time regime. Eventually, random advection from many low Reynolds number swimmers becomes equivalent to a tempered Lévy flight. The solution to the fractional diffusion equation, that is Eq. (3.86), is matched against simulations by fitting its coefficients D_α and Λ, see also Fig. 3.9.

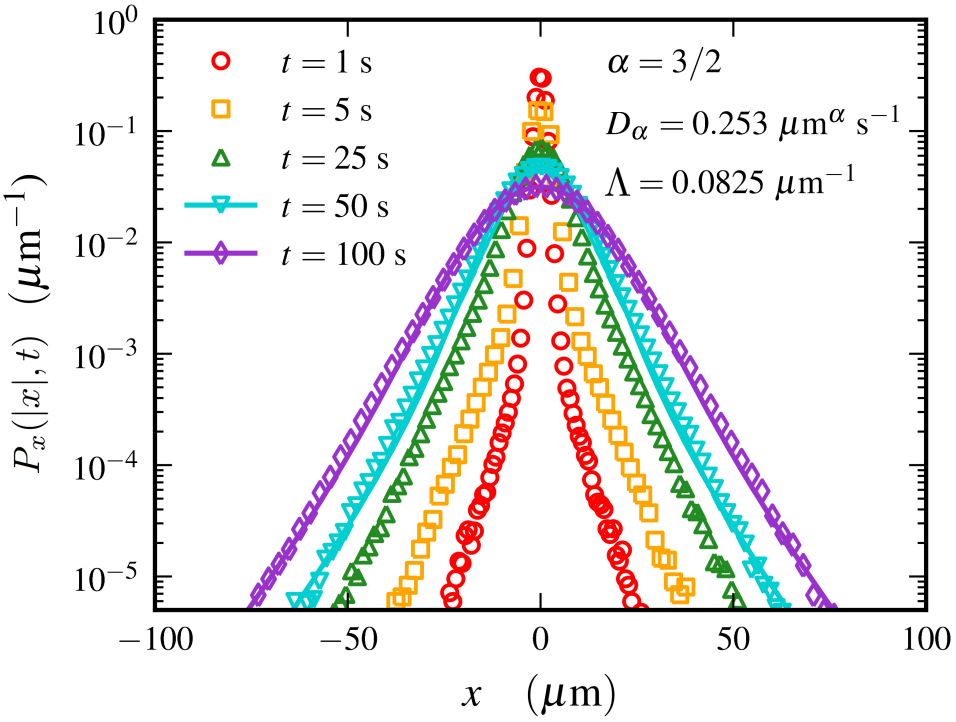

Fig. 3.9: Time evolution of the marginal position probability distribution at a volume fraction $\Phi = 1.6\%$. Solid curves represent Eq. (3.86) with fitted coefficients, shown only at long times, and symbols illustrate histograms determined from simulations. Parameters are those of Fig. 3.4 with $D = 0.245\ \mu\mathrm{m}^2\ \mathrm{s}^{-1}$. At intermediate times, say $t \simeq 1$ s, our data resemble the measurements from Ref. [73].

discretized trajectories as the measured probability distributions can vary depending on the choice of discretization interval.

Our analysis further illustrates that the angular shape of the velocity field is not important to the velocity probability distribution, which is dominated by the radial flow structure. The temporal decay of the velocity correlations, however, depend sensitively on the angular topology of the individual swimmer flow fields. Specifically, our analytic calculations predict that velocity autocorrelations in a dipolar swimmer suspension vanish algebraically as t^{-3}. This prediction could be tested experimentally by monitoring the flow field at a fixed point in the fluid, using a setup similar to that described in Ref. [86].

Finally, we propose that the tracer dynamics at long times can be approximated by a tempered fractional diffusion equation. If the swimmers also undergo directional changes (due to stimuli response or thermal fluctuations), then the net result will only be a further decorrelation of the velocity fluctuations, assuming the suspension remains homogeneous and isotropic. In this case, the tempered Lévy probability distribution from Eq. (3.86) should become valid at earlier times. It would be interesting if the fractional evolution of the position probability distribution at long times could be confirmed experimentally. This, however, will require observation times that go substantially beyond those considered in Ref. [73].

A complete interpretation of the experimental data requires extending Brownian motion beyond the available theories [66, 71, 72]. Though many challenging problems remain – namely, the consistent formulation of a more general Fokker-Planck equation that combines Lévy-like flights and time correlations – our results are a step towards a better understanding of present and future experiments.

Chapter 4

Near-Exponential Distributions from Truncated Power-Law Fields

4.1 Less activity, please

One of the deepest questions in probability concerns how a sum of N random variables is distributed. Asymptotically, as $N \to \infty$, we know from Chapter 2 there are two possible answers. The first, given by the central limit theorem [62], states the probability distribution of such a sum must converge to a Gaussian distribution if each random variable has a finite variance. The second, due to the generalized central limit theorem [62, 64], claims the probability distribution of that sum instead becomes a Lévy stable distribution if each random variable has an infinite variance. Quite often, the central limit theorem holds even for $N \approx 10$, which has made it extremely helpful in statistical physics. Although stochastic processes that have an infinite variance are unusual, they can occur. For example, the generalized central limit theorem has found a niche in continuous random walks as the fundamental ingredient of fractional diffusion equations and, more specifically, Lévy flights [67, 68, 71, 72].

In Chapter 3, we saw that these limit theorems are not just concepts from probability, but also have consequences for physics. While studying how a tracer diffuses in a dilute suspension of swimming microorganisms, we found a bridge between the central limit theorem and the generalized central limit theorem. The tempered Lévy

stable distribution that we proposed as a model is sensibly motivated and reasonably accurate, at least as an initial approximation. Nevertheless, it remains phenomenological. Can we generally derive the probability distribution for the instantaneous fluctuations? Apart from active suspensions, such a derivation may apply to other non-equilibrium systems.

So, forget all about activity and think only about statistical physics. In d dimensions, consider the power-law field

$$\mathbf{u}(\mathbf{r}) = \frac{\lambda \boldsymbol{\Omega}(\hat{\mathbf{r}})}{r^n} \tag{4.1}$$

for some positive integer n. The prefactor λ is a constant having the dimensions of $\mathbf{u}(\mathbf{r})$ multiplied by length^n. We take $\boldsymbol{\Omega}(\hat{\mathbf{r}})$ to be a dimensionless vector function that encapsulates the angular dependence of $\mathbf{u}(\mathbf{r})$, though it could hide lots of variables. As special cases, Eq. (4.1) includes the force determined from a power-law potential, many Green's functions common to physics (like a point force in a viscous fluid or an elastic solid), and the leading-order term of any multipole expansion.

Let $\mathbf{u}(\mathbf{r})$ originate from a discrete element, called a source, that is uniformly distributed in a hyperspherical volume $V = 2\pi^{d/2}R^d/(d\Gamma(d/2))$ with radius R. Now $\boldsymbol{\Omega}$ (through $\hat{\mathbf{r}}$) and r are random variables, meaning $\mathbf{u}$ is completely described by its probability distribution. We measure this random process using a test particle, called a tracer, that passively takes up the field in which it is placed. Given a population of N sources, the tracer experiences a net field equal to the sum over all fields. What is the probability distribution of the net field?

The question we are asking generalizes our approach to the velocity fluctuations of Chapter 3. An answer will be important to understanding each phenomenon involving a sum over many power-law fields. It seems active suspensions are only the tip of an iceberg, there are a large number of physical systems that may be interpreted as power-law fields distributed appropriately [99, 100, 101, 102, 103, 104]. All of these

have fluctuations deviating from Gaussian due to tails that vanish much more slowly. For certain n, we should expect this, as the variance of $\mathbf{u}$ can diverge,

$$\langle u^2 \rangle = \frac{d\lambda^2 \langle \Omega^2 \rangle}{R^d} \int_0^R r^{d-(2n+1)} dr = \begin{cases} d\lambda^2 \langle \Omega^2 \rangle / [(d-2n) R^{2n}] & \text{if } n < d/2, \\ \infty & \text{otherwise.} \end{cases} \tag{4.2}$$

The divergence of $\langle u^2 \rangle$ has been used to argue for power-law tails, like we did in Chapter 3, reflecting either a Lévy stable distribution or an attraction to that family.

An early prediction of non-Gaussian fluctuations came from Johan Holtsmark, for the probability distribution of the electric field due to charged particles in a stationary plasma [99]. The Holtsmark distribution, a symmetric Lévy stable distribution with characteristic exponent $\alpha = 3/2$, was later derived for other Coulomb-like interactions, notably the gravitational force acting on a star in a stellar cluster [100]. Some aspects of turbulence may be described as the creation and destruction of vorticity, an idea from Lars Onsager [105]. Using point vortices in two or three dimensions, Lévy stable distributions have repeatedly been calculated for the velocity and velocity difference of a flow [101, 102, 103]. In a spin glass, the interaction between nearby sites can decay as r^{-3}, perhaps suggesting a Cauchy distibution of couplings [104].

Except for the simulations of Refs. [102] and [103], none of these examples had a cutoff in $\mathbf{u}(\mathbf{r})$ during the analytical or numerical calculations. In that case, it is not surprising to find a Lévy stable distribution because the generalized central limit theorem demands it. However, any physical model of fluctuations corresponding to a sum of power-law random variables always needs a cutoff. This is what changes the limit distribution from a Lévy stable distribution to a Gaussian distribution, though convergence might be extremely slow [93]. The aim of this chapter is to provide an exact analytical result applicable to various systems.

Starting with Eq. (4.1), we determine the probability distribution $p(\mathbf{u})$ of the contribution from a single source. We choose the cutoff as the tracer radius a. Assuming statistical isotropy, so there is only dependence on u, a simple condition is given for

$p(u)$ to be mostly a truncated power-law distribution. We then calculate the probability distribution $P(u)$ in the thermodynamic limit, where the concentration of sources is held at $\Phi = N/V$ as $N \to \infty$ and $R \to \infty$. This is done specifically for $p(u)$ whose variance diverges if $a \to 0$, but a is arbitrary throughout. Appropriately, we recover either a Gaussian distribution as Φ becomes large or a Lévy stable distribution as $a \to 0$. Besides $P(u)$, which is exact, we give another probability distribution $\widetilde{P}(u)$ that approximates $P(u)$ by some effective cutoffs in u rather than the actual cutoffs in r.

Our expressions, for the first time, have cutoffs in the thermodynamic limit. As such, they are correct at any Φ. More generally, we predict tails that are very near to exponentials, appearing only if a is nonzero. The tails are universal to power-law fields that are short-ranged, in the sense they appear so long as $n > d/2$.

4.2 Statistics of a single source

We first consider the field $\mathbf{u}(\mathbf{r})$ due to just a single source, a fixed source concentration Φ is done much later. Without loss of generality, we place a tracer at the origin. The source is uniformly distributed throughout V, except in the space occupied by the tracer. So the volume available to the source is actually $2\pi^{d/2}(R^d - a^d)/(d\Gamma(d/2))$, which introduces the cutoff a. Alternatively, we could set $\mathbf{u}(\mathbf{r}) = 0$ if $r < a$. These different approaches are not identical, but are approximately the same for $a \ll R$.

Formally, using angled brackets to indicate an average over $\mathbf{\Omega}$ and r, the probability distribution is

$$p(\mathbf{u}) = \frac{1}{u^{d-1}\sin^{d-2}u_{\phi_1}\sin^{d-3}u_{\phi_2}\cdots\sin u_{\phi_{d-2}}}\left\langle \delta\left(u - \frac{|\lambda|\Omega}{r^n}\right) \times \delta(u_\theta - \Omega_\theta)\delta(u_{\phi_1} - \Omega_{\phi_1})\delta(u_{\phi_2} - \Omega_{\phi_2})\cdots\delta(u_{\phi_{d-2}} - \Omega_{\phi_{d-2}})\right\rangle. \tag{4.3}$$

The vectors $\mathbf{u}$ and $\mathbf{\Omega}$ are written in hyperspherical coordinates, like those from Appendix B. We write the probability distribution for $\mathbf{\Omega}$ as $f(\mathbf{\Omega})$.

In Eq. (4.3), we immediately perform the average over r. Changing variables to $\xi = |\lambda|\Omega/r^n$ gives

$$\begin{aligned}\frac{d}{(R^d - a^d)u^{d-1}} \int_a^R \delta\left(u - \frac{|\lambda|\Omega}{r^n}\right) r^{d-1}\, dr &= \frac{\alpha(|\lambda|\Omega)^\alpha}{(R^d - a^d)u^{d-1}} \int_{|\lambda|\Omega/R^n}^{|\lambda|\Omega/a^n} \frac{\delta(u-\xi)}{\xi^{1+\alpha}}\, d\xi \\ &= \frac{\alpha(|\lambda|\Omega)^\alpha}{(R^d - a^d)u^{d+\alpha}} \Theta\left(u - \frac{|\lambda|\Omega}{R^n}\right)\Theta\left(\frac{|\lambda|\Omega}{a^n} - u\right), \end{aligned} \tag{4.4}$$

where $\Theta(x)$ is the Heaviside theta function. The characteristic exponent $\alpha = d/n$ arises naturally during the integration. Next, we average over the angular coordinates Ω_θ and $\Omega_{\phi_1}, \Omega_{\phi_2}, \ldots, \Omega_{\phi_{d-2}}$,

$$\begin{aligned}&\int f(\mathbf{\Omega})\delta(u_\theta - \Omega_\theta)\delta(u_{\phi_1} - \Omega_{\phi_1})\delta(u_{\phi_2} - \Omega_{\phi_2}) \cdots \delta(u_{\phi_{d-2}} - \Omega_{\phi_{d-2}}) \\ &\qquad \times \sin^{d-2}\Omega_{\phi_1} \sin^{d-3}\Omega_{\phi_2} \cdots \sin\Omega_{\phi_{d-2}}\, d\Omega_\theta d\Omega_{\phi_1} d\Omega_{\phi_2} \cdots d\Omega_{\phi_{d-2}} \\ &\quad = f(\Omega\hat{\mathbf{u}}) \sin^{d-2} u_{\phi_1} \sin^{d-3} u_{\phi_2} \cdots \sin u_{\phi_{d-2}}. \end{aligned} \tag{4.5}$$

Putting Eqs. (4.4) and (4.5) together with the average over Ω,

$$p(\mathbf{u}) = \frac{\alpha|\lambda|^\alpha}{(R^d - a^d)u^{d+\alpha}} \int_0^\infty f(\Omega\hat{\mathbf{u}})\Omega^{d+\alpha-1}\Theta\left(u - \frac{|\lambda|\Omega}{R^n}\right)\Theta\left(\frac{|\lambda|\Omega}{a^n} - u\right) d\Omega. \tag{4.6}$$

Given some $\mathbf{u}$, the Heaviside theta functions constrain the integral to Ω with $a^n u/|\lambda| \leq \Omega \leq R^n u/|\lambda|$. This, in principle, couples the angular dependence to both cutoffs, possibly affecting how $p(\mathbf{u})$ decays. If we instead chose $\mathbf{u}(\mathbf{r}) = 0$ for $r < a$, then Eq. (4.6) would be

$$\begin{aligned}p(\mathbf{u}) = &\left(\frac{a}{R}\right)^d \delta(\mathbf{u}) \\ &+ \frac{\alpha|\lambda|^\alpha}{R^d u^{d+\alpha}} \int_0^\infty f(\Omega\hat{\mathbf{u}})\Omega^{d+\alpha-1}\Theta\left(u - \frac{|\lambda|\Omega}{R^n}\right)\Theta\left(\frac{|\lambda|\Omega}{a^n} - u\right) d\Omega. \end{aligned} \tag{4.7}$$

Except at $\mathbf{u} = 0$, Eqs. (4.6) and (4.7) are the same for $a \ll R$.

From here on out, it is assumed that $\mathbf{u}$ is an isotropic random vector. This means $\langle\mathbf{\Omega}\rangle = 0$ and $f(\mathbf{\Omega})$ depends only on Ω. We work with the radial distribution $g(\Omega)$, defined by

$$f(\Omega) = \Gamma\left(\frac{d}{2}\right)\frac{g(\Omega)}{2\pi^{d/2}\Omega^{d-1}}. \tag{4.8}$$

Eq. (4.6) becomes

$$p(u) = \Gamma\left(\frac{d}{2}\right) \frac{\alpha|\lambda|^\alpha}{2\pi^{d/2}(R^d - a^d)u^{d+\alpha}} \int_0^\infty g(\Omega)\Omega^\alpha \Theta\left(u - \frac{|\lambda|\Omega}{R^n}\right)\Theta\left(\frac{|\lambda|\Omega}{a^n} - u\right) d\Omega. \quad (4.9)$$

Under rather general conditions, there is actually a power-law obscured by the integral. Suppose Ω is bounded, $\Omega_{\min} \le \Omega \le \Omega_{\max}$, for which $\Omega_{\min}$ is nonzero and $\Omega_{\max}$ is finite. Everywhere else, $\Omega < \Omega_{\min}$ or $\Omega > \Omega_{\max}$, $g(\Omega)$ vanishes. If u lies between $|\lambda|\Omega_{\max}/R^n$ and $|\lambda|\Omega_{\min}/a^n$, then the Heaviside theta functions in Eq. (4.9) are made redundant. We have

$$p(u) = \Gamma\left(\frac{d}{2}\right) \frac{\alpha|\lambda|^\alpha \langle\Omega^\alpha\rangle}{2\pi^{d/2}(R^d - a^d)u^{d+\alpha}} \qquad \left(\frac{|\lambda|\Omega_{\max}}{R^n} \le u \le \frac{|\lambda|\Omega_{\min}}{a^n}\right), \quad (4.10)$$

where $\langle\Omega^\alpha\rangle = \int f(\Omega)\Omega^\alpha \, d^d\Omega = \int_0^\infty g(\Omega)\Omega^\alpha \, d\Omega$ is a fractional moment of order α. So, for this piece of $p(u)$, the angular dependence of $\mathbf{u}(\mathbf{r})$ is completely swept into $\langle\Omega^\alpha\rangle$. The probability contributed from Eq. (4.10) is

$$\begin{aligned} 2\pi^{d/2}\Gamma\left(\frac{d}{2}\right)^{-1} \int_{|\lambda|\Omega_{\min}/R^n}^{|\lambda|\Omega_{\min}/a^n} p(u)u^{d-1}\, du &= \frac{\alpha|\lambda|^\alpha\langle\Omega^\alpha\rangle}{R^d - a^d} \int_{|\lambda|\Omega_{\max}/R^n}^{|\lambda|\Omega_{\min}/a^n} u^{-(1+\alpha)}\, du \\ = \frac{\langle\Omega^\alpha\rangle[(\Omega_{\min}/\Omega_{\max})^\alpha - (a/R)^d]}{\Omega_{\min}^\alpha[1-(a/R)^d]} &\simeq \frac{\langle\Omega^\alpha\rangle}{\Omega_{\max}^\alpha}. \end{aligned} \quad (4.11)$$

Above we took $(a/R)^d \ll (\Omega_{\min}/\Omega_{\max})^\alpha$, increasingly valid as R becomes large. When $\langle\Omega^\alpha\rangle/\Omega_{\max}^\alpha \simeq 1$, the asymptotic decay of $\mathbf{u}(\mathbf{r})$ contributes more than the exact details of $\mathbf{\Omega}(\hat{\mathbf{r}})$. No matter what, $p(u)$ has cutoffs at the extreme values $u_{\min} = |\lambda|\Omega_{\min}/R^n$ and $u_{\max} = |\lambda|\Omega_{\max}/a^n$.

Without evaluating the integral from Eq. (4.9), we can still calculate the moments of $\mathbf{u}$ by directly averaging Eq. (4.1). Its odd moments are zero. Its even moments are symmetric tensors, each of which has a radial part

$$\begin{aligned} \langle u^{2m}\rangle &= \frac{d}{R^d - a^d} \int_a^R \int_0^\infty g(\Omega)\left(\frac{\lambda\Omega}{r^n}\right)^{2m} r^{d-1}\, d\Omega dr \\ &= \frac{d\lambda^{2m}\langle\Omega^{2m}\rangle}{R^d - a^d} \int_a^R r^{d-(1+2mn)}\, dr \\ &= \frac{d\lambda^{2m}\langle\Omega^{2m}\rangle[(a/R)^d - (a/R)^{2mn}]}{(2mn-d)a^{2mn}[1-(a/R)^d]}. \end{aligned} \quad (4.12)$$

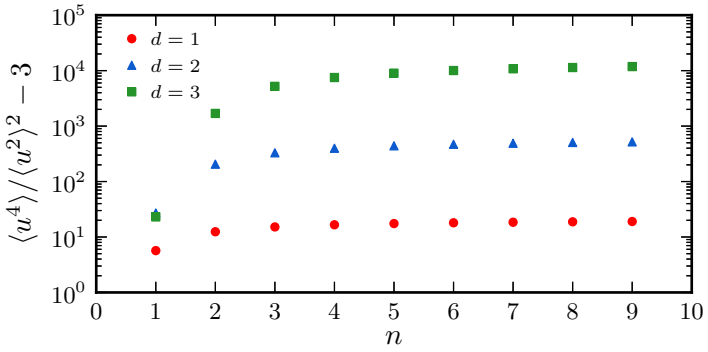

Fig. 4.1: The kurtosis $\langle u^4\rangle/\langle u^2\rangle^2 - 3$ for various d. We took $\Omega(\hat{\mathbf{r}}) = 1$, $a = 1$, and $R = 25$. If $d = 1$, then nothing really happens. For $d = 2$ and $d = 3$, there is a sharp change from $n = 1$ to $n = 2$. After $a \to 0$, this transition becomes an infinite jump at $n = d/2$.

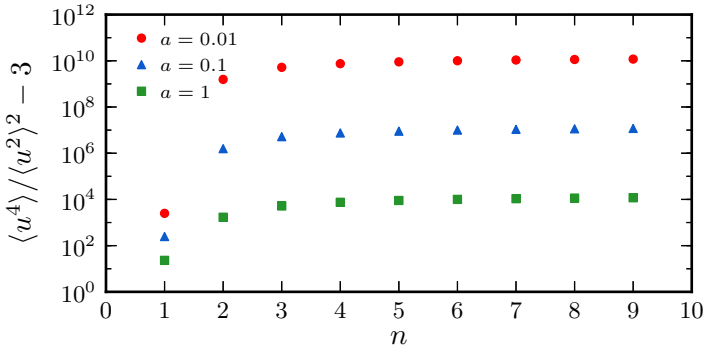

Fig. 4.2: The kurtosis $\langle u^4\rangle/\langle u^2\rangle^2 - 3$ with $d = 3$ for various a. All of the other parameters are the same as those of Fig. 4.1. A decrease in a by a single order of magnitude causes an increase in $\langle u^4\rangle/\langle u^2\rangle^2 - 3$ by a few orders of magnitude.

The kurtosis follows easily,

$$\frac{\langle u^4\rangle}{\langle u^2\rangle^2} - 3 = \frac{(2n-d)^2\langle\Omega^4\rangle[1-(a/R)^d][(a/R)^d-(a/R)^{4n}]}{d(4n-d)\langle\Omega^2\rangle^2[(a/R)^d-(a/R)^{2n}]^2} - 3. \tag{4.13}$$

How Eq. (4.13) behaves depends on both d and n. We find, again taking $a \ll R$,

$$\frac{\langle u^4\rangle}{\langle u^2\rangle^2} - 3 \simeq \frac{\langle\Omega^4\rangle}{\langle\Omega^2\rangle^2} \begin{cases} (2n-d)^2/[d(4n-d)] - 3 & \text{if } n < d/2, \\ 1/[d^2(a/R)^d \log^2(a/R)] - 3 & \text{if } n = d/2, \\ (2n-d)^2/[d(4n-d)(a/R)^d] - 3 & \text{if } n > d/2. \end{cases} \tag{4.14}$$

For $n \geq d/2$ or, equivalently, $\alpha \leq 2$, $\langle u^4\rangle/\langle u^2\rangle^2 - 3$ grows as a shrinks. This is what Eq. (4.2) implies. We show $\langle u^4\rangle/\langle u^2\rangle^2 - 3$ in Figs. 4.1 and 4.2. Note the large transition from $n = 1$ to $n = 2$ with $d = 3$.

Finally, we determine the marginal probability distribution $p_x(|u_x|)$ along, say, the x-axis by integrating $p(u)$ with respect to the other variables. We do this for two reasons. First, it is not immediately clear what the marginal probability distribution of a truncated power-law distribution is. Second, it is helpful later as a special case of something that is much more complicated.

Set $u_\rho = (u^2 - u_x^2)^{1/2}$. Then

$$\begin{aligned} p_x(|u_x|) &= 2\pi^{(d-1)/2}\Gamma\left(\frac{d-1}{2}\right)^{-1} \int_0^\infty p\big((u_x^2+u_\rho^2)^{1/2}\big) u_\rho^{d-2}\, du_\rho \\ &= \Gamma\left(\frac{d}{2}\right)\Gamma\left(\frac{d-1}{2}\right)^{-1} \frac{\alpha|\lambda|^\alpha}{\pi^{1/2}(R^d-a^d)} \int_0^\infty \int_0^\infty \frac{g(\Omega)\Omega^\alpha u_\rho^{d-2}}{(u_x^2+u_\rho^2)^{(d+\alpha)/2}} \\ &\quad \times \Theta\left((u_x^2+u_\rho^2)^{1/2} - \frac{|\lambda|\Omega}{R^n}\right)\Theta\left(\frac{|\lambda|\Omega}{a^n} - (u_x^2+u_\rho^2)^{1/2}\right) d\Omega du_\rho. \end{aligned} \tag{4.15}$$

After interchanging the order of integration, the conditions enforced with the Heaviside theta functions can be written as $[(\lambda\Omega/R^n)^2 - u_x^2]^{1/2} < u_\rho < [(\lambda\Omega/a^n)^2 - u_x^2]^{1/2}$. So, for $|u_x| < |\lambda|\Omega/R^n$,

$$\begin{aligned} \int_{[(\lambda\Omega/R^n)^2-u_x^2]^{1/2}}^{[(\lambda\Omega/a^n)^2-u_x^2]^{1/2}} \frac{u_\rho^{d-2}}{(u_x^2+u_\rho^2)^{(d+\alpha)/2}}\, du_\rho &= \frac{1}{(d-1)|u_x|^{d+\alpha}} \Bigg\{ \left[\left(\frac{\lambda\Omega}{a^n}\right)^2 - u_x^2\right]^{(d-1)/2} \\ &\quad \times {}_2F_1\left(\frac{d-1}{2}, \frac{d+\alpha}{2}; \frac{1+d}{2}; 1 - \left(\frac{\lambda\Omega}{a^n u_x}\right)^2\right) - \left[\left(\frac{\lambda\Omega}{R^n}\right)^2 - u_x^2\right]^{(d-1)/2} \\ &\quad \times {}_2F_1\left(\frac{d-1}{2}, \frac{d+\alpha}{2}; \frac{1+d}{2}; 1 - \left(\frac{\lambda\Omega}{R^n u_x}\right)^2\right) \Bigg\}, \end{aligned} \tag{4.16}$$

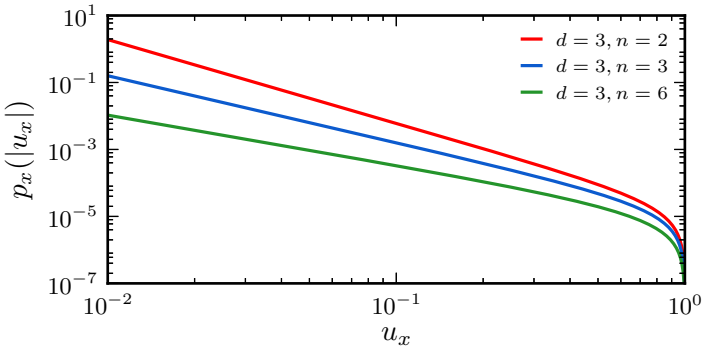

Fig. 4.3: The marginal probability distribution $p_x(|u_x|)$ for a single source. We took $\lambda = 1$, $\Omega(\hat{\mathbf{r}}) = 1$, $a = 1$, and $R = 25$. Essentially, $p_x(|u_x|)$ is a power-law, except near $u_{\max} = 1$.

and, for $|u_x| > |\lambda|\Omega/R^n$,

$$\int_0^{[(\lambda\Omega/a^n)^2 - u_x^2]^{1/2}} \frac{u_\rho^{d-2}}{(u_x^2 + u_\rho^2)^{(d+\alpha)/2}}\, du_\rho = \frac{1}{(d-1)|u_x|^{d+\alpha}} \left[\left(\frac{\lambda\Omega}{a^n}\right)^2 - u_x^2 \right]^{(d-1)/2} \times {}_2F_1\left(\frac{d-1}{2}, \frac{d+\alpha}{2}; \frac{1+d}{2}; 1 - \left(\frac{\lambda\Omega}{a^n u_x}\right)^2 \right), \tag{4.17}$$

where ${}_2F_1(a_1, a_2; b_1; z)$ is Gauss's hypergeometric function. Combining Eqs. (4.16) and (4.17) gives

$$\begin{aligned} p_x(|u_x|) = \Gamma\left(\frac{d}{2}\right)\Gamma\left(\frac{1+d}{2}\right)^{-1} \frac{\alpha|\lambda|^\alpha}{2\pi^{1/2}(R^d - a^d)|u_x|^{d+\alpha}} \int_0^\infty g(\Omega)\Omega^\alpha \\ \times \left\{ \left[\left(\frac{\lambda\Omega}{a^n}\right)^2 - u_x^2 \right]^{(d-1)/2} {}_2F_1\left(\frac{d-1}{2}, \frac{d+\alpha}{2}; \frac{1+d}{2}; 1 - \left(\frac{\lambda\Omega}{a^n u_x}\right)^2 \right) \right. \\ - \left[\left(\frac{\lambda\Omega}{R^n}\right)^2 - u_x^2 \right]^{(d-1)/2} {}_2F_1\left(\frac{d-1}{2}, \frac{d+\alpha}{2}; \frac{1+d}{2}; 1 - \left(\frac{\lambda\Omega}{R^n u_x}\right)^2 \right) \\ \left. \times \Theta\left(\frac{|\lambda|\Omega}{R^n} - |u_x|\right) \right\} \Theta\left(\frac{|\lambda|\Omega}{a^n} - |u_x|\right) d\Omega. \end{aligned} \tag{4.18}$$

We plot $p_x(|u_x|)$ in Fig. 4.3. It behaves as a power-law that decays like $|u_x|^{-1-\alpha}$ until the truncation becomes relevant around the extreme values.

4.3 The probability distribution for many sources

4.3.1 The characteristic function

Suppose the net field $\mathbf{u}$ from a population of N independent sources is $\mathbf{u} = \sum_{i=1}^{N} \mathbf{u}_i$, where each $\mathbf{u}_i$ corresponds to a single source. Given the sources are independent, the probability distribution of $\mathbf{u}$, denoted by $P(\mathbf{u})$ in the thermodynamic limit, is the convolution of $p(\mathbf{u})$ with itself repeated $N-1$ times. The characteristic function $P(\mathbf{k})$ may be expressed concisely using the convolution theorem,

$$P(\mathbf{k}) = \lim_{N\to\infty, R\to\infty} p(\mathbf{k})^N = \lim_{N\to\infty, R\to\infty} \left(\int e^{i\mathbf{k}\cdot\mathbf{u}} p(\mathbf{u})\, d^d u \right)^N. \tag{4.19}$$

We seek to determine $P(\mathbf{k})$, and therefore $P(\mathbf{u})$, without invoking a probability distribution from a limit theorem.

To proceed, we take the Fourier transform of Eq. (4.9). Since $p(u)$ depends only on the magnitude of $\mathbf{u}$, we use a Fourier kernel particular to radially symmetric functions, see Appendix B,

$$\begin{aligned} p(k) &= \int e^{i\mathbf{k}\cdot\mathbf{u}} p(u)\, d^d u \\ &= 2\pi^{d/2}\Gamma\left(\frac{d}{2}\right)^{-1} \int_0^\infty {}_0F_1\left(;\frac{d}{2};-\left(\frac{ku}{2}\right)^2\right) p(u) u^{d-1}\, du \\ &= \frac{\alpha|\lambda|^\alpha}{R^d - a^d} \int_0^\infty g(\Omega) \left[\int_{|\lambda|\Omega/R^n}^{|\lambda|\Omega/a^n} {}_0F_1\left(;\frac{d}{2};-\left(\frac{ku}{2}\right)^2\right) u^{-(1+\alpha)}\, du \right] \Omega^\alpha d\Omega. \end{aligned} \tag{4.20}$$

The inner integral can be evaluated in terms of the Meijer G-function, whose relevant properties are listed in Appendix C. We first rewrite the Fourier kernel with Eq. (C.5),

$${}_0F_1\left(;\frac{d}{2};-\left(\frac{ku}{2}\right)^2\right) = \Gamma\left(\frac{d}{2}\right) G^{0,1}_{0,2}\left(\left(\frac{2}{ku}\right)^2 \middle| \begin{matrix} 1, d/2 \\ - \end{matrix}\right). \tag{4.21}$$

So, by Eq. (C.4),

$$\begin{aligned} &{}_0F_1\left(;\frac{d}{2};-\left(\frac{ku}{2}\right)^2\right) u^{-(1+\alpha)} \\ &\quad = \Gamma\left(\frac{d}{2}\right)\left(\frac{k}{2}\right)^{1+\alpha} G^{0,1}_{0,2}\left(\left(\frac{2}{ku}\right)^2 \middle| \begin{matrix} (3+\alpha)/2, (1+d+\alpha)/2 \\ - \end{matrix}\right). \end{aligned} \tag{4.22}$$

Applying the integral from Eq. (C.6), then manipulating via Eqs. (C.3) and (C.4), yields

$$\begin{aligned}
&\int {}_0F_1\left(;\frac{d}{2};-\left(\frac{ku}{2}\right)^2\right)u^{-(1+\alpha)}\,du \\
&\quad=\Gamma\left(\frac{d}{2}\right)\left(\frac{k}{2}\right)^{1+\alpha}\int G^{0,1}_{0,2}\left(\left(\frac{2}{ku}\right)^2\,\middle|\,\begin{matrix}(3+\alpha)/2,(1+d+\alpha)/2\\ -\end{matrix}\right)du \\
&\quad=-\Gamma\left(\frac{d}{2}\right)\frac{k^\alpha}{2^{1+\alpha}}G^{0,2}_{1,3}\left(\left(\frac{2}{ku}\right)^2\,\middle|\,\begin{matrix}1,1+\alpha/2,(d+\alpha)/2\\ 0\end{matrix}\right) \\
&\quad=-\Gamma\left(\frac{d}{2}\right)\frac{k^\alpha}{2^{1+\alpha}}G^{2,0}_{3,1}\left(\left(\frac{ku}{2}\right)^2\,\middle|\,\begin{matrix}1\\ 0,-\alpha/2,1-(d+\alpha)/2\end{matrix}\right) \\
&\quad=-\Gamma\left(\frac{d}{2}\right)\frac{1}{2u^\alpha}G^{2,0}_{3,1}\left(\left(\frac{ku}{2}\right)^2\,\middle|\,\begin{matrix}1+\alpha/2\\ \alpha/2,0,1-d/2\end{matrix}\right).
\end{aligned}\tag{4.23}$$

We arrive at

$$\begin{aligned}
p(k)=\Gamma\left(\frac{d}{2}\right)\frac{\alpha R^d}{2(R^d-a^d)}\int_0^\infty g(\Omega)\Bigg[&G^{2,0}_{3,1}\left(\left(\frac{\lambda\Omega k}{2R^n}\right)^2\,\middle|\,\begin{matrix}1+\alpha/2\\ \alpha/2,0,1-d/2\end{matrix}\right)\\
&-\left(\frac{a}{R}\right)^d G^{2,0}_{3,1}\left(\left(\frac{\lambda\Omega k}{2a^n}\right)^2\,\middle|\,\begin{matrix}1+\alpha/2\\ \alpha/2,0,1-d/2\end{matrix}\right)\Bigg]d\Omega.
\end{aligned}\tag{4.24}$$

The Meijer G-function that appears last in Eq. (4.23) has a fundamental role to play. It is defined for all d and α, thereby providing us with a simple, yet general, expression in the Fourier domain. We may represent it using a fractional power and a normal series,

$$\begin{aligned}
-G^{2,0}_{3,1}\left(z\,\middle|\,\begin{matrix}1+\alpha/2\\ \alpha/2,0,1-d/2\end{matrix}\right)&=2\pi\csc\left(\frac{\pi\alpha}{2}\right)\Gamma\left(\frac{\alpha}{2}\right)^{-1}\Gamma\left(\frac{d+\alpha}{2}\right)^{-1}\frac{z^{\alpha/2}}{\alpha}\\
&+4\sum_{\substack{m=0,\\ m\text{ even}}}^{\infty}\cos\left(\frac{\pi m}{2}\right)\Gamma\left(\frac{m}{2}\right)^{-1}\Gamma\left(\frac{d+m}{2}\right)^{-1}\frac{z^{m/2}}{m(m-\alpha)}.
\end{aligned}\tag{4.25}$$

As written, the right-hand side has poles at $\alpha=l$ for any l that is an even positive

integer. These are removed after we formally evaluate

$$\lim_{\alpha\to l}\left[2\pi\csc\left(\frac{\pi\alpha}{2}\right)\Gamma\left(\frac{\alpha}{2}\right)^{-1}\Gamma\left(\frac{d+\alpha}{2}\right)^{-1}\frac{z^{\alpha/2}}{\alpha}\right.$$
$$\left.+\,4\cos\left(\frac{\pi l}{2}\right)\Gamma\left(\frac{l}{2}\right)^{-1}\Gamma\left(\frac{d+l}{2}\right)^{-1}\frac{z^{l/2}}{l(l-\alpha)}\right]$$
$$=\cos\left(\frac{\pi l}{2}\right)\Gamma\left(\frac{l}{2}\right)^{-1}\Gamma\left(\frac{d+l}{2}\right)^{-1}z^{l/2}\left[\frac{2}{l}+\Psi\left(\frac{l}{2}\right)+\Psi\left(\frac{d+l}{2}\right)-\log z\right], \quad (4.26)$$

where $\Psi(z)=\Gamma'(z)/\Gamma(z)$ is the digamma function. So there is a logarithmic term if d is an even multiple of n – a condition never satisfied for $d=3$, but possibly for $d=2$. Otherwise, we sum the series to a generalized hypergeometric function,

$$4\sum_{\substack{m=0,\\ m\text{ even}}}^{\infty}\cos\left(\frac{\pi m}{2}\right)\Gamma\left(\frac{m}{2}\right)^{-1}\Gamma\left(\frac{d+m}{2}\right)^{-1}\frac{z^{m/2}}{m(m-\alpha)}$$
$$=-\frac{2}{\alpha}\Gamma\left(\frac{d}{2}\right)^{-1}{}_1F_2\left(-\frac{\alpha}{2};\frac{d}{2},1-\frac{\alpha}{2};-z\right)\quad(\alpha\neq 2,4,\ldots), \quad (4.27)$$

which puts Eq. (4.25) in a more convenient form,

$$\frac{\alpha}{2}G^{2,0}_{3,1}\left(z\,\middle|\,\begin{matrix}1+\alpha/2\\ \alpha/2,0,1-d/2\end{matrix}\right)=\Gamma\left(\frac{d}{2}\right)^{-1}{}_1F_2\left(-\frac{\alpha}{2};\frac{d}{2},1-\frac{\alpha}{2};-z\right)$$
$$-\pi\csc\left(\frac{\pi\alpha}{2}\right)\Gamma\left(\frac{\alpha}{2}\right)^{-1}\Gamma\left(\frac{d+\alpha}{2}\right)^{-1}z^{\alpha/2}\quad(\alpha\neq 2,4,\ldots). \quad (4.28)$$

The Meijer G-functions of Eq. (4.24) then become generalized hypergeometric functions,

$$p(k)=\frac{R^d}{R^d-a^d}\int_0^\infty g(\Omega)\left[{}_1F_2\left(-\frac{\alpha}{2};\frac{d}{2},1-\frac{\alpha}{2};-\left(\frac{\lambda\Omega k}{2R^n}\right)^2\right)\right.$$
$$\left.-\left(\frac{a}{R}\right)^d{}_1F_2\left(-\frac{\alpha}{2};\frac{d}{2},1-\frac{\alpha}{2};-\left(\frac{\lambda\Omega k}{2a^n}\right)^2\right)\right]d\Omega\quad(\alpha\neq 2,4,\ldots). \quad (4.29)$$

We remark that, except for the transition at $\alpha=2$, Eq. (4.29) covers all $p(u)$ whose variances diverge as $a\to 0$. These have $\alpha<2$.

We are now ready to calculate $P(k)$ directly from $p(k)$. This is done specifically for $\alpha<2$. If R becomes large, then the generalized hypergeometric function that has

a in its argument dominates asymptotically the generalized hypergeometric function that has R in its argument. With this in mind, we expand at large R,

$$ {}_1F_2\left(-\frac{\alpha}{2};\frac{d}{2},1-\frac{\alpha}{2};-\left(\frac{\lambda\Omega k}{2R^n}\right)^2\right)\simeq 1+\frac{\alpha}{2d(2-\alpha)}\left(\frac{\lambda\Omega k}{R^n}\right)^2 \tag{4.30} $$

so, up to $(a/R)^d$,

$$ \begin{aligned} p(k)\simeq{}& 1+\left(\frac{a}{R}\right)^d \\ &\times\left[1-\int_0^\infty g(\Omega)\,{}_1F_2\left(-\frac{\alpha}{2};\frac{d}{2},1-\frac{\alpha}{2};-\left(\frac{\lambda\Omega k}{2a^n}\right)^2\right)d\Omega\right] \quad (\alpha<2). \end{aligned} \tag{4.31} $$

Rewriting in terms of Φ, then taking $N\to\infty$ and $R\to\infty$, produces

$$ \begin{aligned} P(k)={}&\lim_{N\to\infty,R\to\infty}\left\{1+\Gamma\left(\frac{d}{2}\right)^{-1}\frac{2\pi^{d/2}a^d\Phi}{dN}\right. \\ &\left.\times\left[1-\int_0^\infty g(\Omega)\,{}_1F_2\left(-\frac{\alpha}{2};\frac{d}{2},1-\frac{\alpha}{2};-\left(\frac{\lambda\Omega k}{2a^n}\right)^2\right)d\Omega\right]\right\}^N \\ ={}&\exp\left\{\Gamma\left(\frac{d}{2}\right)^{-1}\frac{2\pi^{d/2}a^d\Phi}{d}\right. \\ &\left.\times\left[1-\int_0^\infty g(\Omega)\,{}_1F_2\left(-\frac{\alpha}{2};\frac{d}{2},1-\frac{\alpha}{2};-\left(\frac{\lambda\Omega k}{2a^n}\right)^2\right)d\Omega\right]\right\} \quad (\alpha<2). \end{aligned} \tag{4.32} $$

This probability distribution is intimately related to a sum of truncated power-law random variables, but it never appeared before. It accurately describes the interplay between concentration and truncation.

For the other cases, in which $\alpha\geq 2$, $\mathbf{u}(\mathbf{r})$ is classified as a long-range field. Consequently, a thermodynamic limit does not exist in the usual sense of a fixed concentration. To determine $P(k)$, we expand $p(k)$ from either Eq. (4.24) or (4.29) at large R, stopping at the first-order term. If $\alpha=2$, then this term is proportional to $R^{-2n}\log R$. Otherwise, this term is proportional to R^{-2n}. After redefining Φ to contain everything with R, we repeat exactly what led to Eq. (4.32). Then, for $\alpha>2$, $P(k)$ is a Gaussian distribution whose variance is proportional to a concentration in $2n$ dimensions.

4.3.2 Recovering the limit theorems

It is worth considering how Eq. (4.32) relates to both the central limit theorem and the generalized central limit theorem. As Φ becomes large, we can expand the argument of the exponential in Eq. (4.32),

$$\begin{aligned}
&\Gamma\left(\frac{d}{2}\right)^{-1}\frac{2\pi^{d/2}a^d\Phi}{d} \\
&\quad\times\left[1-\int_0^\infty g(\Omega)\,{}_1F_2\left(-\frac{\alpha}{2};\frac{d}{2},1-\frac{\alpha}{2};-\left(\frac{\lambda\Omega k}{2a^n}\right)^2\right)d\Omega\right] \\
&\simeq -\Gamma\left(\frac{d}{2}\right)^{-1}\frac{\pi^{d/2}\alpha\lambda^2\langle\Omega^2\rangle\Phi k^2}{d^2(2-\alpha)a^{2n-d}},
\end{aligned} \tag{4.33}$$

which leads to the Gaussian distribution

$$P(k)\simeq e^{-(\sigma k)^2/2}\quad(\alpha<2). \tag{4.34}$$

The variance,

$$\sigma^2=\Gamma\left(\frac{d}{2}\right)^{-1}\frac{2\pi^{d/2}\alpha\lambda^2\langle\Omega^2\rangle\Phi}{d^2(2-\alpha)a^{2n-d}}\quad(\alpha<2), \tag{4.35}$$

is exactly that predicted with the central limit theorem.

We recover the generalized central limit theorem by evaluating

$$\begin{aligned}
&\lim_{a\to0}\Gamma\left(\frac{d}{2}\right)^{-1}\frac{2\pi^{d/2}a^d\Phi}{d} \\
&\quad\times\left[1-\int_0^\infty g(\Omega)\,{}_1F_2\left(-\frac{\alpha}{2};\frac{d}{2},1-\frac{\alpha}{2};-\left(\frac{\lambda\Omega k}{2a^n}\right)^2\right)d\Omega\right] \\
&=-\csc\left(\frac{\pi\alpha}{2}\right)\Gamma\left(\frac{\alpha}{2}\right)^{-1}\Gamma\left(\frac{d+\alpha}{2}\right)^{-1}\frac{2^{1-\alpha}\pi^{1+d/2}|\lambda|^\alpha\langle\Omega^\alpha\rangle\Phi k^\alpha}{d},
\end{aligned} \tag{4.36}$$

where we used that

$${}_1F_2\left(-\frac{\alpha}{2};\frac{d}{2},1-\frac{\alpha}{2};-z\right)\simeq\pi\csc\left(\frac{\pi\alpha}{2}\right)\Gamma\left(\frac{d}{2}\right)\Gamma\left(\frac{\alpha}{2}\right)^{-1}\Gamma\left(\frac{d+\alpha}{2}\right)^{-1}z^{\alpha/2} \tag{4.37}$$

at large z. This implies the Lévy stable distribution

$$\lim_{a\to0}P(k)=e^{-(ck)^\alpha}\quad(\alpha<2), \tag{4.38}$$

whose scale c comes from

$$c^\alpha = \csc\left(\frac{\pi\alpha}{2}\right)\Gamma\left(\frac{\alpha}{2}\right)^{-1}\Gamma\left(\frac{d+\alpha}{2}\right)^{-1}\frac{2^{1-\alpha}\pi^{1+d/2}|\lambda|^\alpha\langle\Omega^\alpha\rangle\Phi}{d} \quad (\alpha<2). \tag{4.39}$$

As usual, the variance of Eq. (4.38) diverges.

4.3.3 Picking some effective cutoffs

Eq. (4.32) is complicated by the average over Ω in the argument of the exponential. Although $P(k)$ is exact, a simple approximation to $P(k)$ may be more useful. Rather than derive $P(k)$ from cutoffs in r, we could impose effective cutoffs in u like, say, $\widetilde{u}_{\min} = |\lambda|\widetilde{\Omega}_{\min}/R^n$ and $\widetilde{u}_{\max} = |\lambda|\widetilde{\Omega}_{\max}/a^n$. For a single source, the probability distribution that corresponds to these effective cutoffs is

$$\begin{aligned}\widetilde{p}(u) &= \Gamma\left(\frac{d}{2}\right)\frac{\alpha(\widetilde{u}_{\min}\widetilde{u}_{\max})^\alpha}{2\pi^{d/2}(\widetilde{u}_{\max}^\alpha-\widetilde{u}_{\min}^\alpha)u^{d+\alpha}}\Theta(u-\widetilde{u}_{\min})\Theta(\widetilde{u}_{\max}-u)\\ &= \Gamma\left(\frac{d}{2}\right)\frac{\alpha(|\lambda|\widetilde{\Omega}_{\min}\widetilde{\Omega}_{\max})^\alpha}{2\pi^{d/2}(\widetilde{\Omega}_{\max}^\alpha R^d-\widetilde{\Omega}_{\min}^\alpha a^d)u^{d+\alpha}}\Theta\left(u-\frac{|\lambda|\widetilde{\Omega}_{\min}}{R^n}\right)\Theta\left(\frac{|\lambda|\widetilde{\Omega}_{\max}}{a^n}-u\right).\end{aligned} \tag{4.40}$$

If we repeat the derivation of $P(k)$ using $\widetilde{p}(u)$ instead of $p(u)$, then the probability distribution in the thermodynamic limit is

$$\begin{aligned}\widetilde{P}(k) = \exp\Bigg\{&\Gamma\left(\frac{d}{2}\right)^{-1}\left(\frac{\widetilde{\Omega}_{\min}}{\widetilde{\Omega}_{\max}}\right)^\alpha\frac{2\pi^{d/2}a^d\Phi}{d}\\ &\times\left[1-{}_1F_2\left(-\frac{\alpha}{2};\frac{d}{2},1-\frac{\alpha}{2};-\left(\frac{\lambda\widetilde{\Omega}_{\max}k}{2a^n}\right)^2\right)\right]\Bigg\} \quad (\alpha<2).\end{aligned} \tag{4.41}$$

At large Φ, there is an effective Gaussian distribution,

$$\widetilde{P}(k) \simeq e^{-(\widetilde{\sigma}k)^2/2} \quad (\alpha<2) \tag{4.42}$$

with

$$\widetilde{\sigma}^2 = \Gamma\left(\frac{d}{2}\right)^{-1}\frac{2\pi^{d/2}\alpha\lambda^2\widetilde{\Omega}_{\min}^\alpha\widetilde{\Omega}_{\max}^{2-\alpha}\Phi k^2}{d^2(2-\alpha)a^{2n-d}} \quad (\alpha<2), \tag{4.43}$$

and, as $a\to 0$, there is an effective Lévy stable distribution,

$$\lim_{a\to 0}\widetilde{P}(k) = e^{-(\widetilde{c}k)^\alpha} \quad (\alpha<2) \tag{4.44}$$

with

$$\widetilde{c}^{\alpha} = \csc\left(\frac{\pi\alpha}{2}\right)\Gamma\left(\frac{\alpha}{2}\right)^{-1}\Gamma\left(\frac{d+\alpha}{2}\right)^{-1}\frac{2^{1-\alpha}\pi^{1+d/2}|\lambda|^{\alpha}\widetilde{\Omega}_{\min}^{\alpha}\Phi}{d} \quad (\alpha < 2). \tag{4.45}$$

The accuracy of $\widetilde{P}(k)$ ultimately depends on $\widetilde{\Omega}_{\min}$ and $\widetilde{\Omega}_{\max}$.

There is no perfect way to choose $\widetilde{\Omega}_{\min}$ and $\widetilde{\Omega}_{\max}$. Motivated by the limit theorems, we demand that $\widetilde{P}(k)$ must equal $P(k)$ should either $a \to 0$ or Φ become large. Then

$$\widetilde{c} = c, \tag{4.46a}$$

$$\widetilde{\sigma} = \sigma, \tag{4.46b}$$

which further implies

$$\widetilde{\Omega}_{\min}^{\alpha} = \langle\Omega^{\alpha}\rangle, \tag{4.47a}$$

$$\widetilde{\Omega}_{\min}^{\alpha}\widetilde{\Omega}_{\max}^{2-\alpha} = \langle\Omega^{2}\rangle. \tag{4.47b}$$

Solving this system of equations for $\widetilde{\Omega}_{\min}$ and $\widetilde{\Omega}_{\max}$, we find

$$\widetilde{\Omega}_{\min} = \langle\Omega^{\alpha}\rangle^{1/\alpha}, \tag{4.48a}$$

$$\widetilde{\Omega}_{\max} = \left(\frac{\langle\Omega^{2}\rangle}{\langle\Omega^{\alpha}\rangle}\right)^{1/(2-\alpha)}. \tag{4.48b}$$

We could always take other values for $\widetilde{\Omega}_{\min}$ and $\widetilde{\Omega}_{\max}$, but Eqs. (4.48) guarantee that we recover both limit theorems from $\widetilde{P}(k)$.

4.3.4 Inversion of the characteristic function

Our $P(k)$ reflects very different behavior in $P(u)$ as Φ changes. To illustrate this, we derive asymptotic expressions for the effective marginal probability distribution $\widetilde{P}_x(|u_x|)$, verified by numerically inverting its characteristic function $\widetilde{P}_x(|k_x|) = \widetilde{P}(|k_x|)$. Working with $\widetilde{P}_x(|k_x|)$ instead of the exact marginal probability distribution $P_x(|k_x|) = P(|k_x|)$ evades the integral from Eq. (4.32), though what follows can also be done for

some particular $\Omega(\hat{\mathbf{r}})$. But, if $\widetilde{P}(k)$ is sufficiently close to $P(k)$, then so are these expressions.

Suppose Φ is small. We expand Eq. (4.41) with respect to Φ,

$$\widetilde{P}_x(|k_x|) \simeq 1 + \Gamma\left(\frac{d}{2}\right)^{-1}\left(\frac{\widetilde{\Omega}_{\min}}{\widetilde{\Omega}_{\max}}\right)^{\alpha}\frac{2\pi^{d/2}a^d\Phi}{d} \times\left[1 - {}_1F_2\left(-\frac{\alpha}{2};\frac{d}{2},1-\frac{\alpha}{2};-\left(\frac{\lambda\widetilde{\Omega}_{\max}k_x}{2a^n}\right)^2\right)\right] \quad (\alpha<2), \tag{4.49}$$

which is valid specifically for

$$\Gamma\left(\frac{d}{2}\right)^{-1}\left(\frac{\widetilde{\Omega}_{\min}}{\widetilde{\Omega}_{\max}}\right)^{\alpha}\frac{\pi^{d/2}a^d\Phi}{d} \ll 1. \tag{4.50}$$

Inverting the Fourier transform leads to the effective version of Eq. (4.18) in the thermodynamic limit,

$$\begin{aligned}\widetilde{P}_x(|u_x|) &\simeq \delta(u_x) + \Gamma\left(\frac{d}{2}\right)^{-1}\left(\frac{\widetilde{\Omega}_{\min}}{\widetilde{\Omega}_{\max}}\right)^{\alpha}\frac{\pi^{d/2-1}a^d\Phi}{d} \\ &\quad\times\int_{-\infty}^{\infty}e^{-ik_x|u_x|}\left[1 - {}_1F_2\left(-\frac{\alpha}{2};\frac{d}{2},1-\frac{\alpha}{2};-\left(\frac{\lambda\widetilde{\Omega}_{\max}k_x}{2a^n}\right)^2\right)\right]dk_x \\ &\simeq \Gamma\left(\frac{1+d}{2}\right)^{-1}\frac{\pi^{(d-1)/2}\alpha(|\lambda|\widetilde{\Omega}_{\min})^{\alpha}\Phi}{d|u_x|^{d+\alpha}} \\ &\quad\times\left[\left(\frac{\lambda\widetilde{\Omega}_{\max}}{a^n}\right)^2 - u_x^2\right]^{(d-1)/2}{}_2F_1\left(\frac{d-1}{2},\frac{d+\alpha}{2};\frac{1+d}{2};1-\left(\frac{\lambda\widetilde{\Omega}_{\max}}{a^nu_x}\right)^2\right) \\ &\quad\times\Theta\left(\frac{|\lambda|\widetilde{\Omega}_{\max}}{a^n} - |u_x|\right) \quad (\alpha<2).\end{aligned} \tag{4.51}$$

This is basically a truncated power-law. We illustrate Eq. (4.51) in Fig. 4.4.

Moving on to large Φ, the saddlepoint method [106, 107] can be used to approximate

$$\widetilde{P}_x(|u_x|) = \frac{1}{2\pi}\int_{-\infty}^{\infty}\exp\left\{-ik_x|u_x| + \Gamma\left(\frac{d}{2}\right)^{-1}\left(\frac{\widetilde{\Omega}_{\min}}{\widetilde{\Omega}_{\max}}\right)^{\alpha}\frac{2\pi^{d/2}a^d\Phi}{d} \times\left[1 - {}_1F_2\left(-\frac{\alpha}{2};\frac{d}{2},1-\frac{\alpha}{2};-\left(\frac{\lambda\widetilde{\Omega}_{\max}k_x}{2a^n}\right)^2\right)\right]\right\}dk_x \quad (\alpha<2). \tag{4.52}$$

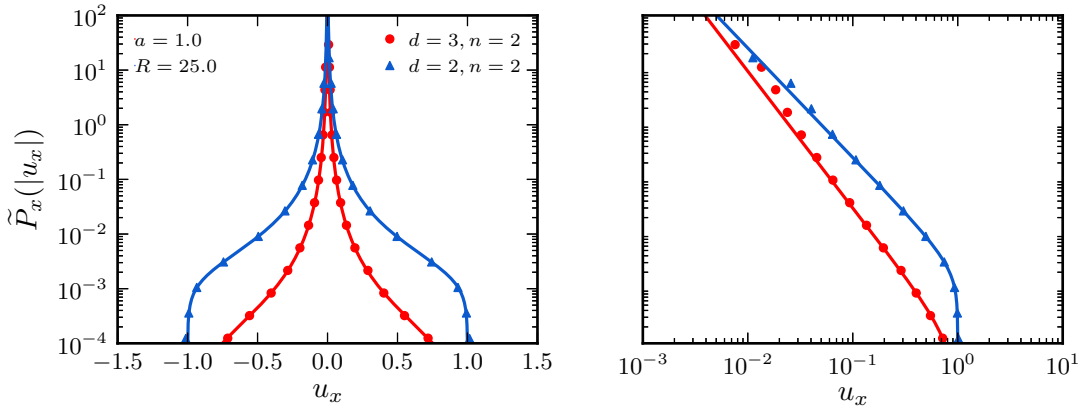

Fig. 4.4: The effective probability distribution $\widetilde{P}_x(|u_x|)$ at small concentrations. We set $\lambda = 1$ and $\widetilde{\Omega}_{\min} = \widetilde{\Omega}_{\max} = 1$, as well as $\Phi = 7.6\times10^{-5}$ for $d = 3$ and $\Phi = 2.6\times10^{-3}$ for $d = 2$. The solid curves are the asymptotic expression, Eq. (4.51), and the symbols are the simulation data.

We first rotate the contour so that it is parallel to the imaginary axis by changing variables to $\kappa_x = ik_x$, then integrate through the saddlepoint ζ_x,

$$\widetilde{P}_x(|u_x|) = \frac{1}{2\pi i}\int_{\zeta_x-i\infty}^{\zeta_x+i\infty} \exp\left\{ -\kappa_x|u_x| + \Gamma\left(\frac{d}{2}\right)^{-1}\left(\frac{\widetilde{\Omega}_{\min}}{\widetilde{\Omega}_{\max}}\right)^{\alpha}\frac{2\pi^{d/2}a^d\Phi}{d} \times\left[1 - {}_1F_2\left(-\frac{\alpha}{2};\frac{d}{2},1-\frac{\alpha}{2};\left(\frac{\lambda\widetilde{\Omega}_{\max}\kappa_x}{2a^n}\right)^2\right)\right]\right\} d\kappa_x \quad (\alpha<2). \tag{4.53}$$

Defining ζ_x implicitly as the real root of

$$\begin{aligned}
|u_x| &= \Gamma\left(\frac{d}{2}\right)^{-1}\left(\frac{\widetilde{\Omega}_{\min}}{\widetilde{\Omega}_{\max}}\right)^{\alpha}\frac{2\pi^{d/2}a^d\Phi}{d} \\
&\quad\times\frac{\partial}{\partial\kappa_x}\left[1 - {}_1F_2\left(-\frac{\alpha}{2};\frac{d}{2},1-\frac{\alpha}{2};\left(\frac{\lambda\widetilde{\Omega}_{\max}\kappa_x}{2a^n}\right)^2\right)\right]\Bigg|_{\kappa_x=\zeta_x} \\
&= -\Gamma\left(\frac{d}{2}\right)^{-1}\left(\frac{\widetilde{\Omega}_{\min}}{\widetilde{\Omega}_{\max}}\right)^{\alpha}\frac{2\pi^{d/2}a^d\Phi}{d} \\
&\quad\times\frac{\partial}{\partial\kappa_x}{}_1F_2\left(-\frac{\alpha}{2};\frac{d}{2},1-\frac{\alpha}{2};\left(\frac{\lambda\widetilde{\Omega}_{\max}\kappa_x}{2a^n}\right)^2\right)\Bigg|_{\kappa_x=\zeta_x} \\
&= \Gamma\left(\frac{d}{2}\right)^{-1}\frac{2\pi^{d/2}\alpha\lambda^2\widetilde{\Omega}_{\min}^{\alpha}\widetilde{\Omega}_{\max}^{2-\alpha}\Phi\zeta_x}{d^2(2-\alpha)a^{2n-d}} \\
&\quad\times{}_1F_2\left(1-\frac{\alpha}{2};1+\frac{d}{2},2-\frac{\alpha}{2};\left(\frac{\lambda\widetilde{\Omega}_{\max}\zeta_x}{2a^n}\right)^2\right),
\end{aligned} \tag{4.54}$$

we have

$$\widetilde{P}_x(|u_x|) \simeq \Bigg[-\Gamma\left(\frac{d}{2}\right)^{-1}\left(\frac{\widetilde{\Omega}_{\min}}{\widetilde{\Omega}_{\max}}\right)^{\alpha}\frac{4\pi^{1+d/2}a^d\Phi}{d}$$
$$\times \frac{\partial^2}{\partial\kappa_x^2}{}_1F_2\left(-\frac{\alpha}{2};\frac{d}{2},1-\frac{\alpha}{2};\left(\frac{\lambda\widetilde{\Omega}_{\max}\kappa_x}{2a^n}\right)^2\right)\Bigg|_{\kappa_x=\zeta_x}\Bigg]^{-1/2}$$
$$\times \exp\Bigg\{ -\zeta_x|u_x| + \Gamma\left(\frac{d}{2}\right)^{-1}\left(\frac{\widetilde{\Omega}_{\min}}{\widetilde{\Omega}_{\max}}\right)^{\alpha}\frac{2\pi^{d/2}a^d\Phi}{d}$$
$$\times\left[1-{}_1F_2\left(-\frac{\alpha}{2};\frac{d}{2},1-\frac{\alpha}{2};\left(\frac{\lambda\widetilde{\Omega}_{\max}\zeta_x}{2a^n}\right)^2\right)\right]\Bigg\} \quad (\alpha<2). \tag{4.55}$$

Since we cannot explicitly solve Eq. (4.54) to find ζ_x, we estimate its asymptotic behavior. If ζ_x is small, then

$${}_1F_2\left(1-\frac{\alpha}{2};1+\frac{d}{2},2-\frac{\alpha}{2};\left(\frac{\lambda\widetilde{\Omega}_{\max}\zeta_x}{2a^n}\right)^2\right) \simeq 1+\frac{(2-\alpha)}{2(2+d)(4-\alpha)}\left(\frac{\lambda\widetilde{\Omega}_{\max}\zeta_x}{a^n}\right)^2. \tag{4.56}$$

At leading order, Eq. (4.54) becomes

$$|u_x| \simeq \Gamma\left(\frac{d}{2}\right)^{-1}\frac{2\pi^{d/2}\alpha\lambda^2\widetilde{\Omega}_{\min}^{\alpha}\widetilde{\Omega}_{\max}^{2-\alpha}\Phi\zeta_x}{d^2(2-\alpha)a^{2n-d}}, \tag{4.57}$$

or, equivalently,

$$\zeta_x \simeq \Gamma\left(\frac{d}{2}\right)\frac{d^2(2-\alpha)a^{2n-d}|u_x|}{2\pi^{d/2}\alpha\lambda^2\widetilde{\Omega}_{\min}^{\alpha}\widetilde{\Omega}_{\max}^{2-\alpha}\Phi}. \tag{4.58}$$

Comparing both terms in Eq. (4.56) gives a condition of validity,

$$\frac{2-\alpha}{2(2+d)(4-\alpha)}\left(\frac{\lambda\widetilde{\Omega}_{\max}\zeta_x}{a^n}\right)^2 \ll 1, \tag{4.59}$$

which we rewrite as

$$|u_x| \ll \Gamma\left(\frac{d}{2}\right)^{-1}\left[\frac{8\pi^d(2+d)(4-\alpha)}{(2-\alpha)^3}\right]^{1/2}\frac{\alpha|\lambda|\widetilde{\Omega}_{\min}^{\alpha}\widetilde{\Omega}_{\max}^{1-\alpha}a^{d-n}\Phi}{d^2}. \tag{4.60}$$

For large ζ_x,

$$\frac{|\lambda|\widetilde{\Omega}_{\max}\zeta_x}{2a^n}{}_1F_2\left(1-\frac{\alpha}{2};1+\frac{d}{2},2-\frac{\alpha}{2};\left(\frac{\lambda\widetilde{\Omega}_{\max}\zeta_x}{2a^n}\right)^2\right)$$
$$\simeq \Gamma\left(\frac{d}{2}\right)\frac{2^{(d-5)/2}d(2-\alpha)}{\pi^{1/2}}\left(\frac{a^n}{|\lambda|\widetilde{\Omega}_{\max}\zeta_x}\right)^{(1+d)/2}e^{|\lambda|\widetilde{\Omega}_{\max}\zeta_x/a^n}. \tag{4.61}$$

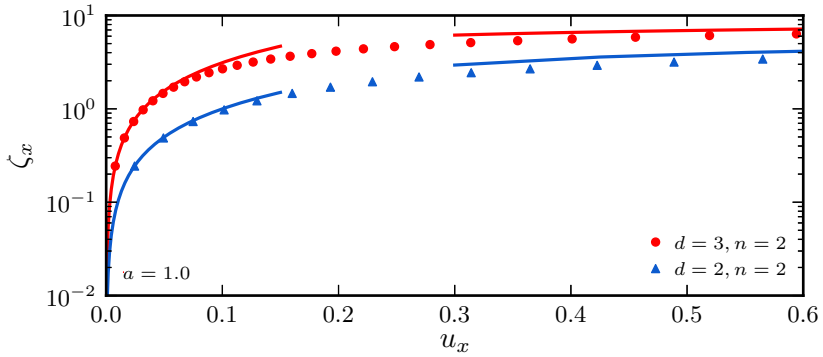

Fig. 4.5: The saddlepoint ζ_x as a function of u_x, compared against its asymptotic expressions. We used the same parameters are those of Fig. 4.6. The solid curves are the asymptotic expressions, either Eq. (4.58) at small $|u_x|$ or Eq. (4.63) at large $|u_x|$, and the symbols are the exact expressions, Eq. (4.54).

So Eq. (4.54) reduces to

$$|u_x| \simeq \frac{(2\pi)^{(d-1)/2}\alpha\widetilde{\Omega}_{\min}^{\alpha}a^{d+(d-1)n/2}\Phi e^{|\lambda|\widetilde{\Omega}_{\max}\zeta_x/a^n}}{d|\lambda|^{(d-1)/2}\widetilde{\Omega}_{\max}^{(d-1)/2+\alpha}\zeta_x^{(1+d)/2}}, \tag{4.62}$$

further implying

$$\zeta_x \simeq -\frac{(1+d)a^n}{2|\lambda|\widetilde{\Omega}_{\max}}W_{-1}\left(-\frac{4\pi}{1+d}\left(\frac{\alpha\widetilde{\Omega}_{\min}^{\alpha}\widetilde{\Omega}_{\max}^{1-\alpha}a^{d-n}|\lambda|\Phi}{2\pi d|u_x|}\right)^{2/(1+d)}\right). \tag{4.63}$$

The Lambert W-function solves the equation $z = W(z)e^{W(z)}$. It is multivalued, but the subscript of '-1' indicates a restriction to the lower branch unique for real arguments between $-1/e$ and 0. Inside this interval, $W_{-1}(z) \leq -1$. We expect

$$\frac{4\pi}{1+d}\left(\frac{\alpha|\lambda|\widetilde{\Omega}_{\min}^{\alpha}\widetilde{\Omega}_{\max}^{1-\alpha}a^{d-n}\Phi}{2\pi d|u_x|}\right)^{2/(1+d)} \ll \frac{1}{e}, \tag{4.64}$$

meaning that

$$|u_x| \gg \left(\frac{4\pi e}{1+d}\right)^{(1+d)/2}\frac{\alpha|\lambda|\widetilde{\Omega}_{\min}^{\alpha}\widetilde{\Omega}_{\max}^{1-\alpha}a^{d-n}\Phi}{2\pi d}. \tag{4.65}$$

We plot ζ_x in Fig. 4.5.

Returning to Eq. (4.54), we insert ζ_x from either Eq. (4.58) or (4.63), depending

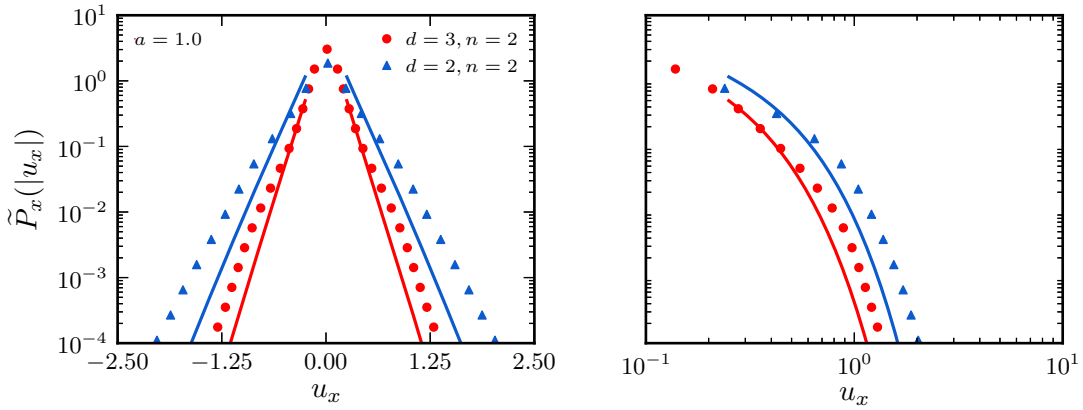

Fig. 4.6: The effective probability distribution $\widetilde{P}_x(|u_x|)$ at large concentrations. We used the same parameters as those of Fig. 4.4, except $\Phi = 7.6 \times 10^{-3}$ for $d = 3$ and $\Phi = 6.4 \times 10^{-2}$ for $d = 2$. The solid curves are the asymptotic expression, Eq. (4.72), and the symbols are the simulation data. As the saddlepoint method typically loses normalization, the curves do not overlay the symbols.

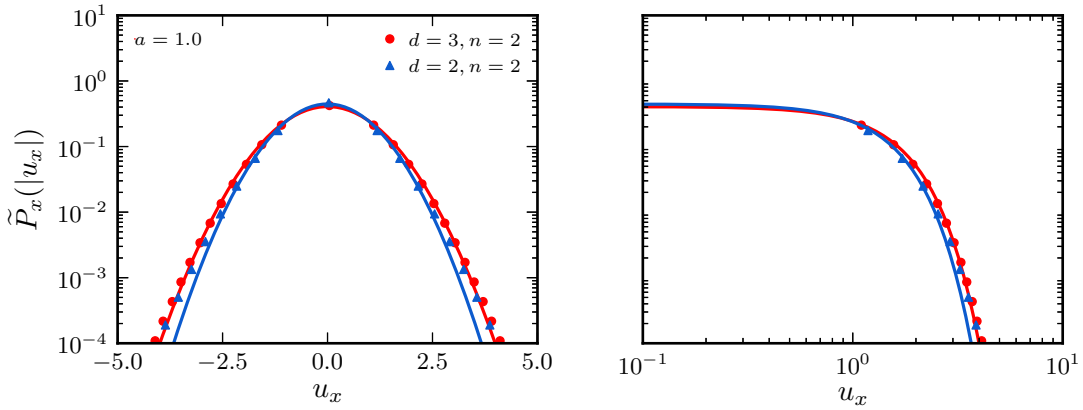

Fig. 4.7: The effective probability distribution $\widetilde{P}_x(|u_x|)$ at very large concentrations. We used the same parameters as those of Fig. 4.4, except $\Phi = 2.3 \times 10^{-1}$ for $d = 3$ and $\Phi = 5.1 \times 10^{-2}$ for $d = 2$. The solid curves are the asymptotic expression, Eq. (4.69), and the symbols are the simulation data.

on whether $|u_x|$ is small or large. Note

$$
\begin{aligned}
&-\frac{\partial^2}{\partial\kappa_x^2}{}_1F_2\left(-\frac{\alpha}{2};\frac{d}{2},1-\frac{\alpha}{2};\left(\frac{\lambda\widetilde{\Omega}_{\max}\kappa_x}{2a^n}\right)^2\right)\Bigg|_{\kappa_x=\zeta_x}\\
&\quad=\frac{\alpha}{d(2-\alpha)}\left(\frac{\lambda\widetilde{\Omega}_{\max}}{a^n}\right)^2\Bigg[{}_1F_2\left(1-\frac{\alpha}{2};1+\frac{d}{2},2-\frac{\alpha}{2};\left(\frac{\lambda\widetilde{\Omega}_{\max}\zeta_x}{2a^n}\right)^2\right)\\
&\qquad+\frac{(2-\alpha)\zeta_x^2}{(2+d)(4-\alpha)}{}_1F_2\left(2-\frac{\alpha}{2};2+\frac{d}{2},3-\frac{\alpha}{2};\left(\frac{\widetilde{\Omega}_{\max}\zeta_x}{2a^n}\right)^2\right)\Bigg].
\end{aligned}
\tag{4.66}
$$

If $|u_x|$ is small,

$$
\begin{aligned}
&-\zeta_x|u_x|+\Gamma\left(\frac{d}{2}\right)^{-1}\left(\frac{\widetilde{\Omega}_{\min}}{\widetilde{\Omega}_{\max}}\right)^{\alpha}\frac{2\pi^{d/2}a^d\Phi}{d}\\
&\qquad\times\left[1-{}_1F_2\left(-\frac{\alpha}{2};\frac{d}{2},1-\frac{\alpha}{2};\left(\frac{\lambda\widetilde{\Omega}_{\max}\zeta_x}{2a^n}\right)^2\right)\right]\\
&\quad\simeq-\Gamma\left(\frac{d}{2}\right)\frac{d^2(2-\alpha)a^{2n-d}|u_x|^2}{4\pi^{d/2}\alpha\lambda^2\widetilde{\Omega}_{\min}^{\alpha}\widetilde{\Omega}_{\max}^{2-\alpha}\Phi}
\end{aligned}
\tag{4.67}
$$

and

$$
\begin{aligned}
&-\Gamma\left(\frac{d}{2}\right)^{-1}\left(\frac{\widetilde{\Omega}_{\min}}{\widetilde{\Omega}_{\max}}\right)^{\alpha}\frac{4\pi^{1+d/2}a^d\Phi}{d}\\
&\qquad\times\frac{\partial^2}{\partial\kappa_x^2}{}_1F_2\left(-\frac{\alpha}{2};\frac{d}{2},1-\frac{\alpha}{2};\left(\frac{\lambda\widetilde{\Omega}_{\max}\kappa_x}{2a^n}\right)^2\right)\Bigg|_{\kappa_x=\zeta_x}\\
&\quad\simeq\Gamma\left(\frac{d}{2}\right)^{-1}\frac{4\pi^{1+d/2}\alpha\lambda^2\widetilde{\Omega}_{\min}^{\alpha}\widetilde{\Omega}_{\max}^{2-\alpha}\Phi}{d^2(2-\alpha)a^{2n-d}},
\end{aligned}
\tag{4.68}
$$

leading to the Gaussian core

$$
\begin{aligned}
\widetilde{P}_x(|u_x|)\simeq&\left[\Gamma\left(\frac{d}{2}\right)\frac{d^2(2-\alpha)a^{2n-d}}{4\pi^{1+d/2}\alpha\lambda^2\widetilde{\Omega}_{\min}^{\alpha}\widetilde{\Omega}_{\max}^{2-\alpha}\Phi}\right]^{1/2}\\
&\times\exp\left[-\Gamma\left(\frac{d}{2}\right)\frac{d^2(2-\alpha)a^{2n-d}|u_x|^2}{4\pi^{d/2}\alpha\lambda^2\widetilde{\Omega}_{\min}^{\alpha}\widetilde{\Omega}_{\max}^{2-\alpha}\Phi}\right].
\end{aligned}
\tag{4.69}
$$

This is exactly the same as the effective Gaussian distribution defined by Eq. (4.42),

as it should be. For large $|u_x|$,

$$
\begin{aligned}
&-\zeta_x|u_x| + \Gamma\left(\frac{d}{2}\right)^{-1}\left(\frac{\widetilde{\Omega}_{\min}}{\widetilde{\Omega}_{\max}}\right)^{\alpha}\frac{2\pi^{d/2}a^d\Phi}{d} \\
&\quad\times\left[1 - {}_1F_2\left(-\frac{\alpha}{2};\frac{d}{2},1-\frac{\alpha}{2};\left(\frac{\lambda\widetilde{\Omega}_{\max}\zeta_x}{2a^n}\right)^2\right)\right] \\
&\simeq -\zeta_x|u_x| + \frac{(2\pi)^{(d-1)/2}\alpha\widetilde{\Omega}_{\min}^{\alpha}a^{(1+d)n/2-d}\Phi e^{|\lambda|\widetilde{\Omega}_{\max}\zeta_x/a^n}}{d|\lambda|^{(1+d)/2}\widetilde{\Omega}_{\max}^{(1+d)/2+\alpha}\zeta_x^{(1+d)/2}} \\
&\simeq \left[1 + \frac{1+d}{2}W_{-1}\left(-\frac{4\pi}{1+d}\left(\frac{\alpha|\lambda|\widetilde{\Omega}_{\min}^{\alpha}\widetilde{\Omega}_{\max}^{1-\alpha}a^{d-n}\Phi}{2\pi d|u_x|}\right)^{2/(1+d)}\right)\right]\frac{a^n|u_x|}{|\lambda|\widetilde{\Omega}_{\max}}
\end{aligned}
\tag{4.70}
$$

and

$$
\begin{aligned}
&-\Gamma\left(\frac{d}{2}\right)^{-1}\left(\frac{\widetilde{\Omega}_{\min}}{\widetilde{\Omega}_{\max}}\right)^{\alpha}\frac{4\pi^{1+d/2}a^d\Phi}{d} \\
&\quad\times\frac{\partial^2}{\partial\kappa_x^2}{}_1F_2\left(-\frac{\alpha}{2};\frac{d}{2},1-\frac{\alpha}{2};\left(\frac{\lambda\widetilde{\Omega}_{\max}\kappa_x}{2a^n}\right)^2\right)\Bigg|_{\kappa_x=\zeta_x} \\
&\simeq \frac{(2\pi)^{(1+d)/2}\alpha|\lambda|^{(3-d)/2}\widetilde{\Omega}_{\min}^{\alpha}a^{d+(d-3)n/2}\Phi e^{|\lambda|\widetilde{\Omega}_{\max}\zeta_x/a^n}}{d\widetilde{\Omega}_{\max}^{(d-3)/2+\alpha}\zeta_x^{(1+d)/2}} \\
&\simeq \frac{2\pi|\lambda|\widetilde{\Omega}_{\max}|u_x|}{a^n},
\end{aligned}
\tag{4.71}
$$

resulting in the near-exponential tails

$$
\begin{aligned}
\widetilde{P}_x(|u_x|) \simeq &\left(\frac{a^n}{2\pi|\lambda|\widetilde{\Omega}_{\max}|u_x|}\right)^{1/2}\exp\left\{\left[1+\frac{1+d}{2}\right.\right. \\
&\left.\left.\times W_{-1}\left(-\frac{4\pi}{1+d}\left(\frac{\alpha|\lambda|\widetilde{\Omega}_{\min}^{\alpha}\widetilde{\Omega}_{\max}^{1-\alpha}a^{d-n}\Phi}{2\pi d|u_x|}\right)^{2/(1+d)}\right)\right]\frac{a^n|u_x|}{|\lambda|\widetilde{\Omega}_{\max}}\right\} \quad (\alpha<2).
\end{aligned}
\tag{4.72}
$$

The functional form of Eq. (4.72) does not depend on n, making it universal to short-range fields. We illustrate Eqs. (4.72) and (4.69) in, respectively, Figs. 4.6 and 4.7.

Eqs. (4.69) and (4.72) suggest another scale appears in the thermodynamic limit. For example, we rewrite the argument of the Lambert W-function from Eq. (4.72),

$$
\begin{aligned}
&-\frac{4\pi}{1+d}\left(\frac{\alpha|\lambda|\widetilde{\Omega}_{\min}^{\alpha}\widetilde{\Omega}_{\max}^{1-\alpha}a^{d-n}\Phi}{2\pi d|u_x|}\right)^{2/(1+d)} = -\frac{4\pi}{1+d}\left[\frac{\alpha(|\lambda|\widetilde{\Omega}_{\min})^{\alpha}\widetilde{u}_{\max}^{1-\alpha}\Phi}{2\pi d|u_x|}\right]^{2/(1+d)} \\
&= -\frac{4\pi}{1+d}\left(\frac{\alpha\widetilde{u}_{\text{many}}^{\alpha}\widetilde{u}_{\max}^{1-\alpha}}{2\pi d|u_x|}\right)^{2/(1+d)},
\end{aligned}
\tag{4.73}
$$

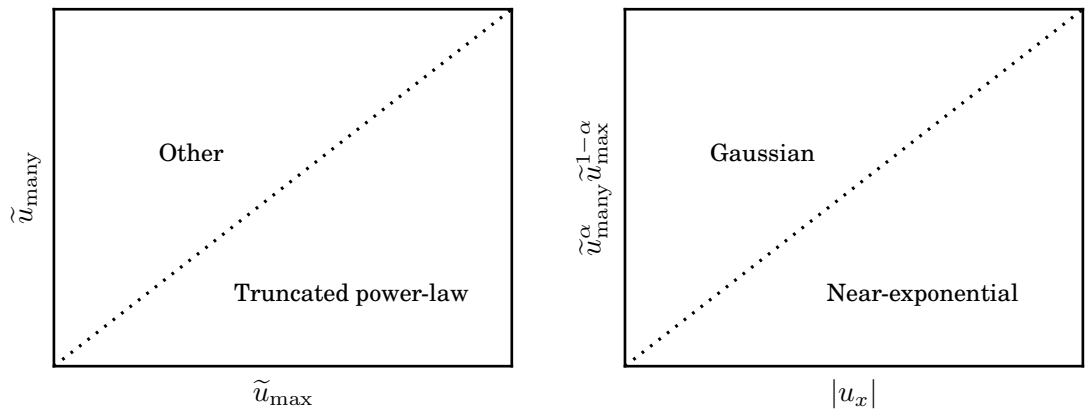

Fig. 4.8: The different behaviors of the effective marginal probability distribution $\widetilde{P}_x(|u_x|)$. For $\widetilde{u}_{\text{many}} \ll \widetilde{u}_{\text{max}}$, $\widetilde{P}_x(|u_x|)$ decays as a truncated power-law (left). Otherwise, there is an asymptotic regime for which $\widetilde{P}_x(|u_x|)$ has parts that are either Gaussian or near-exponential (right).

where $\widetilde{u}_{\text{many}} = |\lambda|\widetilde{\Omega}_{\text{min}}\Phi^{1/\alpha}$. It is not surprising that Φ also sets a scale because, for a fixed d and n, a and Φ are the only parameters important to the thermodynamic limit.

Our expressions can be rewritten in terms of $\widetilde{u}_{\text{many}}$ and $\widetilde{u}_{\text{max}}$. We do this, also dropping some unnecessary constants. When $\widetilde{u}_{\text{many}} \ll \widetilde{u}_{\text{max}}$,

$$\widetilde{P}_x(|u_x|) \simeq \Gamma\left(\frac{1+d}{2}\right)^{-1} \frac{\pi^{(d-1)/2}\alpha\widetilde{u}_{\text{many}}^{\alpha}(\widetilde{u}_{\text{max}}^2 - u_x^2)^{(d-1)/2}}{d|u_x|^{d+\alpha}} \\ \times {}_2F_1\left(\frac{d-1}{2}, \frac{d+\alpha}{2}; \frac{1+d}{2}; 1 - \left(\frac{\widetilde{u}_{\text{max}}}{u_x}\right)^2\right)\Theta(\widetilde{u}_{\text{max}} - |u_x|) \quad (\alpha < 2). \tag{4.74}$$

Otherwise, $\widetilde{P}_x(|u_x|)$ has two parts. Either $|u_x| \ll \widetilde{u}_{\text{many}}^{\alpha}\widetilde{u}_{\text{max}}^{1-\alpha}$,

$$\widetilde{P}_x(|u_x|) \simeq \left[\Gamma\left(\frac{d}{2}\right)\frac{d^2(2-\alpha)}{4\pi^{1+d/2}\alpha\widetilde{u}_{\text{many}}^{\alpha}\widetilde{u}_{\text{max}}^{2-\alpha}}\right]^{1/2} \\ \times \exp\left[-\Gamma\left(\frac{d}{2}\right)\frac{d^2(2-\alpha)u_x^2}{4\pi^{d/2}\alpha\widetilde{u}_{\text{many}}^{\alpha}\widetilde{u}_{\text{max}}^{2-\alpha}}\right] \quad (\alpha < 2), \tag{4.75}$$

or $|u_x| \gg \widetilde{u}_{\rm many}^{\alpha}\widetilde{u}_{\rm max}^{1-\alpha}$,

$$\widetilde{P}_x(|u_x|) \simeq \frac{1}{(2\pi\widetilde{u}_{\rm max}|u_x|)^{1/2}} \exp\left\{\left[1+\frac{1+d}{2}\right.\right.$$
$$\left.\left.\times W_{-1}\left(-\frac{4\pi}{1+d}\left(\frac{\alpha\widetilde{u}_{\rm many}^{\alpha}\widetilde{u}_{\rm max}^{1-\alpha}}{2\pi d|u_x|}\right)^{2/(1+d)}\right)\right]\frac{|u_x|}{\widetilde{u}_{\rm max}}\right\} \quad (\alpha<2). \tag{4.76}$$

We summarize the different behaviors of $\widetilde{P}_x(|u_x|)$ in Fig. 4.8.

All of these expressions are meant only for characterizing $\widetilde{P}_x(|u_x|)$. To capture $\widetilde{P}_x(|u_x|)$ at any scale, the inverse Fourier transform of $\widetilde{P}_x(|k_x|)$ needs to be evaluated accurately. It is probably only possible numerically. Throughout this chapter, we numerically invert $\widetilde{P}_x(|k_x|)$ using a fast Fourier transform (FFT). Due to the generalized hypergeometric function in the exponential of $\widetilde{P}_x(|k_x|)$, a high precision floating-point library is required for sampling $\widetilde{P}_x(|k_x|)$.

4.4 Examples

Let us give some examples that illustrate our theory. All are rather common. For each, we perform simulations and compare the data to the marginal probability distribution $P_x(|u_x|)$, as well as the effective marginal probability distribution $\widetilde{P}_x(|u_x|)$ if appropriate.

4.4.1 Potentials

A very simple power-law field is the force

$$\mathbf{F}(\mathbf{r}) = \frac{\lambda\hat{\mathbf{r}}}{r^n}, \tag{4.77}$$

usually derived from a potential like $V(r) = -\lambda/[(n-1)r^{n-1}]$. If $d=3$ and $n=2$, then $\mathbf{F}(\mathbf{r})$ could represent a point mass or charge. Without a cutoff a, these classical cases are exactly those which inspired the Holtsmark distribution [99, 100].

We identify $\boldsymbol{\Omega}(\hat{\mathbf{r}}) = \hat{\mathbf{r}}$ in Eq. (4.77), which clearly implies $\Omega(\hat{\mathbf{r}}) = 1$. So

$$g(\Omega) = \delta(\Omega - 1) \tag{4.78}$$

and

$$P(k) = \widetilde{P}(k) = \exp\left\{\Gamma\left(\frac{d}{2}\right)^{-1} \frac{2\pi^{d/2} a^d \Phi}{d} \times \left[1 - {}_1F_2\left(-\frac{\alpha}{2}; \frac{d}{2}, 1 - \frac{\alpha}{2}; -\left(\frac{\lambda k}{2a^n}\right)^2\right)\right]\right\}. \tag{4.79}$$

For $\mathbf{F}(\mathbf{r})$, or any field that is isotropic, the exact characteristic function, $P(k)$, is identical to its approximation with effective cutoffs, $\widetilde{P}(k)$.

We plot $p(F)$ and $P_x(|F_x|)$, using $g(\Omega)$ of Eq. (4.78), against data from simulations in, for three dimensions, Figs. 4.9 and 4.10, and, for two dimensions, Figs. 4.11 and 4.12. The sudden decays of $P_x(|F_x|)$ reflect the sharp cutoff of $p(F)$.

4.4.2 Vortices

In three dimensions, the velocity field caused by a vortex of an ideal fluid is [108]

$$\mathbf{v}(\mathbf{r}) = -\frac{\boldsymbol{\omega} \times \hat{\mathbf{r}}}{4\pi r^2}, \tag{4.80}$$

where $\boldsymbol{\omega}$ is the vorticity. A population of vortices has been used to model the velocity fluctuations in fully-developed turbulence [101, 102, 103].

After inspecting Eq. (4.80), we take $\boldsymbol{\Omega}(\hat{\mathbf{r}}) = \boldsymbol{\omega} \times \hat{\mathbf{r}}$. If $\boldsymbol{\omega}$ has an equal probability of pointing in any direction, like for isotropic turbulence, then so does $\boldsymbol{\Omega}$. Assuming ω is not random,

$$g(\Omega) = \delta(\Omega - \omega). \tag{4.81}$$

This means $P(k)$ for our vortices is the same as $P(k)$ for certain potentials, specifically Eq. (4.79) with $d = 3$, $n = 2$, and $\lambda = -\omega/(4\pi)$. As such, Figs. 4.9 and 4.10 are also relevant.

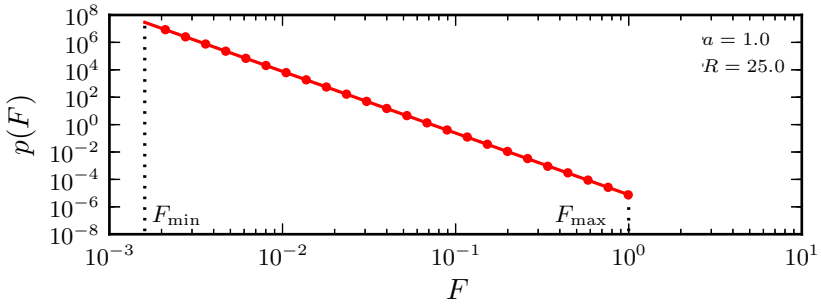

Fig. 4.9: The exact probability distribution $p(F)$ for a single potential in three dimensions. We set $n = 2$ and $\lambda = 1$. The solid curve is the exact expression, from Eq. (4.9) using $g(\Omega)$ of Eq. (4.78), and the symbols are the simulation data. Note the sharp cutoffs at $F_{\min}$ and $F_{\max}$.

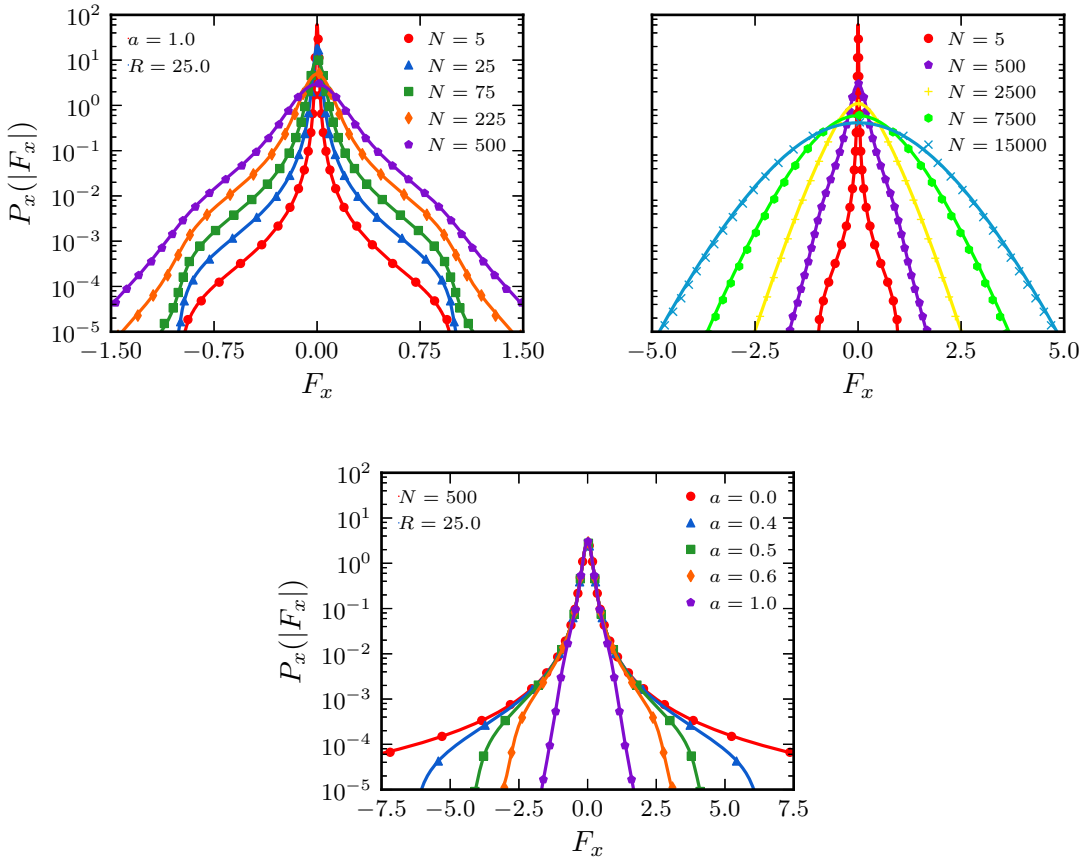

Fig. 4.10: The exact marginal probability distribution $P_x(|F_x|)$ for many potentials in three dimensions. We used the same parameters as those of Fig. 4.9. The solid curves are the exact expression, from Eq. (4.79), and the symbols are the simulation data. As N grows, $P_x(|F_x|)$ exhibits a wide range of shapes (top left and right). As a shrinks, the tails of $P_x(|F_x|)$ broaden until a Lévy stable distribution is recovered (bottom).

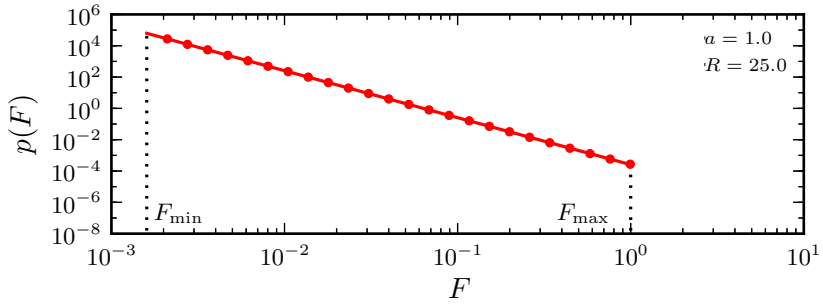

Fig. 4.11: The exact probability distribution $p(F)$ for a single potential in two dimensions. We set $n = 2$ and $\lambda = 1$. The solid curve is the exact expression, from Eq. (4.9) using $g(\Omega)$ of Eq. (4.78), and the symbols are the simulation data.

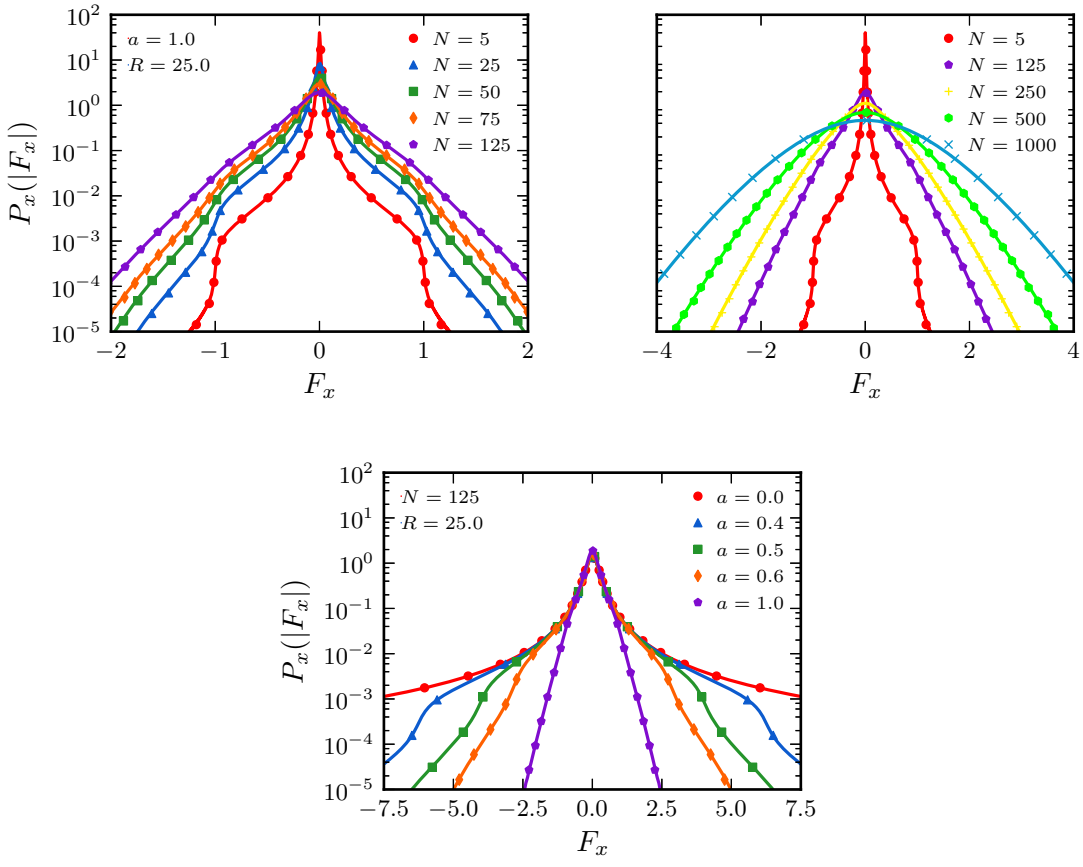

Fig. 4.12: The exact marginal probability distribution $P_x(|F_x|)$ for many potentials in two dimensions. We used the same parameters as those of Fig. 4.11. The solid curves are the exact expression, from Eq. (4.79), and the symbols are the simulation data.

4.4.3 Swimmers

Returning to active suspensions, think again about the velocity field due to a swimming microorganism in three dimensions,

$$\mathbf{u}(\mathbf{r}) = \frac{q[1-3(\hat{\mathbf{r}}\cdot\hat{\mathbf{n}})^2]\hat{\mathbf{r}}}{8\pi\eta r^2}. \tag{4.82}$$

We already know $\alpha = 3/2$ from Chapter 3. Set $\mathbf{\Omega}(\hat{\mathbf{r}}) = [1-3(\hat{\mathbf{r}}\cdot\hat{\mathbf{n}})^2]\hat{\mathbf{r}}$. With $\cos\theta = \hat{\mathbf{r}}\cdot\hat{\mathbf{n}}$, we write the magnitude of $\mathbf{\Omega}(\hat{\mathbf{r}})$ as $\Omega(\cos\theta) = |1-3\cos^2\theta|$. Changing variables to $\chi = \cos\theta$,

$$\begin{aligned} g(\Omega) &= \frac{1}{2}\int_0^\pi \delta(\Omega - |1-3\cos^2\theta|)\sin\theta\, d\theta = \frac{1}{2}\int_{-1}^{1}\delta(\Omega-|1-3\chi^2|)\,d\chi \\ &= \frac{1}{2}\int_{-1/\sqrt{3}}^{1/\sqrt{3}}\delta(\Omega-(1-3\chi^2))\,d\chi + \int_{1/\sqrt{3}}^{1}\delta(\Omega+(1-3\chi^2))\,d\chi. \end{aligned} \tag{4.83}$$

Each integral can be evaluated analytically,

$$\int_{-1/\sqrt{3}}^{1/\sqrt{3}}\delta(\Omega-(1-3\chi^2))\,d\chi = \frac{\Theta(\Omega)\Theta(1-\Omega)}{\sqrt{3}(1-\Omega)^{1/2}}, \tag{4.84a}$$

$$\int_{1/\sqrt{3}}^{1}\delta(\Omega+(1-3\chi^2))\,d\chi = \frac{\Theta(\Omega)\Theta(2-\Omega)}{2\sqrt{3}(1+\Omega)^{1/2}}. \tag{4.84b}$$

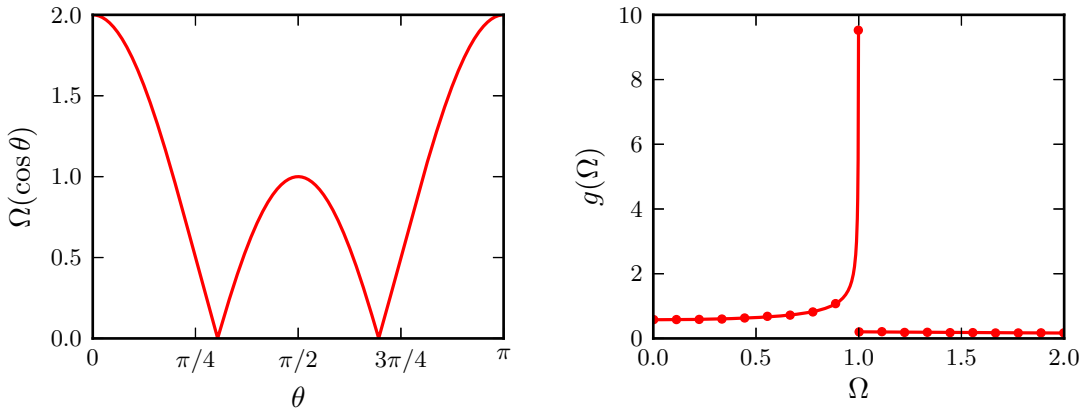

Fig. 4.13: For a swimmer, $\Omega(\cos\theta)$ oscillates between $\Omega_{\min} = 0$ and $\Omega_{\max} = 2$ (left). Its probability distribution $g(\Omega)$ decays sharply from a peak at $\Omega = 1$ to roughly a constant (right). The solid curves are analytic expressions and, for $g(\Omega)$, the symbols are simulation data.

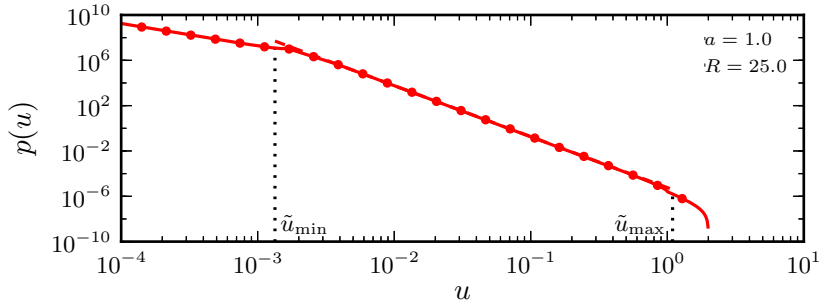

Fig. 4.14: The exact probability distribution $p(u)$, and its effective counterpart $\widetilde{p}(u)$, for a single swimmer in three dimensions. We set $q/(8\pi\eta) = 1$. The solid curve is the exact expression, Eq. (4.9) numerically integrated using $g(\Omega)$ of Eq. (4.83), the dashed curve is the effective expression, Eq. (4.40), and the symbols are the simulation data. Note the cutoffs are smooth, unlike those in Fig. 4.9.

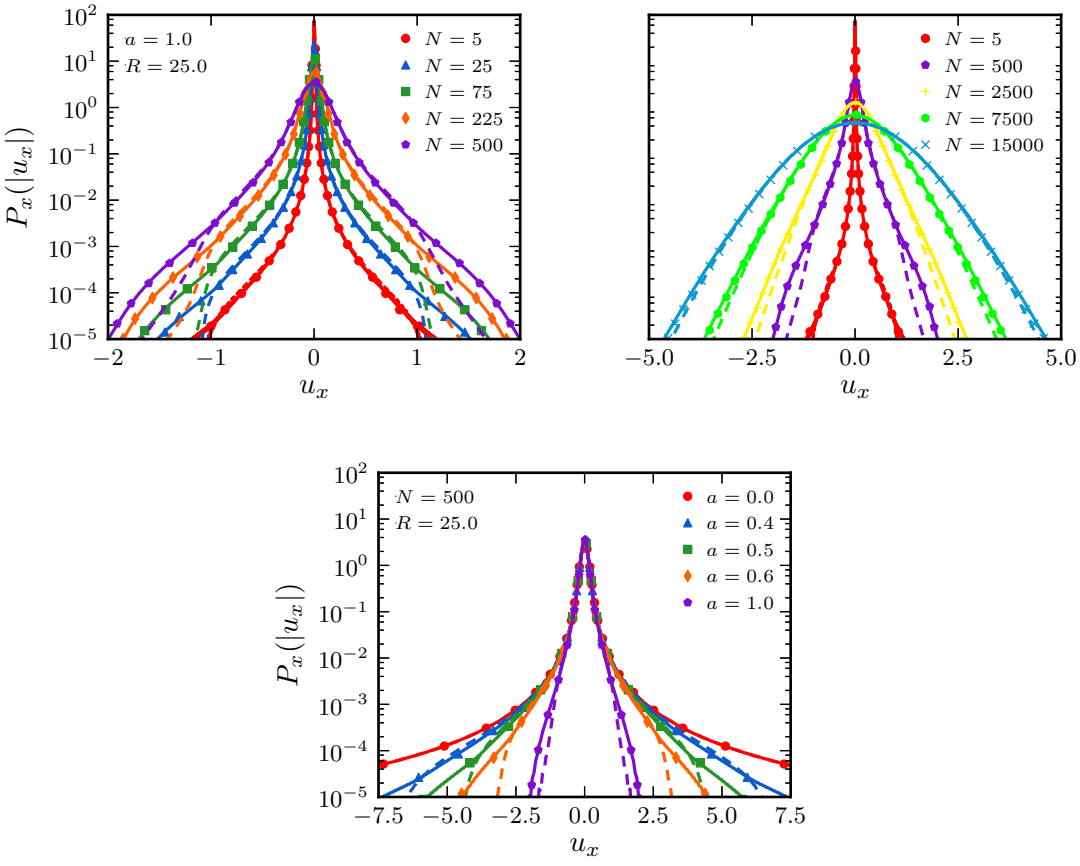

Fig. 4.15: The exact marginal probability distribution $P_x(|u_x|)$, and its effective counterpart $\widetilde{P}_x(|u_x|)$, for many swimmers in three dimensions. We used the same parameters as those of Fig. 4.14. The solid curves are the exact expression, from numerically integrating Eq. (4.32) using $g(\Omega)$ of Eq. (4.83), the dashed curves are the effective expressions, from Eq. (4.41), and the symbols are the simulation data.

Putting Eqs. (4.84) into Eq. (4.83) gives

$$g(\Omega) = \frac{\Theta(\Omega)}{2\sqrt{3}}\left[\frac{\Theta(1-\Omega)}{(1-\Omega)^{1/2}} + \frac{\Theta(2-\Omega)}{(1+\Omega)^{1/2}}\right]. \tag{4.85}$$

This has the moments

$$\langle\Omega^{3/2}\rangle = \frac{2\sqrt{2}+\sqrt{3}(\pi+2\,\mathrm{arcsinh}\,\sqrt{2})}{16} \approx 0.76502708, \tag{4.86a}$$

$$\langle\Omega^{2}\rangle = \frac{4}{5}, \tag{4.86b}$$

which correspond to, from Eqs. (4.48),

$$\widetilde{\Omega}_{\mathrm{min}} \approx 0.83647161, \tag{4.87a}$$

$$\widetilde{\Omega}_{\mathrm{max}} \approx 1.09351905. \tag{4.87b}$$

Fig. 4.13 shows $\Omega(\cos\theta)$ and $g(\Omega)$.

We plot $p(u)$ and $P_x(|u_x|)$, using $g(\Omega)$ of Eq. (4.83), as well as $\widetilde{p}(u)$ and $\widetilde{P}_x(|u_x|)$, using $\widetilde{\Omega}_{\mathrm{min}}$ and $\widetilde{\Omega}_{\mathrm{max}}$ of Eqs. (4.87), against data from simulations in Figs. 4.14 and 4.15. While $p(u)$ and $P_x(|u_x|)$ match throughout, $\widetilde{p}(u)$ and $\widetilde{P}_x(|u_x|)$ look reasonable. The anisotropy in $\mathbf{u}(\mathbf{r})$ seems to smooth the extreme tails of $p(u)$ and $P_x(|u_x|)$.

4.5 Discussion

Power-laws, such as the fields captured by Eq. (4.1), are everywhere in nature. In many cases, they arise as an asymptotic approximation for a more complicated expression. Nevertheless, they may be sufficient to reproduce the general properties of a system.

We derived a probability distribution of the net field $\mathbf{u}$ caused by a population of independent and identically distributed random sources, each of which corresponds to a short-range field, as from Eq. (4.1), with truncation. This is a classical problem [99, 100, 101, 102, 103, 104], but a probability distribution that includes the truncation

was missing. Our probability distribution contains an integral that can be avoided by using a simple approximation involving effective cutoffs.

Rather than a trivial detail, some sort of regularization is actually a fundamental ingredient of any correct theory. We saw this in Chapter 3, but we explored more of the mathematical consequences in this chapter. If there is no regularization, then the probability distribution of $\mathbf{u}$ in the thermodynamic limit is always a Lévy stable distribution. This is physically impossible because $\langle u^2 \rangle$ should not diverge. With regularization, we discovered near-exponential tails that are shared across many systems. Such tails may explain the data from simulations of vortex blobs in Ref. [103].

It is likely that sums of truncated power-law random variables have been observed, but not identifed, rather broadly. We discuss further applications of our results in Chapter 6.

Chapter 5

Non-Gaussian Steady States in Active Reconstituted Networks

5.1 Going bottom-up

Cells are the building blocks of life. Either alone or as part of a community, they are vital to keeping an organism up and running. Taken by itself, a cell is a complex machine, constantly changing its geometric shape and material properties to adapt to its environment. Inside it is noisy and wet, with high concentrations of molecules that must get from place to place relatively cheaply. Under these conditions, some sort of diffusion, if possible, is the vehicle of choice for mixing and transport that does not require energy input. But, given all of the competing effects that occur in cells, there is no reason why it has to be Brownian motion.

There are two approaches to understanding any complex system: top-down (we break it into simpler systems) or bottom-up (we rebuild it part by part). For a long time, biologists mostly took the top-down approach, studying a system either as it was found in nature or after it was modified under controlled conditions. Nowadays, there are tools from molecular biology and optical microscopy that allow us to construct, then observe, *in vitro* models of cellular processes [44, 45]. This kind of bottom-up biology does not aim to replace experiments inside cells, but hopes to offer complementary insights. Outside a cell, a model can be tested and refined independently of

a large number of extra variables, which allows a deeper understanding of the basic science. Looking backward, investigating biology bottom-up is a logical extension of how self-organization was originally explored during chemical reactions with a few simple ingredients [109].

Most structures need the support of a scaffold. In a cell, mechanical stability comes from the cytoskeleton, a fiber network that spans the cytoplasm and links to the plasma membrane [41]. It consists primarily of microtubules, which serve as rigid girders, and microfilaments, which form a flexible mesh. These microfilaments are linear polymers of actin, together behaving like an elastic sheet. As actin polymerizes into a microfilament, a collective pressure is exerted on the plasma membrane that changes the internal organization and external architecture of a cell. Some bacteria nucleate bundles of actin through the plasma membrane, allowing them to crawl on a surface or swim in a fluid [42]. Given that the cytoskeleton is so important to a cell, the first step towards constructing a cell bottom-up is to imitate the cytoskeleton with a reconstituted network of filaments.

Once we have a reconstituted network, we aim to study its properties. We determine its mechanical behavior by applying a stress and measuring the strain (or vice versa). Although the relationship between stress and strain may be complicated, we often find a linear response. In this regime, the fluctuation-dissipation theorem immediately supplies physical quantities, like viscoelastic moduli, from the mean square displacement of a diffusing tracer. There is no need for rheometers, some tracers and a camera will do just fine at room temperature. This is microrheology [110, 111].

With microrheology, it is possible to probe the local mechanics of reconstituted networks like, say, actin. This is done partly to help determine how to imitate a cell *in vitro*. For example, in some early experiments, the elastic moduli of reconstituted networks were measured to be orders of magnitude smaller than those of cells [112, 113]. It turned out that bundling and crosslinking between filaments, normally induced by

accessory proteins inside a cell, dramatically affect the elasticity of a network [114].

Still, elastic filaments and accessory proteins do not represent the entire contents of a cell. A missing ingredient is activity, such as molecular motors powered by adenosine triphosphate (ATP) or guanosine triphosphate (GTP). The non-equilibrium dynamics of interacting motors and filaments turns a passive structure into an active material, much more like the cytoskeleton. Depending on the concentration of motors, this may give rise to self-assembly and self-organization, which we already discussed in Chapter 1. Even at dilute concentrations, the presence of myosin II can render the fluctuation-dissipation theorem invalid [46].

Very recently, some experiments revealed that the fluctuations in an actin network populated with myosin II motors are non-Gaussian [115]. By tracking 1 μm tracers over 100 s, the probability distribution of a tracer displacement was measured and appears strikingly like some of the other probability distributions considered throughout this thesis. We show the measured trajectories in Fig. 5.1, as well as the measured probability distributions in Figs. 5.2 and 5.3. Just as for the swimming microorganisms in Chapter 3, we attribute these non-Gaussian fluctuations to the asymptotic behavior of the displacement field caused by a single myosin. We analyze the displacement imparted to a tracer from a myosin and, using the results of Chapter 4, we predict a non-Gaussian steady state inherent to active reconstituted networks.

5.2 A simple model for myosin II in actin

Out of all motor proteins in the myosin family, myosin II is likely to be the most common [116]. Along with actin, it is part of different proteins found in cardiac, skeletal, and smooth muscle, which generate the force necessary for pumping a fluid or moving an object [42]. Some actin-myosin complexes also modulate cell functions, including adhesion [117], motility [118], and lineage specification [119].

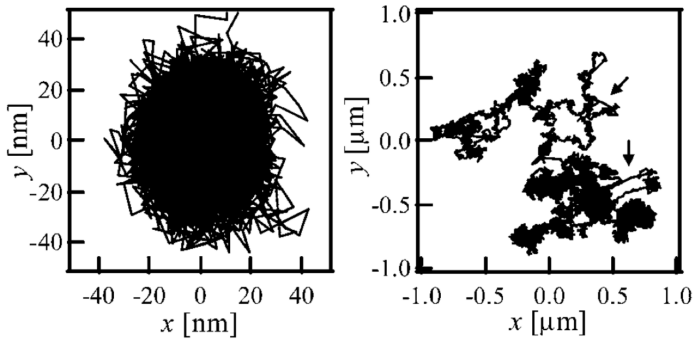

Fig. 5.1: Trajectories of tracers in passive (left) and active (right) reconstituted networks, from Ref. [115]. Without any myosin II, the trajectory is compact. If myosin II is present, then the trajectory has long steps reminiscent of a Lévy flight.

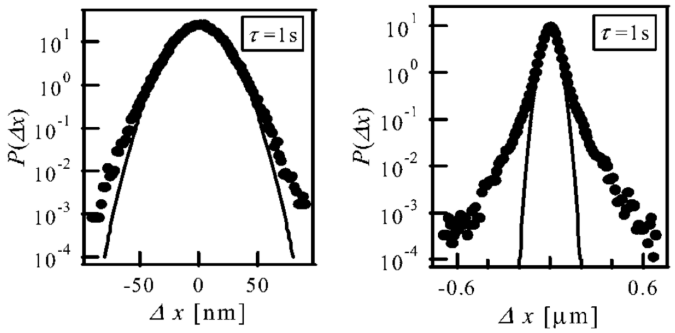

Fig. 5.2: Probability distributions of tracer displacements in passive (left) and active (right) reconstituted networks, from Ref. [115]. Without any myosin II, the probability distribution is a Gaussian distribution. If myosin II is present, then the probability distribution has tails that decay much more slowly.

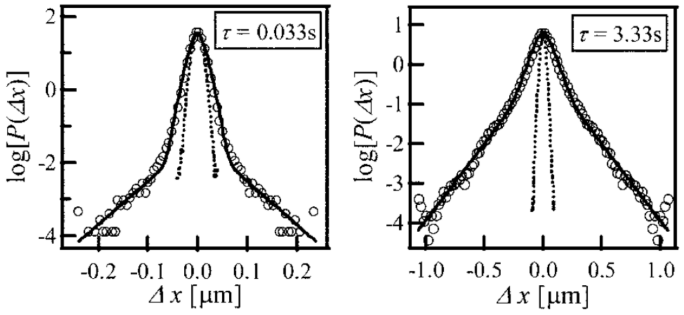

Fig. 5.3: Probability distributions for tracer displacements at times of 0.033 s (left) and 3.33 s (right) in an active reconstituted network, from Ref. [115]. As time evolves, the shape of the probability distribution changes.

Unlike other myosins, which have a head that binds to actin and a tail that anchors the head, myosin II effectively has two heads due to dimerization of its tail. The tails of many myosin II associate to form myosin minifilaments about 1 μm in size [120]. Several heads of a myosin minifilament then bind to an actin filament, increasing the time taken before it fully unbinds. As either end of a myosin minifilament can bind, a myosin minifilament is able to act as a stable crosslinker between a pair of actin filaments. In the presence of ATP, a myosin minifilament becomes a thermodynamic engine that drives actin filaments by producing a contractile force.

At lengths larger than the mesh length and times longer than the relaxation time, a reconstituted network can be modeled as an elastic structure whose displacement field $\mathbf{u}(\mathbf{r})$ is captured by the Navier equations,

$$\mu\nabla^2\mathbf{u}(\mathbf{r}) + (\mu+\lambda)\nabla(\nabla\cdot\mathbf{u}(\mathbf{r})) = 0, \tag{5.1}$$

where μ and λ are the Lamé parameters corresponding to the Poisson ratio $\nu = \lambda/[2(\mu+\lambda)]$. If we wanted to completely describe the network, then we should keep the acceleration term from the Navier-Cauchy equations, and include a coupled fluid in Eq. (5.1) whose velocity field satisfies the Navier-Stokes equations [121]. With some myosin II present, a reconstituted actin network has a mesh length of about 100 nm and a relaxation time of about 100 ms [46]. We expect a continuum model, like Eq. (5.1), to hold beyond these scales.

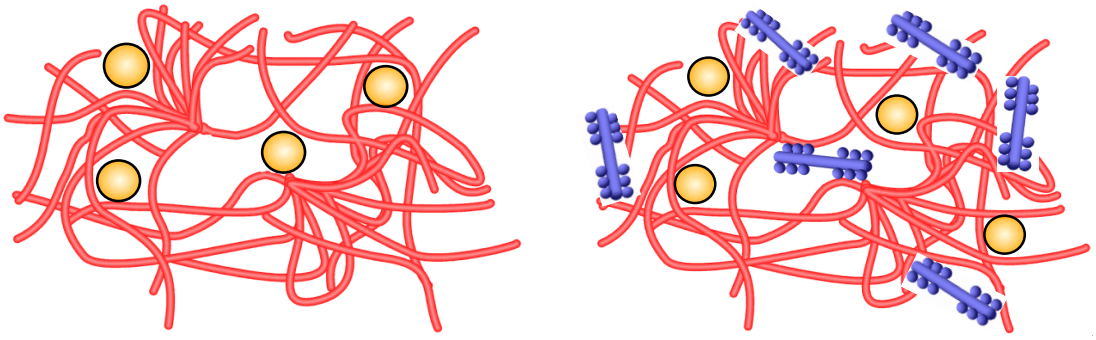

Fig. 5.4: Tracers in passive (left) and active (right) reconstituted networks. Reproduced with permission from Daisuke Mizuno.

Once bound to actin, a myosin minifilament is a pair of equal, but opposite, forces directed along the axes $\pm\hat{\mathbf{n}}$. Like we showed in Chapter 2, this means a myosin minifilament centered at the origin has approximately the dipolar field [122],

$$\mathbf{u}(\mathbf{r},t) = \frac{q(t)\{2(1-2\nu)(\hat{\mathbf{r}}\cdot\hat{\mathbf{n}})\hat{\mathbf{n}} - [1-3(\hat{\mathbf{r}}\cdot\hat{\mathbf{n}})^2]\hat{\mathbf{r}}\}}{16\pi\mu(1-\nu)r^2}. \tag{5.2}$$

The dipole moment $q(t)$ must be time-dependent to account for the mechanics involved in binding and unbinding. During a period roughly between 1 s and 10 s, the stress induced by a myosin minifilament grows slowly until a sudden release [46]. We assume a linear growth $q(t) = \lambda t$, for which λ is the growth rate and t is the time elapsed since a myosin minifilament bound to actin. If a myosin minifilament is unbound from actin, then there is no displacement.

In order to complete the model, we must specify the kinetics involved in binding and unbinding. We simply take an exponential distribution as the probability distribution for each transition time,

$$\psi_{\text{on}}(t) = \kappa_{\text{on}} e^{-\kappa_{\text{on}} t}, \tag{5.3a}$$

$$\psi_{\text{off}}(t) = \kappa_{\text{off}} e^{-\kappa_{\text{off}} t}, \tag{5.3b}$$

where κ_{on} is the binding rate and κ_{off} is the unbinding rate. When a myosin minifilament rebinds, its position and orientation are completely uncorrelated from their earlier values.

5.3 Displacements from elastic equilibrium

A microrheology experiment uses the displacements of tracers to study the properties of a medium. In an elastic medium, all displacements are instantaneous. Neglecting Brownian motion, the displacement $\mathbf{u}$ of a tracer is then exactly the sum over all displacement fields. For a suspension with N myosins, this is just the sum of N displacement fields, each of which follows Eq. (5.2) by taking q, $\mathbf{r}$, and $\hat{\mathbf{n}}$ as random

variables distributed appropriately. Unless stated otherwise, our notation follows that in Chapter 4.

5.3.1 A single myosin minifilament

Consider the tracer displacement from a single myosin minifilament. Like the swimmers in Chapter 3, a myosin minifilament corresponds to a power-law field that, if distributed uniformly in space, has a divergent variance as $a \to 0$. What is different is the motion and medium. A swimmer just swims through a fluid, whereas a myosin minifilament binds to and unbinds from actin. Because $q(t)$ grows constantly while a myosin minifilament stays bound, there is always a spread of dipole moments. How does this change the probability distribution for a displacement?

Before anything else, we must bring $\mathbf{u}(\mathbf{r}, t)$ into the probabilistic framework of Chapter 4. Given $d = 3$ and $n = 2$, the characteristic exponent is again $\alpha = 3/2$. Eq. (5.2) implies

$$\mathbf{\Omega}(\hat{\mathbf{r}}, \hat{\mathbf{n}}) = 2(1 - 2\nu)(\hat{\mathbf{r}} \cdot \hat{\mathbf{n}})\hat{\mathbf{n}} - [1 - 3(\hat{\mathbf{r}} \cdot \hat{\mathbf{n}})^2]\hat{\mathbf{r}}, \tag{5.4}$$

where $\langle \mathbf{\Omega} \rangle = 0$ as expected. Set $\cos\theta = \hat{\mathbf{r}} \cdot \hat{\mathbf{n}}$. The magnitude of $\mathbf{\Omega}(\hat{\mathbf{r}}, \hat{\mathbf{n}})$ is

$$\Omega(\cos\theta) = \{1 - 2[3 + 4\nu(1 - 2\nu)]\cos^2\theta + 3(7 - 8\nu)\cos^4\theta\}^{1/2}. \tag{5.5}$$

It seems $\Omega(\cos\theta)$ is more complicated for a myosin minifilament than that for a swimmer, even $\widetilde{\Omega}_{\text{min}}$ and $\widetilde{\Omega}_{\text{max}}$ using Eqs. (4.48) depend on ν.

We seek the extreme values Ω_{min} and Ω_{max} to compare against $\widetilde{\Omega}_{\text{min}}$ and $\widetilde{\Omega}_{\text{max}}$. In order to find Ω_{min} and Ω_{max}, we differentiate $\Omega(\cos\theta)$ with respect to θ,

$$\frac{d}{d\theta}\Omega(\cos\theta) = \frac{2[3 + 4\nu(1 - 2\nu) - 3(7 - 8\nu)\cos^2\theta]\sin\theta\cos\theta}{\{1 - 2[3 + 4\nu(1 - 2\nu)]\cos^2\theta + 3(7 - 8\nu)\cos^4\theta\}^{1/2}}. \tag{5.6}$$

This vanishes if θ satisfies either $\sin\theta = 0$, $\cos\theta = 0$, or $3 + 4\nu(1 - 2\nu) - 3(7 - 8\nu)\cos^2\theta = 0$. Obviously, $\sin\theta = 0$ means $\theta = 0$ or $\theta = \pi$, for which $\Omega(\pm 1) = 4(1-\nu)$.

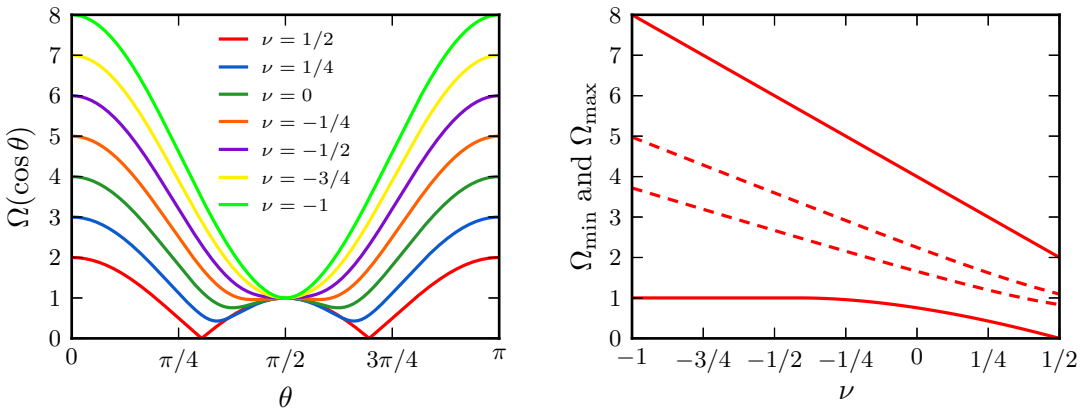

Fig. 5.5: The behavior of $\Omega(\cos\theta)$ depends on ν (left), as does its minimum $\Omega_{\rm min}$ and maximum $\Omega_{\rm max}$ (right). The solid curves are exact expressions and the dashed curves are effective expressions, specifically the effective minimum $\widetilde{\Omega}_{\rm min}$ and maximum $\widetilde{\Omega}_{\rm max}$ from Eqs. (4.48).

Likewise, $\cos\theta = 0$ means $\theta = \pi/2$, for which $\Omega(0) = 1$. Finally, $3 + 4\nu(1-2\nu) - 3(7-8\nu)\cos^2\theta = 0$ means

$$\theta = \arccos\left(\pm \left[\frac{3 + 4\nu(1-2\nu)}{3(7-8\nu)} \right]^{1/2} \right) \qquad \left(\nu \geq \frac{1-\sqrt{7}}{4} \right), \tag{5.7}$$

for which

$$\Omega\left(\pm \left[\frac{3 + 4\nu(1-2\nu)}{3(7-8\nu)} \right]^{1/2} \right) = 2(1-2\nu)\left[\frac{3-4\nu^2}{3(7-8\nu)} \right]^{1/2} \qquad \left(\nu \geq \frac{1-\sqrt{7}}{4} \right). \tag{5.8}$$

Putting it all together,

$$\Omega_{\rm min} = \begin{cases} 1 & \text{if } \nu \leq (1-\sqrt{7})/4, \\ 2(1-2\nu)\{(3-4\nu^2)/[3(7-8\nu)]\}^{1/2} & \text{if } \nu > (1-\sqrt{7})/4, \end{cases} \tag{5.9}$$

and

$$\Omega_{\rm max} = 4(1-\nu). \tag{5.10}$$

We calculate $\widetilde{\Omega}_{\rm min}$ and $\widetilde{\Omega}_{\rm max}$ by numerically integrating to get the fractional moment of order 3/2,

$$\langle \Omega^{3/2} \rangle = \frac{1}{2} \int_0^\pi \{1 - 2[3 + 4\nu(1-2\nu)]\cos^2\theta + 3(7-8\nu)\cos^4\theta\}^{3/4} \sin\theta \, d\theta. \tag{5.11}$$

However, the variance can be determined analytically,

$$\begin{aligned}\langle\Omega^2\rangle &= \frac{1}{2}\int_0^\pi \{1-2[3+4\nu(1-2\nu)]\cos^2\theta+3(7-8\nu)\cos^4\theta\}\sin\theta\,d\theta \\ &= \frac{16(3-7\nu+5\nu^2)}{15}.\end{aligned} \tag{5.12}$$

In Fig. 5.5, we plot $\Omega(\cos\theta)$, together with $\Omega_{\min}$, $\widetilde{\Omega}_{\min}$, $\Omega_{\max}$, and $\widetilde{\Omega}_{\max}$, for various ν.

Moving on, the probability distribution of a dipole moment q reflects $\psi_{\text{off}}(t)$,

$$\langle\delta(q-\lambda t)\rangle = \int_0^\infty \psi_{\text{off}}(t)\delta(q-\lambda t)\,dt = \frac{1}{\lambda}\psi_{\text{off}}\left(\frac{q}{\lambda}\right) = \frac{\kappa_{\text{off}}e^{-\kappa_{\text{off}}q/\lambda}}{\lambda}. \tag{5.13}$$

Taking Eq. (4.9), changing some notation, and averaging over q, the probability distribution of u from a bound myosin minifilament is

$$\begin{aligned}p_{\text{on}}(u) &= \frac{3\kappa_{\text{off}}}{8\pi\lambda(R^3-a^3)u^{9/2}}\int_0^\infty\int_0^\infty e^{-\kappa_{\text{off}}q/\lambda}g(\Omega)\left[\frac{q\Omega}{16\pi\mu(1-\nu)}\right]^{3/2} \\ &\quad\times\Theta\left(u-\frac{q\Omega}{16\pi\mu(1-\nu)R^2}\right)\Theta\left(\frac{q\Omega}{16\pi\mu(1-\nu)a^2}-u\right)dqd\Omega \\ &= \frac{3\kappa_{\text{off}}}{8\pi\lambda(R^3-a^3)u^{9/2}} \\ &\quad\times\int_0^\infty\int_{16\pi\mu(1-\nu)a^2u/\Omega}^{16\pi\mu(1-\nu)R^2u/\Omega} e^{-\kappa_{\text{off}}q/\lambda}g(\Omega)\left[\frac{q\Omega}{16\pi\mu(1-\nu)}\right]^{3/2}dqd\Omega \\ &= \frac{3}{8\pi(R^3-a^3)u^{9/2}}\int_0^\infty g(\Omega)\left[\frac{\lambda\Omega}{16\pi\mu(1-\nu)\kappa_{\text{off}}}\right]^{3/2} \\ &\quad\times\left[\Gamma\left(\frac{5}{2},\frac{16\pi\mu(1-\nu)\kappa_{\text{off}}a^2u}{\lambda\Omega}\right)-\Gamma\left(\frac{5}{2},\frac{16\pi\mu(1-\nu)\kappa_{\text{off}}R^2u}{\lambda\Omega}\right)\right]d\Omega,\end{aligned} \tag{5.14}$$

where the incomplete gamma function is

$$\Gamma(1+\alpha,x) = \int_x^\infty \xi^\alpha e^{-\xi}\,d\xi. \tag{5.15}$$

Similarly, if we average over q with effective cutoffs $\widetilde{u}_{\min} = q\widetilde{\Omega}_{\min}/[16\pi\mu(1-\nu)R^2]$ and $\widetilde{u}_{\max} = q\widetilde{\Omega}_{\max}/[16\pi\mu(1-\nu)a^2]$ in Eq. (4.40), then

$$\begin{aligned}\widetilde{p}_{\text{on}}(u) &= \frac{3}{8\pi(R^3-a^3)u^{9/2}}\left[\frac{\lambda\widetilde{\Omega}_{\min}}{16\pi\mu(1-\nu)\kappa_{\text{off}}}\right]^{3/2} \\ &\quad\times\left[\Gamma\left(\frac{5}{2},\frac{16\pi\mu(1-\nu)\kappa_{\text{off}}a^2u}{\lambda\widetilde{\Omega}_{\max}}\right)-\Gamma\left(\frac{5}{2},\frac{16\pi\mu(1-\nu)\kappa_{\text{off}}R^2u}{\lambda\widetilde{\Omega}_{\min}}\right)\right].\end{aligned} \tag{5.16}$$

The probability distribution of u from an unbound myosin minifilament is

$$p_{\text{off}}(u) = \widetilde{p}_{\text{off}}(u) = \frac{\delta(u)}{4\pi u^2}, \tag{5.17}$$

expressing that there is no displacement at all.

With $\widetilde{p}_{\text{on}}(u)$, it is easy to see how the exponential distribution of q affects the probability distribution of u. For $a \ll R$,

$$\Gamma\left(\frac{5}{2}, \frac{16\pi\mu(1-\nu)\kappa_{\text{off}}R^2u}{\lambda\widetilde{\Omega}_{\text{min}}}\right) \simeq 0 \tag{5.18}$$

and

$$\widetilde{p}_{\text{on}}(u) \simeq \frac{3}{8\pi R^3 u^{9/2}}\left[\frac{\lambda\widetilde{\Omega}_{\text{min}}}{16\pi\mu(1-\nu)\kappa_{\text{off}}}\right]^{3/2}\Gamma\left(\frac{5}{2}, \frac{16\pi\mu(1-\nu)\kappa_{\text{off}}a^2u}{\lambda\widetilde{\Omega}_{\text{max}}}\right). \tag{5.19}$$

At small, but nonzero, u,

$$\Gamma\left(\frac{5}{2}, \frac{16\pi\mu(1-\nu)\kappa_{\text{off}}a^2u}{\lambda\widetilde{\Omega}_{\text{max}}}\right) \simeq \Gamma\left(\frac{5}{2}\right) = \frac{3\pi^{1/2}}{4}, \tag{5.20}$$

so $\widetilde{p}_{\text{on}}(u)$ is a power-law,

$$\widetilde{p}_{\text{on}}(u) \simeq \frac{9}{32\pi^{1/2}R^3u^{9/2}}\left[\frac{\lambda\widetilde{\Omega}_{\text{min}}}{16\pi\mu(1-\nu)\kappa_{\text{off}}}\right]^{3/2}. \tag{5.21}$$

At large u,

$$\begin{aligned}&\Gamma\left(\frac{5}{2}, \frac{16\pi\mu(1-\nu)\kappa_{\text{off}}a^2u}{\lambda\widetilde{\Omega}_{\text{max}}}\right)\\ &\quad\simeq \left[\frac{16\pi\mu(1-\nu)\kappa_{\text{off}}a^2u}{\lambda\widetilde{\Omega}_{\text{max}}}\right]^{3/2} e^{-16\pi\mu(1-\nu)\kappa_{\text{off}}a^2u/(\lambda\widetilde{\Omega}_{\text{max}})},\end{aligned} \tag{5.22}$$

so $\widetilde{p}_{\text{on}}(u)$ is an exponential,

$$\widetilde{p}_{\text{on}}(u) \simeq \frac{3}{8\pi}\left(\frac{\widetilde{\Omega}_{\text{min}}}{\widetilde{\Omega}_{\text{max}}}\right)^{3/2}\left(\frac{a}{Ru}\right)^3 e^{-16\pi\mu(1-\nu)\kappa_{\text{off}}a^2u/(\lambda\widetilde{\Omega}_{\text{max}})}. \tag{5.23}$$

This means averaging over q introduces a much smoother cutoff, specifically an exponential cutoff, to the probability distribution of u. Nevertheless, a broad power-law remains as an intermediate part.

5.3.2 The thermodynamic limit

As we did in Chapter 4, we wish to take $N \to \infty$ and $R \to \infty$ at a fixed concentration $\Phi = 3N/(4\pi R^3)$. We need the probability distribution of u due to a myosin minifilament without knowing if it is bound or unbound. This is just

$$p(u) = \frac{\kappa_{\text{on}}}{\kappa_{\text{on}} + \kappa_{\text{off}}} p_{\text{on}}(u) + \frac{\kappa_{\text{off}}}{\kappa_{\text{on}} + \kappa_{\text{off}}} p_{\text{off}}(u), \tag{5.24}$$

which has the Fourier transform

$$p(k) = \frac{\kappa_{\text{on}}}{\kappa_{\text{on}} + \kappa_{\text{off}}} p_{\text{on}}(k) + \frac{\kappa_{\text{off}}}{\kappa_{\text{on}} + \kappa_{\text{off}}} p_{\text{off}}(k). \tag{5.25}$$

It is not required to immediately evaluate the integral over q in Eq. (5.14). Starting from $p_{\text{on}}(u)$ as a double integral over q and Ω, we repeat what led us to Eq. (4.31) and then integrate over q. After doing so, we find

$$p_{\text{on}}(k) \simeq 1 + \left(\frac{a}{R}\right)^3 \times \left[1 - \int_0^\infty g(\Omega)\, {}_3F_2\left(\frac{1}{2}, 1, -\frac{3}{4}; \frac{3}{2}, \frac{1}{4}; -\left(\frac{\lambda \Omega k}{16\pi\mu(1-\nu)\kappa_{\text{off}} a^n}\right)^2\right) d\Omega\right], \tag{5.26}$$

where

$$\frac{\kappa_{\text{off}}}{\lambda} \int_0^\infty e^{-\kappa_{\text{off}} q/\lambda}\, {}_1F_2\left(-\frac{\alpha}{2}; \frac{d}{2}, 1 - \frac{\alpha}{2}; -\left(\frac{q\Omega k}{32\pi\mu(1-\nu)a^n}\right)^2\right) dq = {}_3F_2\left(\frac{1}{2}, 1, -\frac{\alpha}{2}; \frac{d}{2}, 1 - \frac{\alpha}{2}; -\left(\frac{\lambda\Omega k}{16\pi\mu(1-\nu)\kappa_{\text{off}} a^n}\right)^2\right). \tag{5.27}$$

Of course, we also have

$$p_{\text{off}}(k) = 1, \tag{5.28}$$

just the Fourier transform of a Dirac delta function.

Inserting Eqs. (5.26) and (5.28) into Eq. (5.25) gives

$$p(k) \simeq 1 + \frac{\kappa_{\text{on}}}{\kappa_{\text{on}} + \kappa_{\text{off}}} \left(\frac{a}{R}\right)^3 \times \left[1 - \int_0^\infty g(\Omega)\, {}_3F_2\left(\frac{1}{2}, 1, -\frac{3}{4}; \frac{3}{2}, \frac{1}{4}; -\left(\frac{\lambda \Omega k}{16\pi\mu(1-\nu)\kappa_{\text{off}} a^2}\right)^2\right) d\Omega\right]. \tag{5.29}$$

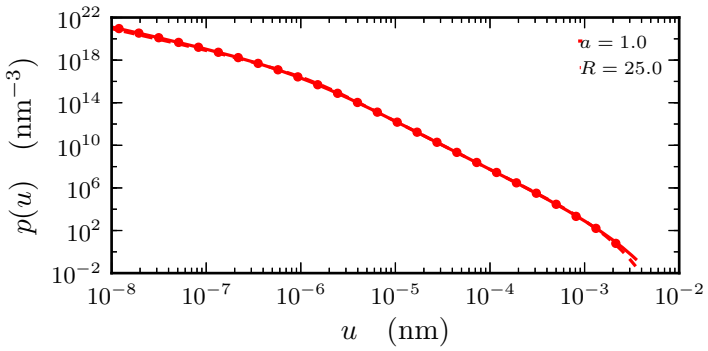

Fig. 5.6: The exact probability distribution $p(u)$, and its effective counterpart $\widetilde{p}(u)$, for a single myosin minifilament. The solid curve is the exact expression, Eq. (5.14) after numerically averaging, the dashed curve is the effective expression, Eq. (5.16), and the symbols are the simulation data.

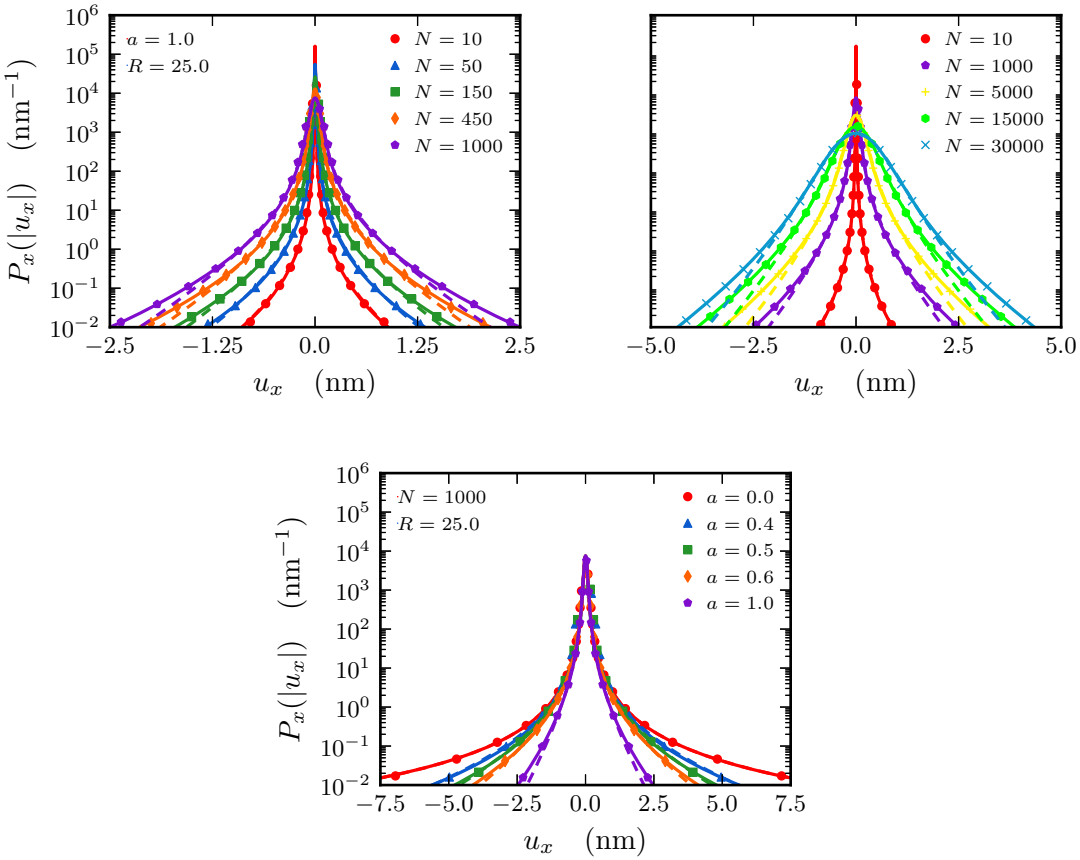

Fig. 5.7: The exact marginal probability distribution $P_x(|u_x|)$, and its effective counterpart $\widetilde{P}_x(|u_x|)$, for many myosin minifilaments. The solid curves are the exact expressions, from numerically averaging Eq. (5.30), the dashed curves are the effective expressions, from Eq. (5.31), and the symbols are the simulation data.

For many myosin minifilaments, the probability distribution of a displacement u, in the thermodynamic limit, is

$$\begin{aligned} P(k) = &\lim_{N\to\infty, R\to\infty} \left\{ 1 + \frac{\kappa_{\text{on}}}{\kappa_{\text{on}} + \kappa_{\text{off}}} \left(\frac{a}{R} \right)^3 \right. \\ &\left. \times \left[1 - \int_0^\infty g(\Omega)\, {}_3F_2\left(\frac{1}{2}, 1, -\frac{3}{4}; \frac{3}{2}, \frac{1}{4}; -\left(\frac{\lambda \Omega k}{16\pi\mu(1-\nu)\kappa_{\text{off}} a^2} \right)^2 \right) d\Omega \right] \right\}^N \\ = &\exp\left\{ \frac{4\pi a^3 \Phi_{\text{on}}}{3} \right. \\ &\left. \times \left[1 - \int_0^\infty g(\Omega)\, {}_3F_2\left(\frac{1}{2}, 1, -\frac{3}{4}; \frac{3}{2}, \frac{1}{4}; -\left(\frac{\lambda \Omega k}{16\pi\mu(1-\nu)\kappa_{\text{off}} a^2} \right)^2 \right) d\Omega \right] \right\}. \end{aligned} \tag{5.30}$$

We defined $\Phi_{\text{on}} = \kappa_{\text{on}}\Phi/(\kappa_{\text{on}} + \kappa_{\text{off}})$ as the concentration of bound myosin minifilaments. In the case of $\widetilde{u}_{\text{min}}$ and $\widetilde{u}_{\text{max}}$, the probability distribution is

$$\begin{aligned} \widetilde{P}(k) = &\exp\left\{ \left(\frac{\widetilde{\Omega}_{\text{min}}}{\widetilde{\Omega}_{\text{max}}} \right)^{3/2} \frac{4\pi a^3 \Phi_{\text{on}}}{3} \right. \\ &\left. \times \left[1 - {}_3F_2\left(\frac{1}{2}, 1, -\frac{3}{4}; \frac{3}{2}, \frac{1}{4}; -\left(\frac{\lambda \widetilde{\Omega}_{\text{max}} k}{16\pi\mu(1-\nu)\kappa_{\text{off}} a^2} \right)^2 \right) \right] \right\}. \end{aligned} \tag{5.31}$$

Using the numerical methods explained in Chapter 4, we compare $p(u)$, $P_x(|u_x|)$, and $\widetilde{P}_x(|u_x|)$ to simulation data in Figs. 5.6 and 5.7. We set $\mu = 10$ Pa, $\nu = 1/4$, $\lambda = 1$ pN μm s^{-1}, and $\kappa_{\text{on}} = \kappa_{\text{off}} = 10$ s^{-1}. These values are, at best, a rough estimate of those for an actual network with myosins [123].

5.4 Discussion

The myosin family of motor proteins is the workhorse of eukaryotic cells. As we said earlier, myosin II helps to stick, move, and split them. Many *in vitro* experiments have a concentration of myosin around 150 nM [120, 46, 115], meaning the concentration of myosin minifilaments, as a number fraction, is $\Phi \sim 0.01\ \mu\text{m}^{-3}$. Perhaps small, it is not negligible. Since a myosin minifilament drives actin while bound to it, a reconstituted network containing myosin and ATP is another example of active matter. Although the concentration of myosin may be different in a cell, the idea remains the same.

Starting with a simple model for myosin II in actin, we explained why the probability distributions of a tracer displacement measured in Ref. [115] are not Gaussian distributions. Once again, the answer is an ultraslow convergence, from truncated power-laws, to the Gaussian distribution of the central limit theorem. We extended our derivation from Chapter 4 to include the binding, and unbinding, of a myosin minifilament to, and from, actin. This smoothed the cutoff for the probability distribution of u. In the thermodynamic limit, $P(k)$ and $\widetilde{P}(k)$ clearly depend on λ, $\kappa_{\rm on}$, and $\kappa_{\rm off}$. The values of these parameters are not yet known. Neither are the values of μ or ν, which depend on $\Phi_{\rm on}$. To complicate things further, $\Phi_{\rm on}$ depends on the concentration of ATP. Given Eqs. (5.30) or (5.31), it may be possible to fit experimental data to extract values for at least some of these parameters. This is not much different from how Jean Perrin estimated Avogadro's number by applying the Stokes-Einstein relation to diffusing granules [75].

While it is possible to measure an instantaneous displacement $\mathbf{u}$, it is much easier to get the difference $\Delta\mathbf{u}(t) = \mathbf{u}(t) - \mathbf{u}(0)$ in microrheology. This is what was measured in Ref. [115]. Both $\mathbf{u}(t)$ and its initial value $\mathbf{u}(0)$ are described by $P(u)$, but $\Delta\mathbf{u}(t)$ is time-dependent with correlations that reflect $q(t)$, $\psi_{\rm on}(t)$, and $\psi_{\rm off}(t)$. We now deliver the steady state mentioned in the title of this chapter. Let $P_\Delta(u,t)$ be the probability distribution of $\Delta\mathbf{u}(t)$. It has the Fourier transform

$$P_\Delta(k,t) = \langle e^{i\mathbf{k}\cdot\Delta\mathbf{u}(t)}\rangle = \langle e^{i\mathbf{k}\cdot(\mathbf{u}(t)-\mathbf{u}(0))}\rangle \simeq \langle e^{i\mathbf{k}\cdot\mathbf{u}(t)}\rangle\langle e^{-i\mathbf{k}\cdot\mathbf{u}(0)}\rangle, \tag{5.32}$$

where the approximation is for long t. The steady state is $\lim_{t\to\infty} P_\Delta(k,t) = P(k)^2$ or, using effective cutoffs, $\lim_{t\to\infty} P_\Delta(k,t) \approx \widetilde{P}(k)^2$. In fact, the probability distribution

$$\lim_{t\to\infty} P_\Delta(k,t) \approx \exp\left\{\left(\frac{\widetilde{\Omega}_{\rm min}}{\widetilde{\Omega}_{\rm max}}\right)^{3/2}\frac{8\pi a^3\Phi_{\rm on}}{3} \times\left[1 - {}_3F_2\left(\frac{1}{2},1,-\frac{3}{4};\frac{3}{2},\frac{1}{4};-\left(\frac{\lambda\widetilde{\Omega}_{\rm max}k}{16\pi\mu(1-\nu)\kappa_{\rm off}a^2}\right)^2\right)\right]\right\} \tag{5.33}$$

has been matched against data from experiments performed in the group of Daisuke Mizuno. A detailed analysis is still underway.

Of course, actin and myosin is not the only recipe for an active suspension of molecular motors. In a feat of biological engineering, self-assembling DNA has recently been used to create a network of stiff tubes and flexible linkers [124]. The motor FtsK50C, which is derived from the bacterial protein FtsK, drives the network as it proceeds along DNA. Measurements similar to Ref. [115] are reported there, indicating that Eqs. (5.30) and (5.31) may be rather general.

Chapter 6

Conclusions

For over a century now, statistical physics has been a fundamental part of how we view the world. It has grown beyond the kinetic theory of gases to become a suite of tools for complex systems. This is especially apparent in chemistry and biology, where the motion of molecules and microorganisms is governed by fluctuations.

In Chapter 1, we discussed how active matter is a description for certain kinds of life, as well as imitations of it. There is a wide range of self-propelled particles that share many properties, although they may be superficially different. A swimming microorganism feeding on nutrients obeys similar physics as a phoretic colloid driven by chemicals. Each family of molecular motors, like dynein, kinesin, or myosin, operates distinctly, but they all generate stress once attached to the cytoskeleton or a reconstituted network. The characteristics shared across these systems encourage us to employ generic models. So far, there is little understanding of fluctuations in these systems.

We reviewed the physics of active suspensions during Chapter 2. At the microscale, the nonlinear equations of both fluid and solid mechanics each reduce to linear equations, namely the Stokes and Navier equations. These equations are often used to model activity, like we did. By its very definition, an active particle is able to propel itself. A physical consequence is that it is usually force-free. This property of an active particle is what causes non-Gaussian fluctuations in active suspensions,

something we identified and investigated throughout Chapters 3, 4, and 5.

The classical picture of Brownian motion suggests a colloid is incessantly bombarded with the surrounding molecules of the fluid. This leads to a random walk, described by the Langevin equation and, correspondingly, the Fokker-Planck equation. An appealing view is that a suspension of swimming microorganisms is an effective thermal bath, where each interaction between a tracer and a swimmer is analogous to a random kick. We put this idea to rest in Chapter 3. Except at high concentrations, the fluctuations in a suspension of swimmers should not be thought of as Gaussian. Rather than Brownian motion, a tracer actually undergoes something much closer to a Lévy flight, in which long steps replace compact exploration.

We proposed a phenomological model for the velocity fluctuations in a suspension of swimmers by tempering a Lévy stable distribution. Analytically, we matched the parameters in the phenomological distribution to the second and fourth velocity moments from the microscopic fields. This agreed well with stochastic simulations of swimmer suspensions, especially for the three-dimensional velocity distributions. It is interesting this succeeded because the exact probability distribution, which we derived in Chapter 4, is expressed quite differently in the Fourier domain. As the velocity fluctuations are non-Gaussian, the probability distribution for a tracer displacement is also non-Gaussian. Neglecting correlations, we proposed a model for that too.

With Chapter 4, we went beyond the phenomological model of Chapter 3 by deriving the exact probability distribution for the fluctuations due to a fixed concentration of random sources, each of which corresponds to a short-range field. This is actually a problem from statistical physics that has appeared again and again. Using the tracer radius as a cutoff, we solved it rather generally in any number of dimensions, yielding a probability distribution that exhibits complex shapes and behaviors. At large concentrations, there are near-exponential tails hidden in the probability distribution. These tails are universal to power-law fields that are short-ranged.

Aside from microorganisms swimming in a fluid, another example of an active suspension is molecular motors in a reconsituted network. We considered this in Chapter 5 by extending our derivation from Chapter 4. We predicted a non-Gaussian steady state for the system, which can be measured experimentally. This makes it possible to determine values for kinetic parameters that remain unknown.

So, what remains to be done? This thesis connected together active suspensions and non-Gaussian fluctuations. There are ways to extend our results in either field.

Our focus was on active suspensions in the dilute limit. For this case, the probability distribution from Eq. (4.32), and its effective counterpart from Eq. (4.41), should be very close to any measured data. But, as the concentration Φ increases, the assumption that it is constant becomes less valid. Remember, from Chapter 1, that dense suspensions form all sorts of patterns due to interacting active particles. It may be possible to use our probability distributions for dense suspensions by interpreting Φ as a local concentration that is itself random, then averaging over it. The probability distribution of this Φ can be determined from experiments, by tracking an entire population of active particles, or simulations, using field theories or microscopic models.

Although we found the exact probability distribution of the fluctuations in a dilute active suspension, we achieved less for the time-dependent probability distribution of a displacement. For swimming microorganisms, we gave a phenomenological model that eventually crosses over to a Gaussian distribution as $t \to \infty$. For molecular motors, we showed there is a non-Gaussian steady state as $t \to \infty$. Such very different behaviors at long times indicate that the correlations of an active suspension need to be carefully considered as they reflect the microscopic dynamics. This contrasts with the probability distribution of fluctuations, whose form is almost identical in both cases.

More broadly, the mathematical machinery from Chapter 4 also can be applied

to continuous random walks. Fractional diffusion equations are a popular description for scale-free random walks, for which each waiting time or step length is drawn from a heavy-tailed distribution [71, 72]. Aside from modifying a fractional diffusion equation, like we did in Chapter 3, there are no models for random walks corresponding to truncated or tempered power-law distributions. This seems counterintuitive, as these random walks are the physically relevant cases. Consider something like a truncated Lévy flight in d dimensions, where each step length is drawn from the truncated power-law distribution

$$p(r) = \Gamma\left(\frac{d}{2}\right) \frac{\alpha (r_{\min} r_{\max})^{\alpha}}{2\pi^{d/2}(r_{\max}^{\alpha} - r_{\min}^{\alpha}) r^{d+\alpha}} \Theta(r - r_{\min}) \Theta(r_{\max} - r). \tag{6.1}$$

Note the analogy with Eq. (4.40). After N steps, the displacement in the random walk is described by the characteristic function

$$P_N(k) \simeq \exp\left\{ N \left(\frac{r_{\min}}{r_{\max}}\right)^{\alpha} \times \left[1 - {}_1F_2\left(-\frac{\alpha}{2}; \frac{d}{2}, 1 - \frac{\alpha}{2}; -\left(\frac{r_{\max} k}{2}\right)^2 \right) \right] \right\} \quad (\alpha < 2). \tag{6.2}$$

For a waiting time distributed according to a truncated power-law, a similar probability distribution can be derived in the Laplace domain. Models like these may help explain non-Gaussian probability distributions that have been measured experimentally in various contexts, like those of Ref. [125]. It has been claimed that "exponential" tails are a signature of non-Gaussian diffusion [126]. Are these tails just the near-exponential tails corresponding to a sum of truncated power-law random variables?

The lack of a general theory for correlated non-Gaussian noise brings us to an open problem that may be very important. For correlated Gaussian noise, it is possible to derive a Fokker-Planck equation precisely because we know its characteristic functional, namely Eq. (2.31). If we want to do something similar in the non-Gaussian case, then we need to at least approximate its underlying characteristic functional.

Let $\zeta(t)$ be some non-Gaussian noise. Suppose we know its probability distribution $P(\zeta)$, which is the same at any instant in time, and its correlation function $\langle\zeta(t)\zeta(t')\rangle$. Can we glue together $P(\zeta)$ and $\langle\zeta(t)\zeta(t')\rangle$ to make an effective characteristic functional whose instantaneous distribution and correlation function are those supplied?

Finally, we close with the most important equation in this thesis,

$$\frac{\partial}{\partial t}P(\mathbf{r},t) \neq D\nabla^2 P(\mathbf{r},t). \tag{6.3}$$

The Fokker-Planck equation that models normal diffusion fails in a lot of common situations. Some new ideas are needed.

Appendix A

Generalized Hypergeometric Functions

Hypergeometric functions have a long history [127], which can be traced all the way back to Euler. The first hypergeometric function to be studied was the function $F(a, b; c; z)$ by Gauss. It is sometimes called "the" hypergeometric function, derived as the series solution to "the" hypergeometric equation,

$$z(1-z)\frac{d^2}{dz^2}f(z) + [c - (a+b+1)z]\frac{d}{dz}f(z) - abf(z) = 0, \tag{A.1}$$

assuming c is not a nonpositive integer.

The generalized hypergeometric function ${}_pF_q(a_1, \ldots, a_p; b_1, \ldots, b_q; z)$ is given by a formal power series,

$${}_pF_q(a_1, \ldots, a_p; b_1, \ldots, b_q; z) = \sum_{n=0}^{\infty} \frac{(a_1)_n \cdots (a_p)_n}{(b_1)_n \cdots (b_q)_n} \frac{z^n}{n!}, \tag{A.2}$$

where $(\alpha)_n$ is the Pochhammer symbol (also known as the rising factorial),

$$(\alpha)_n = \frac{\Gamma(\alpha + n)}{\Gamma(\alpha)}. \tag{A.3}$$

We suppose that none of the parameters $b_1, \ldots, b_q$ is a nonpositive integer, a requirement for the definition of ${}_pF_q(a_1, \ldots, a_p; b_1, \ldots, b_q; z)$ to make sense. If any of the parameters $a_1, \ldots, a_p$ is a nonpositive integer, then ${}_pF_q(a_1, \ldots, a_p; b_1, \ldots, b_q; z)$ becomes just a polynomial. Both a_i and b_j can be removed should $a_i = b_j$, leaving us with $p-1$ parameters $a_1, \ldots, a_{i-1}, a_{i+1}, \ldots, a_p$ and $q-1$ parameters $b_1, \ldots, b_{j-1}, b_{j+1}, \ldots, b_q$.

The series from Eq. (A.2) is a hypergeometric series, meaning each ratio of consecutive terms is a rational function of n,

$$\frac{(a_1)_{n+1}\cdots(a_p)_{n+1}(b_1)_n\cdots(b_q)_n}{(a_1)_n\cdots(a_p)_n(b_1)_{n+1}\cdots(b_q)_{n+1}}\frac{n!z^{n+1}}{(n+1)!z^n}=\frac{(a_1+n)\cdots(a_p+n)}{(b_1+n)\cdots(b_q+n)}\frac{z}{n+1}. \tag{A.4}$$

It converges for all finite z if $p\leq q$ and for $|z|<1$ if $p=q+1$, or diverges for all nonzero z if $p\geq q+2$. More information about generalized hypergeometric functions, beyond the following, is provided in Refs. [127, 128, 129, 130].

The nth derivative is

$$\begin{aligned}&\frac{d^n}{dz^n}{}_pF_q(a_1,\ldots,a_p;b_1,\ldots,b_q;z)\\&\quad=\frac{(a_1)_n\cdots(a_p)_n}{(b_1)_n\cdots(b_q)_n}{}_pF_q(a_1+n,\ldots,a_p+n;b_1+n,\ldots,b_q+n;z),\end{aligned} \tag{A.5}$$

which is a special case of the formula

$$\begin{aligned}&\frac{d^n}{dz^n}(z^\alpha{}_pF_q(a_1,\ldots,a_p;b_1,\ldots,b_q;z))\\&\quad=(\alpha-n+1)z^{\alpha-n}{}_{p+1}F_{q+1}(\alpha+1,a_1,\ldots,a_p;\alpha+1,b_1,\ldots,b_q;z).\end{aligned} \tag{A.6}$$

It satisfies the differential identities

$$\begin{aligned}&\left(z\frac{d}{dz}+a_i\right){}_pF_q(a_1,\ldots,a_p;b_1,\ldots,b_q;z)\\&\quad=a_i\,{}_pF_q(a_1,\ldots,a_i+1,\ldots,a_p;b_1,\ldots,b_q;z),\end{aligned} \tag{A.7a}$$

$$\begin{aligned}&\left(z\frac{d}{dz}+b_i-1\right){}_pF_q(a_1,\ldots,a_p;b_1,\ldots,b_q;z)\\&\quad=b_i\,{}_pF_q(a_1,\ldots,a_p;b_1,\ldots,b_i-1,\ldots,b_q;z).\end{aligned} \tag{A.7b}$$

Combining these leads to the differential equation,

$$\begin{aligned}&z\left[\left(z\frac{d}{dz}+a_1\right)\cdots\left(z\frac{d}{dz}+a_p\right)\right]f(z)\\&\quad=z\frac{d}{dz}\left[\left(z\frac{d}{dz}+b_1-1\right)\cdots\left(z\frac{d}{dz}+b_q-1\right)\right]f(z),\end{aligned} \tag{A.8}$$

for which ${}_pF_q(a_1,\ldots,a_p;b_1,\ldots,b_q;z)$ is the solution.

Integrating a generalized hypergeometric function gives, up to a constant, another generalized hypergeometric function,

$$\int {}_pF_q(a_1,\ldots,a_p;b_1,\ldots,b_q;z)\,dz$$
$$= \frac{(b_1-1)\cdots(b_q-1)}{(a_1-1)\cdots(a_p-1)}{}_pF_q(a_1-1,\ldots,a_p-1;b_1-1,\ldots,b_q-1;z). \tag{A.9}$$

We can easily integrate the product of a power and a generalized hypergeometric function, if $\alpha \geq 1$,

$$\int z^{\alpha-1}{}_pF_q(a_1,\ldots,a_p;b_1,\ldots,b_q;z)\,dz$$
$$= \frac{z^\alpha}{\alpha}{}_{p+1}F_{q+1}(\alpha,a_1,\ldots,a_p;\alpha+1,b_1,\ldots,b_q;z). \tag{A.10}$$

Appendix B

The Fourier Transform in d Dimensions

Given a function $f(\mathbf{r})$ of a vector $\mathbf{r}$ in d dimensions, we define its (forward) Fourier transform by

$$f(\mathbf{k}) = \int e^{i\mathbf{k}\cdot\mathbf{r}} f(\mathbf{r})\, d^d r. \tag{B.1}$$

This has the inverse Fourier transform

$$f(\mathbf{r}) = \frac{1}{(2\pi)^d} \int e^{-i\mathbf{k}\cdot\mathbf{r}} f(\mathbf{k})\, d^d k. \tag{B.2}$$

We always denote the Fourier transform $f(\mathbf{k})$ of a function $f(\mathbf{r})$ by explicit dependence on the argument.

If the function has radial symmetry, meaning that we write it as $f(r)$ with $r = |\mathbf{r}|$, the angular integrals from Eqs. (B.1) or (B.2) can be evaluated immediately. We transform to hyperspherical coordinates,

$$\mathbf{r} = \begin{pmatrix} r\cos\phi_1 \\ r\sin\phi_1\cos\phi_2 \\ r\sin\phi_1\sin\phi_2\cos\phi_3 \\ \vdots \\ r\sin\phi_1\cdots\sin\phi_{d-3}\cos\phi_{d-2} \\ r\sin\phi_1\cdots\sin\phi_{d-2}\cos\theta \\ r\sin\phi_1\cdots\sin\phi_{d-2}\sin\theta \end{pmatrix}, \tag{B.3}$$

for which the volume element is

$$d^d r = r^{d-1}\sin^{d-2}\phi_1 \sin^{d-3}\phi_2 \cdots \sin\phi_{d-2}\, dr d\theta d\phi_1 d\phi_2 \cdots d\phi_{d-2}. \tag{B.4}$$

The angle θ lies between 0 and 2π, whereas every other angle ranges from 0 to π. Since the Fourier transform of a radially symmetric function depends only on $k = |\mathbf{k}|$, it is permissible to just choose $\mathbf{k} = k\hat{\mathbf{r}}_1$. Then Eq. (B.1) becomes

$$f(k) = \int e^{ikr\cos\phi_1} \times f(r) r^{d-1} \sin^{d-2}\phi_1 \sin^{d-3}\phi_2 \cdots \sin\phi_{d-2}\, dr d\theta d\phi_1 d\phi_2 \cdots d\phi_{d-2}. \tag{B.5}$$

Assuming $d > 1$, we first perform the integral over ϕ_1,

$$\int_0^\pi e^{ikr\cos\phi_1} \sin^{d-2}\phi_1\, d\phi_1 = \pi^{1/2}\Gamma\left(\frac{d-1}{2}\right)\left(\frac{2}{kr}\right)^{d/2-1} J_{d/2-1}(kr), \tag{B.6}$$

where $J_\nu(z)$ is a Bessel function of the first kind. For the remaining angles, we have

$$\begin{aligned}\int \sin^{d-3}\phi_2 \cdots \sin\phi_{d-2}\, d\theta d\phi_2 \cdots d\phi_{d-2} &= S_d \left(\int_0^\pi \sin^{d-2}\phi_1\, d\phi_1\right)^{-1} \\ &= \Gamma\left(\frac{d}{2}\right)\Gamma\left(\frac{d-1}{2}\right)^{-1}\frac{S_d}{\pi^{1/2}}.\end{aligned} \tag{B.7}$$

The constant S_d is the solid angle subtended by a hypersphere,

$$S_d = \int \sin^{d-2}\phi_1 \sin^{d-3}\phi_2 \cdots \sin\phi_{d-2}\, d\theta d\phi_1 d\phi_2 \cdots d\phi_{d-2} = 2\pi^{d/2}\Gamma\left(\frac{d}{2}\right)^{-1}, \tag{B.8}$$

which typically appears as part of the volume V_d of a hypersphere with radius R,

$$V_d = S_d \int_0^R r^{d-1}\, dr = \frac{S_d R^d}{d}. \tag{B.9}$$

Using a generalized hypergeometric function ${}_pF_q(a_1, \ldots, a_p; b_1, \ldots, b_q; z)$ for brevity, the result can be put together as

$$\begin{aligned} f(k) &= \Gamma\left(\frac{d}{2}\right) S_d \int_0^\infty \left(\frac{2}{kr}\right)^{d/2-1} J_{d/2-1}(kr) f(r) r^{d-1}\, dr \\ &= S_d \int_0^\infty {}_0F_1\left(;\frac{d}{2};-\left(\frac{kr}{2}\right)^2\right) f(r) r^{d-1}\, dr. \end{aligned} \tag{B.10}$$

The inverse Fourier transform has the analogous formula

$$f(r) = \frac{S_d}{(2\pi)^d}\int_0^\infty {}_0F_1\left(;\frac{d}{2};-\left(\frac{kr}{2}\right)^2\right) f(k) k^{d-1}\, dk. \tag{B.11}$$

Eq. (B.10), like its counterpart (B.11), is valid for any d. For $d = 1$, these equations correspond to a function that depends only on the absolute value of the argument.

Appendix C

Meijer G-Functions

The Meijer G-function, a very general function, is defined by the Mellin-Barnes integral

$$G_{p,q}^{m,n}\left(z \,\middle|\, \begin{matrix} a_1,\ldots,a_p \\ b_1,\ldots,b_q \end{matrix}\right) = \frac{1}{2\pi i}\int_L \frac{\Gamma(b_1-s)\cdots\Gamma(b_m-s)\Gamma(1-a_1+s)\cdots\Gamma(1-a_n+s)}{\Gamma(a_{n+1}-s)\cdots\Gamma(a_p-s)\Gamma(1-b_{m+1}+s)\cdots\Gamma(1-b_q+s)} z^s\, ds, \quad \text{(C.1)}$$

where the contour L is a line parallel to the imaginary axis that has indentations, if necessary, to avoid all poles of the integrand. It was introduced by Meijer [131, 132] to capture many special functions as limiting cases. For a detailed review of its properties, see Refs. [128, 129, 130].

We assume the parameters are such that no pole of $\Gamma(b_j - s)$ for $1 \le j \le m$ coincides with a pole of $\Gamma(1 - a_i + s)$ for $1 \le i \le n$. Or, equivalently, $a_i - b_j$ cannot be a positive integer for $1 \le i \le n$ and $1 \le j \le m$. If a parameter in $a_1, \ldots, a_n$ is equal to a parameter in $b_{m+1}, \ldots, b_q$, then both parameters are removed,

$$G_{p,q}^{m,n}\left(z \,\middle|\, \begin{matrix} a_1,\ldots,a_p \\ b_1,\ldots,b_{q-1},a_1 \end{matrix}\right) = G_{p-1,q-1}^{m,n-1}\left(z \,\middle|\, \begin{matrix} a_2,\ldots,a_p \\ b_1,\ldots,b_{q-1} \end{matrix}\right). \quad \text{(C.2)}$$

A similar relation holds if a parameter in $a_{n+1}, \ldots, a_p$ is equal to a parameter in $b_1, \ldots, b_m$. By a change of variable in the integral from Eq. (C.1), we can derive the identities

$$G_{p,q}^{m,n}\left(z \,\middle|\, \begin{matrix} a_1,\ldots,a_p \\ b_1,\ldots,b_q \end{matrix}\right) = G_{q,p}^{n,m}\left(\frac{1}{z} \,\middle|\, \begin{matrix} 1-b_1,\ldots,1-b_q \\ 1-a_1,\ldots,1-a_p \end{matrix}\right) \quad \text{(C.3)}$$

and

$$z^{\alpha} G_{p,q}^{m,n}\left(z \,\middle|\, \begin{matrix} a_1, \ldots, a_p \\ b_1, \ldots, b_q \end{matrix} \right) = G_{p,q}^{m,n}\left(z \,\middle|\, \begin{matrix} a_1 + \alpha, \ldots, a_p + \alpha \\ b_1 + \alpha, \ldots, b_q + \alpha \end{matrix} \right). \tag{C.4}$$

Note Eq. (C.3) lets us transform the Meijer G-function with $p > q$ into the Meijer G-function with $p < q$.

The generalized hypergeometric function can be expressed as the Meijer G-function,

$$\begin{aligned} {}_pF_q(a_1, \ldots, a_p; b_1, \ldots, b_q; z) &= \frac{\Gamma(b_1) \cdots \Gamma(b_q)}{\Gamma(a_1) \cdots \Gamma(a_p)} G_{p,q+1}^{1,p}\left(-z \,\middle|\, \begin{matrix} 1 - a_1, \ldots, 1 - a_p \\ 0, 1 - b_1, \ldots, 1 - b_q \end{matrix} \right) \\ &= \frac{\Gamma(b_1) \cdots \Gamma(b_q)}{\Gamma(a_1) \cdots \Gamma(a_p)} G_{p,q+1}^{p,1}\left(-\frac{1}{z} \,\middle|\, \begin{matrix} 1, b_1, \ldots, b_q \\ a_1, \ldots, a_p \end{matrix} \right). \end{aligned} \tag{C.5}$$

Integrating the Meijer G-function with respect to z produces

$$\begin{aligned} &\int G_{p,q}^{m,n}\left(z \,\middle|\, \begin{matrix} a_1, \ldots, a_p \\ b_1, \ldots, b_q \end{matrix} \right) dz \\ &\quad = G_{p+1,q+1}^{m,n+1}\left(z \,\middle|\, \begin{matrix} 1, a_1 + 1, \ldots, a_p + 1 \\ b_1 + 1, \ldots, b_m + 1, 0, b_{m+1} + 1, \ldots, b_q + 1 \end{matrix} \right). \end{aligned} \tag{C.6}$$

We can also integrate the product of a power-law and the Meijer G-function,

$$\begin{aligned} &\int z^{\alpha - 1} G_{p,q}^{m,n}\left(z \,\middle|\, \begin{matrix} a_1, \ldots, a_p \\ b_1, \ldots, b_q \end{matrix} \right) dz \\ &\quad = G_{p+1,q+1}^{m,n+1}\left(z \,\middle|\, \begin{matrix} 1, a_1 + \alpha, \ldots, a_p + \alpha \\ b_1 + \alpha, \ldots, b_m + \alpha, 0, b_{m+1} + \alpha, \ldots, b_q + \alpha \end{matrix} \right). \end{aligned} \tag{C.7}$$

References

[1] J. Toner, Y. Tu, and S. Ramaswamy, *Hydrodynamics and phases of flocks*, Ann. Phys. **318** (2005), 170–244.

[2] J.-F. Joanny and J. Prost, *Active gels as a description of the actin-myosin cytoskeleton*, HFSP J. **3** (2009), 94–104.

[3] S. Ramaswamy, *The mechanics and statistics of active matter*, Annu. Rev. Condens. Matter Phys. **1** (2010), 323–345.

[4] M. C. Marchetti, J.-F. Joanny, S. Ramaswamy, T. B. Liverpool, J. Prost, M. Rao, and R. A. Simha, *Soft active matter*, arXiv:1207.2929 (2012).

[5] L. D. Landau and E. M. Lifshitz, *Statistical physics*, Vol. 1, Pergamon Press, Exeter, United Kingdom, 1994.

[6] H. C. Berg and R. A. Anderson, *Bacteria swim by rotating their flagellar filaments*, Nature **245** (1973), 380–382.

[7] A. van Leeuwenhoek and C. Dobell (editor), *Anthony van Leeuwenhoek and his "little animals"*, Harcourt Brace and Company, New York, 1932.

[8] L. Turner, W. S. Ryu, and H. C. Berg, *Real-time imaging of fluorescent flagellar filaments*, J. Bacteriol. **182** (2000), 2793–2801.

[9] C. Dombrowski, L. Cisneros, S. Chatkaew, R. E. Goldstein, and J. O. Kessler, *Self-concentration and large-scale coherence in bacterial dynamics*, Phys. Rev. Lett. **93** (2004), 098103.

[10] R. E. Goldstein, M. Polin, and I. Tuval, *Emergence of synchronized beating during the regrowth of eukaryotic flagella*, Phys. Rev. Lett. **107** (2011), 148103.

[11] E. M. Purcell, *Life at low Reynolds number*, Am. J. Phys. **45** (1977), 3–1.

[12] R. Dreyfus, J. Baudry, M. L. Roper, M. Fermigier, H. A. Stone, and J. Bibette, *Microscopic artificial swimmers*, Nature **437** (2005), 862–865.

[13] A. Najafi and R. Golestanian, *Simple swimmer at low Reynolds number: three linked spheres*, Phys. Rev. E **69** (2004), 062901.

[14] M. Leoni, J. Kotar, B. Bassetti, P. Cicuta, and M. C. Lagomarsino, *A basic swimmer at low Reynolds number*, Soft Matter **5** (2009), 472–476.

[15] G. Taylor, *Analysis of the swimming of microscopic organisms*, Proc. Roy. Soc. A **209** (1951), 447–461.

[16] J. Lighthill, *Mathematical biofluiddynamics*, SIAM, Philadelphia, Pennsylvania, 1975.

[17] S. Childress, *Mechanics of swimming and flying*, Cambridge University Press, New York, 1981.

[18] L. E. Becker, S. A. Koehler, and H. A. Stone, *On self-propulsion of micro-machines at low Reynolds number: Purcell's three-linked swimmer*, J. Fluid Mech. **490** (2003), 15–35.

[19] M. Bzdega and S. A. Koehler, *How to swim in sand*, Earth and Space 2006 (Reston, Virginia), Engineering, Construction, and Operations in Challenging Environments, American Society of Civil Engineers, 2006.

[20] T. S. Yu, E. Lauga, and A. E. Hosoi, *Experimental investigations of elastic tail propulsion at low Reynolds number*, Phys. Fluids **18** (2006), 091701.

[21] A. Snezhko, M. Belkin, I. S. Aranson, and W.-K. Kwok, *Self-assembled magnetic surface swimmers*, Phys. Rev. Lett. **102** (2009), 118103.

[22] A. Ghosh and P. Fischer, *Controlled propulsion of artificial magnetic nanostructured propellers*, Nano Lett. **9** (2009), 2243–2245.

[23] W. Gao, D. Kagan, O. S. Pak, C. Clawson, S. Campuzano, E. Chuluun-Erdene, E. Fullerton, L. Zhang, E. Lauga, and J. Wang, *Cargo-towing fuel-free magnetic nanoswimmers for targeted drug delivery*, Small **8** (2011), 460–467.

[24] E. Lauga, W. R. DiLuzio, G. M. Whitesides, and H. A. Stone, *Swimming in circles: motion of bacteria near solid boundaries*, Biophys. J. **90** (2006), 400–412.

[25] H. Shum, E. A. Gaffney, and D. J. Smith, *Modelling bacterial behaviour close to a no-slip plane boundary: the influence of bacterial geometry*, Proc. R. Soc. A **466** (2010), 1725–1748.

[26] C. M. Pooley, G. P. Alexander, and J. M. Yeomans, *Hydrodynamic interaction between two swimmers at low Reynolds number*, Phys. Rev. Lett. **99** (2007), 228103.

[27] K. Drescher, K. Leptos, I. Tuval, T. Ishikawa, T. J. Pedley, and R. E. Goldstein, *Dancing Volvox: hydrodynamic bound states of swimming algae*, Phys. Rev. Lett. **102** (2009), 168101.

[28] G. J. Elfring and E. Lauga, *Hydrodynamic phase locking of swimming microorganisms*, Phys. Rev. Lett. **103** (2009), 088101.

[29] R. E. Goldstein, M. Polin, and I. Tuval, *Noise and synchronization in pairs of beating eukaryotic flagella*, Phys. Rev. Lett. **103** (2009), 168103.

[30] J. Gray, *Ciliary movement*, Cambridge University Press, Cambridge, United Kingdom, 1928.

[31] H. P. Zhang, A. Be'er, E.-L. Florin, and H. L. Swinney, *Collective motion and density fluctuations in bacterial colonies*, Proc. Natl. Acad. Sci. USA **107** (2010), 13626–13630.

[32] T. Ishikawa, N. Yoshida, H. Ueno, M. Wiedeman, Y. Imai, and T. Yamaguchi, *Energy transport in a concentrated suspension of bacteria*, Phys. Rev. Lett. **107** (2011), 028102.

[33] T. J. Pedley, N. A. Hill, and J. O. Kessler, *The growth of bioconvection patterns in a uniform suspension of gyrotactic micro-organisms*, J. Fluid Mech. **195** (1988), 223–237.

[34] J. B. Xavier, E. Martinez-Garcia, and K. R. Foster, *Social evolution of spatial patterns in bacterial biofilms: when conflict drives disorder*, Am. Nat. **174** (2009), 1–12.

[35] N. C. Darnton, L. Turner, S. Rojevsky, and H. C. Berg, *Dynamics of bacterial swarming*, Biophys. J. **98** (2010), 2082–2090.

[36] I. H. Riedel, K. Kruse, and J. Howard, *A self-organized vortex array of hydrodynamically entrained sperm cells*, Science **309** (2005), 300–303.

[37] E. Bertin, M. Droz, and G. Grégoire, *Boltzmann and hydrodynamic description for self-propelled particles*, Phys. Rev. E **74** (2006), 022101.

[38] A. Baskaran and M. C. Marchetti, *Statistical mechanics and hydrodynamics of bacterial suspensions*, Proc. Natl. Acd. Sci. USA **106** (2009), 15567–15572.

[39] J. Toner and Y. Tu, *Long-range order in a two-dimensional dynamical XY model: how birds fly together*, Phys. Rev. Lett. **75** (1995), 4326–4329.

[40] R. A. Simha and S. Ramaswamy, *Hydrodynamic fluctuations and instabilities in ordered suspensions of self-propelled particles*, Phys. Rev. Lett. **89** (2002), 058101.

[41] B. Alberts, D. Bray, J. Lewis, M. Raff, K. Roberts, and J. D. Watson, *Molecular biology of the cell*, second ed., Garland, New York, 1989.

[42] J. Howard, *Mechanics of motor proteins and the cytoskeleton*, Sinauer Associates, Sunderland, Massachusetts, 2001.

[43] J. T. Finer, R. M. Simmons, and J. A. Spudich, *Single myosin molecule mechanics: piconewton forces and nanometre steps*, Nature **368** (1994), 113–119.

[44] A. R. Bausch and K. Kroy, *A bottom-up approach to cell mechanics*, Nat. Phys. **2** (2006), 231–238.

[45] A. P. Liu and D. A. Fletcher, *Biology under construction: in vitro reconstitution of cellular function*, Nat. Rev. Mol. Cell Biol. **10** (2009), 644–650.

[46] D. Mizuno, C. Tardin, C. F. Schmidt, and F. C. MacKintosh, *Nonequilibrium mechanics of active cytoskeletal networks*, Science **315** (2007), 370–373.

[47] T. Surrey, F. Nédélec, S. Leibler, and E. Karsenti, *Physical properties determining self-organization of motors and microtubules*, Science **292** (2001), 1167–1171.

[48] P.-G. de Gennes, *Scaling concepts in polymer physics*, Cornell University Press, Ithaca, New York, 1979.

[49] T. B. Liverpool and M. C. Marchetti, *Instabilities of isotropic solutions of active polar filaments*, Phys. Rev. Lett. **90** (2003), 138102.

[50] I. S. Aranson and L. S. Tsimring, *Pattern formation of microtubules and motors: inelastic interaction of polar rods*, Phys. Rev. E **71** (2005), 050901.

[51] K. Kruse, J. F. Joanny, F. Jülicher, J. Prost, and K. Sekimoto, *Asters, vortices, and rotating spirals in active gels of polar filaments*, Phys. Rev. Lett. **92** (2004), 078101.

[52] N. Kikuchi, A. Ehrlicher, D. Koch, J. A. Käs, S. Ramaswamy, and M. Rao, *Buckling, stiffening, and negative dissipation in the dynamics of a biopolymer in an active medium*, Proc. Natl. Acad. Sci. USA **106** (2009), 19776–19779.

[53] F. J. Nédélec, T. Surrey, A. C. Maggs, and S. Leibler, *Self-organization of microtubules and motors*, Nature **389** (1997), 305–308.

[54] V. Schaller, C. Weber, C. Semmrich, E. Frey, and A. R. Bausch, *Polar patterns of driven filaments*, Nature **467** (2010), 73–77.

[55] T. Butt, T. Mufti, A. Humayun, P. B. Rosenthal, S. Khan, S. Khan, and J. E. Molloy, *Myosin motors drive long range alignment of actin filaments*, J. Biol. Chem. **285** (2010), 4964–4974.

[56] V. Schaller, C. A. Weber, B. Hammerich, E. Frey, and A. R. Bausch, *Frozen steady states in active systems*, Proc. Natl. Acad. Sci. USA **108** (2011), 19183–19188.

[57] M. Doi and S. F. Edwards, *The theory of polymer dynamics*, Oxford University Press, New York, 1998.

[58] K. Drescher, R. E. Goldstein, N. Michel, M. Polin, and I. Tuval, *Direct measurement of the flow field around swimming microorganisms*, Phys. Rev. Lett. **105** (2010), 168101.

[59] K. Drescher, J. Dunkel, L. H. Cisneros, S. Ganguly, and R. E. Goldstein, *Fluid dynamics and noise in bacterial cell-cell and cell-surface scattering*, Proc. Natl. Acad. Sci. USA **108** (2011), 10940–10945.

[60] S. Kim and S. J. Karrila, *Microhydrodynamics: principles and selected applications*, Dover Publications, Mineola, New York, 2005.

[61] N. Phan-Thien and S. Kim, *Microstructures in elastic media: principles and computational methods*, Oxford University Press, New York, 1994.

[62] W. Feller, *An introduction to probability theory and its applications*, Vol. 1 and 2, Wiley, New York, 1971.

[63] E. T. Whittaker and G. Robinson, *The calculus of observations: a treatise on numerical mathematics*, Dover Publications, New York, 1967.

[64] B. V. Gnedenko and A. N. Kolmogorov, *Limit distributions for sums of independent random variables*, Addison-Wesley, Cambridge, Massachusetts, 1954.

[65] N. G. van Kampen, *Stochastic processes in physics and chemistry*, Elsevier, Amsterdam, The Netherlands, 2006.

[66] P. Hänggi and P. Jung, *Colored noise in dynamical systems*, Adv. Chem. Phys. **89** (1995), 239–326.

[67] B. D. Hughes, *Random walks and random environments*, Vol. 1, Oxford University Press, New York, 1995.

[68] M. F. Shlesinger, G. M. Zaslavsky, and U. Frisch (eds.), *Lévy flights and related topics in physics*, Proceedings of the International Workshop (June 27-30, 1994), Berlin, Springer, 1995.

[69] H. C. Fogedby, *Langevin equations for continuous time Lévy flights*, Phys. Rev. E **50** (1994), 1657–1660.

[70] A. A. Budini and M. Cáceres, *Functional characterization of generalized Langevin equations*, J. Phys. A: Math. Gen. **37** (2004), 5959–5981.

[71] R. Metzler and J. Klafter, *The random walk's guide to anomalous diffusion: a fractional dynamics approach*, Phys. Rep. **339** (2000), 1–77.

[72] ———, *The restaurant at the end of the random walk: recent developments in the description of anomalous transport by fractional dynamics*, J. Phys. A: Math. Gen. **37** (2004), R161–R208.

[73] K. C. Leptos, J. S. Guasto, J. P. Gollub, A. I. Pesci, and R. E. Goldstein, *Dynamics of enhanced tracer diffusion in suspensions of swimming microorganisms*, Phys. Rev. Lett. **103** (2009), 198103.

[74] J. Ingenhousz, *Vermischte schriften physisch und medicinischen inhalts*, Wapler, Vienna, Austria, 1784.

[75] J. Perrin, *Mouvement Brownien et réalité moléculaire*, Ann. Chim. Phys. **18** (1909), 5–114.

[76] W. Sutherland, *A dynamical theory of diffusion for non-electrolytes and the molecular mass of albumin*, Philos. Mag. **9** (1905), 781–785.

[77] A. Einstein, *Über die von der molekularkinetischen theorie der wärme geforderten bewegung von in ruhenden flüssigkeiten suspendierten teilcehn*, Annalen der Physik und Chemie **17** (1905), 549–560.

[78] Y. Han, A. M. Alsayed, M. Nobili, J. Zhang, T. C. Lubensky, and A. G. Yodh, *Brownian motion of an ellipsoid*, Science **314** (2006), 626–630.

[79] T. Li, S. Kheifets, D. Medellin, and M. G. Raizen, *Measurement of the instantaneous velocity of a Brownian particle*, Science **328** (2010), 1673–1675.

[80] A. Sokolov, M. M. Apodacac, B. A. Grzybowskic, and I. S. Aranson, *Swimming bacteria power microscopic gears*, Proc. Natl. Acad. Sci. USA **107** (2009), 969–974.

[81] R. Di Leonardo, L. Angelani, D. Dell'Arciprete, G. Ruocco, V. Iebba, S. Schippa, M. P. Conte, F. Mecarini, F. De Angelis, and E. Di Fabrizio, *Bacterial rachet motors*, Proc. Natl. Acad. Sci. USA **107** (2010), 9541–9545.

[82] X.-L. Wu and A. Libchaber, *Particle diffusion in a quasi-two-dimensional bacterial bath*, Phys. Rev. Lett. **84** (2000), 3017–3020.

[83] D. T. N. Chen, A. W. C. Lau, L. A. Hough, M. F. Islam, M. Goulian, T. C. Lubensky, and A. G. Yodh, *Fluctuations and rheology in active bacterial suspensions*, Phys. Rev. Lett. **99** (2007), 148302.

[84] J. P. Hernandez-Ortiz, C. G. Stoltz, and M. D. Graham, *Transport and collective dynamics in suspensions of confined swimming particles*, Phys. Rev. Lett. **95** (2005), 204501.

[85] P. T. Underhill, J. P. Hernandez-Ortiz, and M. D. Graham, *Diffusion and spatial correlations in suspensions of swimming particles*, Phys. Rev. Lett. **100** (2008), 248101.

[86] I. Rushkin, V. Kantsler, and R. E. Goldstein, *Fluid velocity fluctuations in a suspension of swimming protists*, Phys. Rev. Lett. **105** (2010), 188101.

[87] E. Lauga and T. R. Powers, *The hydrodynamics of swimming microorganisms*, Rep. Prog. Phys. **72** (2009), 1–36.

[88] J. L. Anderson, *Colloid transport by interfacial forces*, Ann. Rev. Fluid Mech. **212** (1989), 155–182.

[89] J. Dunkel, V. B. Putz, I. M. Zaid, and J. M. Yeomans, *Swimmer-tracer scattering at low Reynolds number*, Soft Matter **6** (2010), 4268–4276.

[90] T. J. Pedley and J. O. Kessler, *A new continuum model for suspensions of gyrotactic microorganisms*, J. Fluid Mech. **212** (1990), 155–182.

[91] N. J. Carron, *An introduction to the passage of energetic particles through matter*, CRC Press, Boca Raton, Florida, 2007.

[92] J. S. Guasto, K. A. Johnson, and J. P. Gollub, *Oscillatory flows induced by microorganisms swimming in two-dimensions*, Phys. Rev. Lett. **105** (2010), 168101.

[93] R. N. Mantegna and H. E. Stanley, *Stochastic process with ultraslow convergence to a Gaussian: the truncated Lévy flight*, Phys. Rev. Lett. **73** (1994), 2947–2949.

[94] G. Samorodnitsky and M. S. Taqqu, *Stable non-Gaussian random processes: stochastic models with infinite variance*, Chapman & Hall, New York, 1994.

[95] B. I. Shraiman and E. D. Siggia, *Lagrangian path integrals and fluctuations in random flow*, Phys. Rev. E **49** (1994), 2912–2927.

[96] S. G. Samko, A. A. Kilbas, and O. I. Marichev, *Fractional integrals and derivatves: theory and applications*, Gordon and Breach, Amsterdam, The Netherlands, 1993.

[97] C. A. Solari, S. Ganguly, J. O. Kessler, R. E. Michod, and R. E. Goldstein, *Multicellularity and the functional interdependence of motility and molecular transport*, Proc. Natl. Acad. Sci. USA **103** (2006), 1353–1358.

[98] M. B. Short, C. A. Solari, S. Ganguly, T. R. Powers, J. O. Kessler, and R. E. Goldstein, *Flows driven by flagella of multicellular organisms enhance long-range molecular transport*, Proc. Natl. Acad. Sci. USA **103** (2006), 8315–8319.

[99] J. Holtsmark, *Über die verbreiterung von spektrallinien*, Ann. Phys. **363** (1919), 577–630.

[100] S. Chandrasekhar, *Stochastic problems in physics and astronomy*, Rev. Mod. Phys. **15** (1943), 1–89.

[101] H. Takayasu, *Stable distribution and Lévy process in fractal turbulence*, Prog. Theor. Phys. **72** (1984), 471–479.

[102] J. Jiménez, *Algebraic probability density tails in decaying isotropic two-dimensional turbulence*, J. Fluid Mech. **313** (1996), 223–240.

[103] I. A. Min, I. Mezić, and A. Leonard, *Lévy stable distributions for velocity and velocity difference in systems of vortex elements*, Phys. Fluids **8** (1996), 1169–1180.

[104] P. Cizeau and J. P. Bouchaud, *Mean field theory of dilute spin-glasses with power-law interactions*, J. Phys. A: Math. Gen. **26** (1993), L187–L193.

[105] L. Onsager, *Statistical hydrodynamics*, Nuovo Cimento Suppl. **6** (1949), 279–287.

[106] C. Goutis and G. Casella, *Explaining the saddlepoint approximation*, Amer. Stat. **53** (1999), 216–224.

[107] S. Huzurbazar, *Practical saddlepoint approximations*, Amer. Stat. **53** (1999), 225–232.

[108] P. G. Saffman, *Vortex dynamics*, Cambridge University Press, Cambridge, United Kingdom, 1995.

[109] G. Nicolis and I. Prigogine, *Self-organization in nonequilibrium systems: from dissipative structures to order through fluctuations*, Wiley, New York, 1977.

[110] T. A. Waigh, *Microrheology of complex fluids*, Rep. Prog. Phys. **68** (2005), 685–742.

[111] P. Cicuta and A. M. Donald, *Microrheology: a review of the method and applications*, Soft Matter **3** (2007), 1449–1455.

[112] F. C. MacKintosh, J. Käs, and P. A. Janmey, *Elasticity of semiflexible biopolymer networks*, Phys. Rev. Lett. **75** (1995), 4425–4428.

[113] T. Gisler and D. A. Weitz, *Scaling of the microrheology of semidilute f-actin solutions*, Phys. Rev. Lett. **82** (1999), 1606–1609.

[114] M. L. Gardel, J. H. Shin, F. C. MacKintosh, L. Mahadevan, P. Matsudaira, and D. A. Weitz, *Elastic behavior of cross-linked and bundled actin networks*, Science **304** (2004), 1301–1305.

[115] T. Toyota, D. A. Head, C. F. Schmidt, and D. Mizuno, *Non-gaussian athermal fluctuations in active gels*, Soft Matter **7** (2011), 3234–3239.

[116] J. R. Sellers, *Myosins: a diverse superfamily*, Biochim. Biophy. Acta **1496** (2000), 3–22.

[117] M. Vicente-Manzanares, X. Ma, R. S. Adelstein, and A. R. Horwitz, *Non-muscle myosin II takes centre stage in cell adhesion and migration*, Nat. Rev. Mol. Cell Biol. **10** (2009), 778–790.

[118] T. D. Pollard and J. A. Cooper, *Actin, a central player in cell shape and movement*, Science **326** (2009), 1208–1212.

[119] A. J. Engler, S. Sen, H. L. Sweeney, and D. E. Discher, *Matrix elasticity directs stem cell lineage specification*, Cell **126** (2006), 677–689.

[120] D. Humphrey, C. Duggan, D. Saha, D. Smith, and J. Käs, *Active fluidization of polymer networks through molecular motors*, Science **416** (2002), 413–416.

[121] A. J. Levine and T. C. Lubensky, *One- and two-particle microrheology*, Phys. Rev. Lett. **85** (2000), 1774–1777.

[122] D. A. Head and D. Mizuno, *Nonlocal fluctuation correlations in active gels*, Phys. Rev. E **81** (2010), 041910.

[123] D. A. Head, Personal communication, 2011.

[124] O. J. N. Bertrand, D. K. Fygenson, and O. A. Saleh, *Active, motor-driven mechanics in a DNA gel*, Proc. Natl. Acad. Sci. USA **109** (2012), 17342–17347.

[125] B. Wang, S. M. Anthony, S. C. Baea, and S. Granick, *Anomalous yet Brownian*, Proc. Natl. Sci. Acad. USA **106** (2009), 15160–15164.

[126] B. Wang, J. Kuo, S. C. Baea, and S. Granick, *When Brownian diffusion is not Gaussian*, Nature Mat. **11** (2012), 481–485.

[127] L. J. Slater, *Generalized hypergeometric functions*, Cambridge University Press, London, United Kingdom, 1966.

[128] A. Erdélyi, W. Magnus, F. Oberhettinger, and F. G. Tricomi, *Higher transcendental functions*, Vol. 1, McGraw-Hill, New York, 1953.

[129] Y. L. Luke, *Mathematical functions and their approximations*, Academic Press, New York, 1975.

[130] A. M. Mathai and R. K. Saxena, *Generalized hypergeometric functions with applications in statistics and physical sciences*, Springer-Verlag, Berlin, Germany, 1973.

[131] C. S. Meijer, *Über whittakersche bzw. besselsche funktionen und deren produkte*, Nieuw. Archief Wisk. **18** (1936), 10–39.

[132] ———, *On the G-function*, Proc. Kon. Acad. Wet. Amsterdam **49** (1941), 227–237, 344–356, 457–469, 632–641, 765–772, 936–943, 1063–1072, 1165–1175.